Oceanographic studies of the Baltic Sea with emphasis on sea ice and mixing processes.

Christian Nohr

Doctoral Thesis in Oceanography

University of Gothenburg

The Faculty of Science
Department of Earth Sciences — Oceanography
University of Gothenburg
Earth Sciences Centre
Box 460, SE-405 30 Göteborg, Sweden

Akademisk avhandling för vinnande av Filosofie Doktorsexamen i Oceanografi vid Göteborgs Universitet. Avhandlingen kommer att offentligt försvaras onsdag den 27:e maj 2009, kl. 10:15 i Stora Hörsalen, Geovetarcentrum, Göteborgs Universitet, Göteborg.

Examinator: Professor, Anders Stigebrandt

Fakultetsopponent: Professor, Matti Leppäranta, Department of Physical Sciences, Division of Geophysics, P.O.Box 64 (Gustaf Hällströmin katu 2), University of Helsinki, Fi-00014 Helsinki, Finland

Christian Nohr
Oceanographic studies of the Baltic Sea with emphasis on sea ice and mixing processes.

A124 2009
ISSN 1400-3813
ISBN 978-91-628-7788-0
http://hdl.handle.net/2077/17688
Distribution: Earth Sciences Centre, Göteborg, Sweden

Abstract

This thesis comprises of model estimates of the water and heat budgets, re-estimating of the budget of deep-water mixing energy, model studies of generation mechanisms for internal waves, sea ice dynamics and finally sea ice monitoring. Common site for all the studies are the Baltic Sea.

A Baltic Sea model was used as a tool for synthesizing available data to be able to analyze the Baltic Sea water and heat balances. The accuracy in the long-term water and heat balances was quantified, while the accuracy of the individual terms is still unknown. The study illustrates the possibility of negative precipitation minus evaporation rates. The calculated inter-annual variability of the heat loss between atmosphere and Baltic Sea indicates large variations (± 10 Wm^{-2}). Despite an atmospheric warming no trend was seen in the annual mean water temperature.

Computations suggest that breaking internal waves, generated by wind forced barotropic motions, contribute significantly to the diapycnal mixing in the deep water of the Baltic Sea. Similar computations have previously been performed for tides in the World Ocean. However, the primary driver of barotropic motions in the Baltic Sea is the local weather. This causes the generated internal waves to have periods well above the inertial period. The stochastic forcing and the complex topography imply that the described energy transfer can be quite efficient even though the waves have super inertial periods. The diffusivity due to the dissipation of the barotropic motion conforms to earlier estimates and this mechanism also explains observed seasonal and spatial variations in vertical diffusivity.

Ice motion and ice thickness in the center of the Bothnian Bay was monitored with a bottom mounted ADCP for an entire winter season. The ice motion was primarily driven by the wind but with a clear influence of internal ice stresses and ice thickness. A rough force balance computation gave compressive ice strength 4 times larger than normally used in numerical ice models. The ridges made up 30-50% of the total ice volume showing that dynamical processes are important for the total ice production.

The development of a dynamic ice model includes a novel viscous-plastic approach where a memory of weak directions in the ice cover were stored. The model computes the ice motion, the ice deformation and the associated dynamic ice production and the results shows good agreement when compared with measurements of ice velocity from the ADCP. The results also show that the dynamic ice production typically increases the ice volume with 80% over the simulation period.

Key words: Baltic Sea; Water and Heat budgets; Deep-water mixing; Internal Wavedrag; Dynamical Sea Ice production; Sea Ice dynamics

Til Anna og Simen.

Contents

Preface

This thesis consists of a summary (Part I) to the following appended papers (Part II), which are referred to by their Roman numerals:

Paper I: A. Omstedt and C. Nohr, 2004: Calculating the water and heat balances of the Baltic Sea using ocean modelling and available meteorological, hydrological and ocean data. *Tellus A* 56(4), 400-414, doi:10.1111/j.1600-0870.2004.00070.x

Paper II: C. Nohr and B. G. Gustafsson, Computation of energy for diapycnal mixing in the Baltic Sea due to internal wave drag acting on wind-driven barotropic currents, Submitted to *Oceanologia*.

Paper III: G. Björk and C. Nohr and B. G. Gustafsson and A. E. B. Lindberg, 2008, Ice dynamics in the Bothnian Bay as inferred from ADCP measurements, *Tellus A* 60(1), 178-188, doi:10.1111/j.1600-0870.2007.00282.x

Paper IV: C. Nohr, G. Björk, and B. G. Gustafsson, A Simplified Model of Sea Ice Deformation Based on the Formation Direction of Leads. Accepted for publication in *Cold Regions Science and Technology*, doi:10.1016/j.coldregions.2009.04.005

A doctoral thesis at a university in Sweden is produced either as a monograph or as a collection of papers. In the latter case, the introductory part constitutes the formal thesis, which summarizes the accompanying papers. These have already been published or are manuscripts at different stages (manuscript, submitted, accepted or in press).

Part I

Summary

Plutselig stanser Brumm og peker
opphisset framfor seg: *"Se!"*
"Hva?" sa Nøff og hoppet i været,
og for å vise at han ikke hadde
hoppet fordi han var redd, fortsatte
han et par ganger til, som om
han drev gymnastikk.

A.A. Milne (*Ole Brumm, Sitatbok*)

1 Introduction

The Baltic Sea is a large fjord-like estuary and because most ocean processes can be found here, the Baltic Sea is a unique laboratory for oceanographic studies, see Fig. 1.1. The main objective of this thesis is to investigate and describe a few key physical processes in the Baltic Sea. In **Paper I**, the water and heat budgets of the Baltic Sea are revisited. In **Paper II**, the origin and magnitude of possible energy sources that drives vertical mixing processes in the central Baltic proper are identified. In **Paper III**, new observations of sea ice dynamics in the Bothnian Bay are presented and finally an alternative sea ice dynamical model is proposed in **Paper IV**. For those unacquainted with the Baltic Sea, the thesis starts with a short description of the physical oceanography of the Baltic Sea, and then the thesis will focus on each of the above processes in detail.

1.1 Physical description

1.1.1 Straits and sills

The Baltic Sea is divided into several minor basins separated by a number of sills, see Fig. 1.2. The two main sills separating Kattegat and the Baltic proper are Drogden Sill (8 m deep) and Darss Sill (15 m deep). In the north, the Baltic proper and Bothnian Sea are connected through the Southern Kvark Strait and Åland Sea. The main sill is wide and only 40 m deep intersected by a small channel of 70 m depth. Further north, Bothnian Sea and Bothnian Bay are connected through the Northern Kvark Strait which is separated into two channels, both with a depth of 25 m. In the east, Gulf of Riga is connected to the Baltic proper trough Irbe Strait, with a depth of 25 m and about 30 km wide. The width of the mouth between Baltic proper and Gulf of Finland is 75 km. The total area of the Baltic Sea is 387 000 km^2, where Baltic proper occupy 228 000 km^2. The average depth is only 55 m and the maximum depth is 459 m, located in the Landsort Deep.

1.1.2 The water exchange

The water exchange through the Baltic Sea entrance is driven by sea level variations in the Kattegat, which in turn are forced by atmospheric high and low

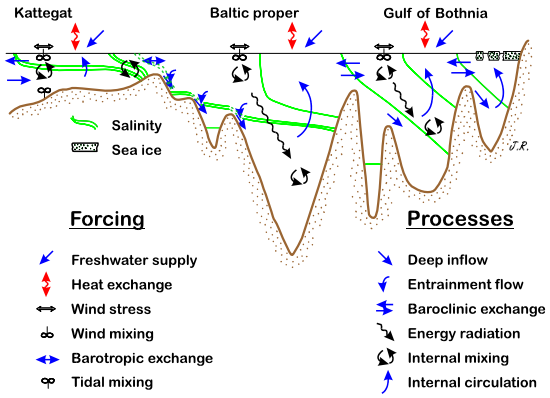

Figure 1.1: The main oceanographic forcing and processes found in the Baltic Sea.

pressure systems [Gustafsson and Andersson, 2001]. The water flow is mainly barotropic, i.e. the water is well mixed with the same pressure gradient force from the sea surface to the sea bed. Occasionally, there is a baroclinic exchange at Darss Sill, i.e. a two-layer exchange where there is an outflow from the Baltic in the surface and an inflow in the deep. The water exchange with the ocean is choked by the narrow and shallow straits, therefore sea level variations with periods shorter than ∼1 month are predominantly driven within the Baltic Sea and the response is that of a closed basin. For longer periods the Baltic reacts as an open bay and imported sea level variations dominate [Samuelsson and Stigebrandt, 1996]. Typical observed amplitudes of the dominant tidal component (M_2) in the Kattegat just outside the straits is 5 - 30 cm and in the southern Baltic Sea less than 1 cm [Svansson, 1975]. The Baltic receives a substantial net freshwater supply from rivers and through precipitation. The mean river runoff is about 15.000 m^3/s [Bergström and Carlsson, 1994] and precipitation minus evaporation (P-E) is about 1500 m^3/s [Rutgersson et al., 2002]. The mean outflow from the Baltic Sea is calculated to 57.000 m^3/s while the mean inflow is 42.000 m^3/s [Omstedt and Nohr, 2004]. However, episodic instantaneous inflows and outflows may vary in the range 0-300.000 m^3/s. The residence time of the entire water mass in the Baltic Sea is about 33 years [e.g. Stigebrandt, 2001, 2003, Stigebrandt and Gustafsson, 2003, Meier, 2005].

The heat cycle is closely linked to the water cycle, in that heat is either added or removed from the surface water by means of evaporation (E) and the negligible term precipitation (P). Omstedt et al. [2000] showed that earlier model studies of e.g. the water balances, indicated too large input of freshwater, such as the sum of P-E and river runoff. They in particular suggested improvements of the water cycle and in general identified a need for a better understanding of both

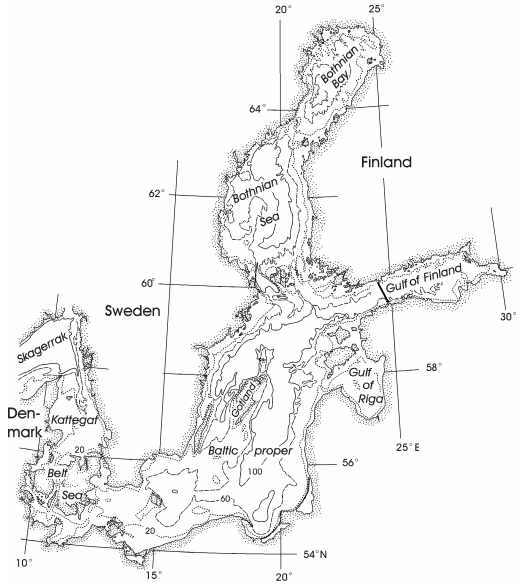

Figure 1.2: Bathymetric map of the Baltic Sea.

heat and water cycles. The main intention to revisit the water and heat cycle in **Paper I** was to improve our basic understanding of the Baltic Sea water and heat balance by estimating the accuracy of the balances, both on short- and long-term perspectives.

1.1.3 The water masses and vertical mixing

The substantial freshwater surplus in combination with limited ocean exchange, makes the main basin of the Baltic Sea, the Baltic proper, permanently salt stratified. The halocline is located at a depth of about 60 m and a seasonal thermocline is formed at 15-20 m depth during summer. The deep water, below 125-150 m depth, is stagnant in between irregular renewals and the stagnation periods lasts generally between 1-10 years [Stigebrandt, 2003, Meier, 2005]. Stagnation leads to decreasing oxygen concentration in the bottom water due to oxygen consumption by degradation of organic matter. Intrusion of dense water is often rich in oxygen and adds new oxygen to the stagnant bottom waters. The density of the inflowing water is controlled by the mixing and dynamics of the water masses in Kattegat [Gustafsson, 1997]. As soon as the water from the

Kattegat reaches inside the sills, the denser water forms dense gravity currents and pools of dense water in the downstream basins. The gravity current becomes less dense and increases in volume transport due to entrainment of surrounding basin water along the way to the deep parts of the Baltic. Depending on the final density, the water of the dense gravity current either interleaves into the basin water at the level of neutral buoyancy or comes to rest at the bottom of the deepest basin. There is a long-term balance in the deep water between the downward supply of new salt water by means of gravity currents, upward transport by advection and mixing with overlying less salty water masses. Vertical mixing increases the potential energy and dense water is lifted upwards by this process.

In contrast to the ocean where barotropic tides seem to be the major contributor of energy to mixing processes below the well-mixed surface layer [e.g. Garrett and St Laurent, 2002], wind driven motions seem to be the major energy contributor in the virtually tideless Baltic [Stigebrandt et al., 2002]. An indication of this is that the seasonal variation in the mixing intensity follows that of the wind [Axell, 1998]. However, the pathways of the different energy sources sustaining the turbulence that drives the vertical mixing below the seasonal pycnocline in the Baltic Sea, are largely unknown and so are their relative importance. The main objective of **Paper II** is to estimate the magnitude and find a source of the power required to drive the vertical mixing. The work was inspired by the calculations by Sjöberg and Stigebrandt [1992] and Gustafsson [2001] of the energy transfer from dissipating tides to vertical mixing in the ocean. They used the so-called local step model which describes the transfer energy from barotropic to baroclinic motions at steep topography [Stigebrandt, 1976]. The results was later validated by satellite based altimetry data [Egbert and Ray, 2000, 2003, Garrett, 2003]. The second objective of **Paper II** was to acquire the spatial distribution and the magnitude of this contribution. It was shown that several interesting "hot-spots" of energy transfer exists in the Baltic Sea and that the magnitude of the energy transfer plays an important role in the total energy conversion.

1.1.4 Sea ice

Sea ice affects the efficiency of wind driven diapycnal mixing and the heat flux between atmosphere and ocean. The efficiency of the insulation depends strongly on the ice thickness and the composition of the ice cover, and it is therefore important to simulate the ice cover as correctly as possible. The Bothnian Bay, the northernmost basin of the Baltic Sea, covers an area of 36 500 km^2 and the length between the Northern Kvark in the south and Tornio in the North is 315 km and the maximum width is 180 km (Fig. 1.2). The winters are severe enough to cause sea ice formation every year, which is ideal for modeling the seasonal sea ice cover. Ice formation generally starts in the shallow coastal areas in the north, and spreads into the basin. The ice season lasts 5-7 months depending on the severity of the winters [Leppäranta and Omstedt,

1999] and the mean sea ice thickness varies from year to year. Sea ice formed by thermodynamically growth only becomes 50-120 cm thick [Leppäranta and Omstedt, 1999], while sea ice formed by mechanical processes typically reaches a thickness of 5-15 m (occasionally 30 m) [Leppäranta and Hakala, 1992]. During mechanical deformation of sea ice the ice cover is broken up into smaller pieces that pile up into high ridges. Another important feature is the dynamical ice production, which starts when moving sea ice creates open water areas where the ice production is much higher than for the surrounding areas covered with ice. Rapid ice growth in the open water areas can represent a significant part of the total ice growth [Semtner Jr., 1975]. Ice thickness data has shown that over a full ice season in the Bothnian Bay, up to 50% of the ice volume may consist of mechanically deformed ice (see **Paper III**, Björk et al. [2008]). This indicates that the dynamical ice production is of significant magnitude (see also review by Granskog et al. [2006]).

Earlier investigations of sea ice drift in the Baltic have been based on surface drifters and SAR satellite data during relatively short periods [Uotila, 2001, Leppäranta, 1998]. The main objective of **Paper III** was to investigate how the ice motion responded to wind forcing from different directions and how the response changed due to variations in sea ice thickness and the amount of open water. For this purpose an upward looking ADCP (Acoustic Doppler Current Profiler) was deployed at the bottom of the Bothnian Bay and monitored the ice motion during an entire ice season. Previous data of sea ice thickness from the Bothnian Bay are relatively sparse [Jacob and Omstedt, 2005], but recent observations with an airborne Electro-Magnetic (EM) sensor increased the amount of data significantly (EU project IRIS, 2003-2005). The second aim with **Paper III** was to obtain an estimate of the amount of thick ice in the form of mechanically deformed ice. Sampling the ice thickness from a fixed position gives observations representing a long horizontal distance when the ice cover is moving. Ice motion in combination with thickness measurements from e.g. the ADCP, give a quantitative measure of the amount of different ice thicknesses, including the mechanically deformed ice.

In the Baltic Sea, horizontally integrated but vertically resolved coupled models have been proven to give reasonable results for the water column [e.g. Omstedt and Axell, 2003, Gustafsson, 2003], yet, the sea ice dynamic sub-models are still rather primitive. The reason for developing the sea ice model in **Paper IV** was to introduce a higher level of reality in the horizontally integrated models, and to provide efficient way to compute the dynamically induced ice production in addition to pure thermodynamical growth. The model presented in **Paper IV** is a one-dimensional sea ice model in which it is assumed that there exists a relationship between sea ice motions in two dimensions [Leppäranta et al., 1989] and that it is possible to identify so-called weaknesses in the ice cover. These weaknesses play an important role in the present sea ice dynamic model. One way to validate this type of model is to compare with estimates of the amount of open water that is formed by sea ice motions from e.g. ice charts. The time development of open water fraction not only controls the dynamical sea

ice production, but also the heat flux to the atmosphere during sea ice growth. The heat budget is thus closely linked to the sea ice dynamics by means of mechanical open water formation.

2 Water and heat balance

The on-going multidisciplinary and international BALTEX (the Baltic Sea Experiment) program focuses on several key questions in relation to water and heat cycles of the Baltic Sea and its catchments [BALTEX, 1995, 1997]. BALTEX started in 1992 and is a part of the Global Energy and Water Cycle Experiment (GEWEX) within the World Climate Research Program (WCRP). The primary research focuses of BALTEX are the water and heat cycles that are critical for the control and regulation of the Earth's climate in a fundamental manner. Improvement of modeling and parametrization of the individual components in the water and heat balances is an important task [Omstedt et al., 2000]. For this it is required that the water and heat budgets are considered simultaneously, because the strong coupling between the water and heat balance through the process that either cools down or heats up the sea surface due to the addition or to the removal of fresh water, such as rain or evaporation.

2.1 The water balance

The main components of the water cycle of the Baltic Sea is shown in Fig. 2.1.

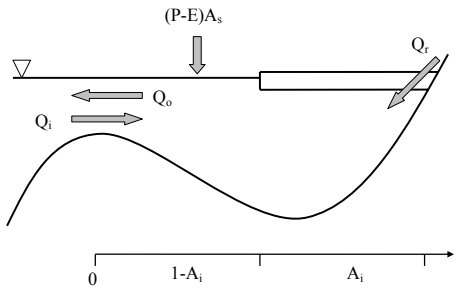

Figure 2.1: Main components in the water cycle of the Baltic Sea water body [from Omstedt and Rutgersson, 2000].

The volume change is given by a change in sea level per unit of time multiplied by the surface area of the Baltic Sea ($A_s \frac{d\eta}{dt}$). The change in water storage (positive

for volume increase) is important for short-term estimations of the water balance [Lehmann and Hinrichsen, 2001]. The volume change is balanced by inflowing (Q_i) and outflowing (Q_o) water through the entrance area, river runoff from the drainage area (Q_r), and the precipitation-evaporation rate multiplied by surface area ($A_s(P-E)$). In addition there are minor contributions from ground-water inflow (Q_g), volume changes due to ice advection (Q_{ice}), land uplift (Q_{rise}), thermal expansion when the water becomes warmer or colder (Q_T) and salt contraction when the salinity changes (Q_S). The Baltic Sea water balance can thus be written as [e.g. Omstedt and Rutgersson, 2000, Stigebrandt, 2001]:

$$\begin{aligned} A_s \frac{d\eta}{dt} &= Q_i - Q_o + Q_r + (P-E)A_s \\ &\quad + Q_g + Q_{ice} + Q_{rise} + Q_T + Q_S \end{aligned} \tag{2.1}$$

The terms Q_g, Q_{rise}, Q_T and Q_S have to be estimated since they are not explicitly modeled. For example thermal expansion, Q_T, may cause seasonal variations in volume flow of the order of 10^3 $\mathrm{m^3 s^{-1}}$ due to heating and cooling [Stigebrandt, 2001], but on an annual scale the volume flow is at least one order of magnitude less. The terms Q_i and Q_o are computed from the inflows and outflows of water caused by e.g. sea level or density differences over the sills. The term Q_{ice} is nowadays basically equal to zero, because only rarely ice passes through the entrance area. The remaining terms are estimated from measurements of river runoff from land, Q_r, and precipitation on the sea, P.

the total amount of precipitation over the drainage area such as land, Q_r, and water, P. Evaporation, E, on the other hand, is a calculated quantity and it is related to the humidity of the air close to the sea surface. For estimates of the magnitude of the various terms, see Table 2.1.

Table 2.1: Estimated annual mean volume flows for the Baltic Sea water balance (order of magnitude). All flows are positive going into the Baltic Sea.

Term	Magnitude ($m^3 s^{-1}$)
Q_i	10^5
Q_o	-10^5
$Q_o - Q_i$	-10^4
$(P-E)A_s$	10^3
Q_r	10^4
Q_{ice}	-10^2
Q_{rise}	-10^1
Q_T	$\pm 10^2$
Q_S	$\pm 10^1$
Q_g	10^2

2.2 The heat balance

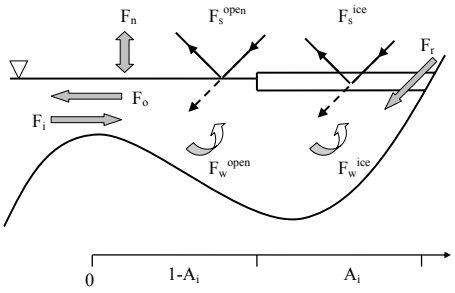

Figure 2.2: Main components in the heat cycle of the Baltic Sea water body [from Omstedt and Rutgersson, 2000].

The main components in the heat cycle of the Baltic Sea are shown in Fig. 2.2. The rate of change of the total heat content ($H = \int\int \rho_0 c_p T_{water} dz dA$, where ρ_0 and c_p are reference density and heat capacity of water, respectively) is balanced by advective inflow (F_i) and outflow (F_o) of heat through the entrance area, in addition to the net heat loss to the atmosphere (F_{loss}). From the heat conservation principles, we can write the heat balance equation for the Baltic Sea (note that the fluxes are positive when going from the water to the atmosphere) [e.g. Omstedt and Rutgersson, 2000]

$$\frac{dH}{dt} = (F_i - F_o - F_{loss})A_s \tag{2.2}$$

F_{loss} is calculated as the sum of net heat flux and solar radiation to the open water ($(1 - A_i)(F_n + F_s^{open})$) and through the ice-water interface ($A_i(F_s^{ice} + F_w^{ice})$). A_i is the ice concentration, F_s^{ice} the solar radiation through the snow/ice and F_w^{ice} the heat flux from ice to water. In addition, the heat sink associated with ice advection (F_{ice}) and heat flows associated with river runoff (F_r) and ground-water flow (F_g) also contribute to the total heat loss. Thus, the total heat loss reads

$$F_{loss} = (1 - A_i)(F_n + F_s^{open}) + A_i(F_w^{ice} + F_s^{ice}) + F_{ice} + F_r + F_g \tag{2.3}$$

The net heat flux (F_n) is the sum of the following components: The sensible heat flux (F_h) is the heat energy transfer between the water and air when there is a temperature difference. The latent heat flux (F_e) is associated with evaporation of water at the sea surface. It is an important component of the energy budget. The next term is the net long-wave radiation (F_l) that is the energy leaving the surface as infrared radiation. The radiation is proportional to forth power of the

absolute temperature of the sea surface, also known as the Stefan-Boltzmann law, or Stefan's law, i.e. $F_l \propto \sigma T_w^4$. Here σ is the Stefan-Boltzmann constant. In addition to these terms there are contributions from heat fluxes associated with precipitation in the form of rain (F_{prec}) and snow (F_{snow}). Finally, the net heat flux reads

$$F_n = F_h + F_e + F_l + F_{prec} + F_{snow} \tag{2.4}$$

The order of magnitude of some of the different terms are given in Table 2.2.

Table 2.2: Estimated annual mean heat fluxes for the Baltic Sea (order of magnitude). The fluxes are positive when going from the water to the atmosphere.

Term	Magnitude (Wm^{-2})
F_n	10^2
F_s^o	-10^2
F_w^i	10^0
F_s^i	-10^{-1}
F_{prec}, F_{snow}	10^{-1}
F_{ice}	-10^{-1}
F_r, F_g	10^{-1}
$F_o - F_i$	10^{-1}
F_{loss}	-10^0

2.3 Estimating accuracy of the water and heat budget

One of the main concerns when working with simulations are whether the model is accurate and to what extent the model agrees with observed data. In *Paper I* we estimate model accuracy terms of the major components of the water and heat budgets. The method used in **Paper I** is based on calculations of the mean and *root-mean-squared*, henceforth *rms*, of the difference between observed and modeled annual basin average salinity. In contrast to the mean values, the *rms* gives a measure of the variability of the difference between observations and model results. A high value on the *rms* indicates a large discrepancy between observations and model, which can be interpreted as lower model accuracy.
Starting with salt conservation

$$V\frac{dS}{dt} = (S_i - S)Q_i - (S_o - S)Q_o + \left[S(P-E)A_s + Q_f)\right] \tag{2.5}$$

Where S is an average salinity and assuming that $S_o \approx S$, Eq. (2.5) gives a balance between changes in inflowing saline water ($(S_i - S)Q_i$) and the fresh water ($S(P-E)A_s + Q_f)$). Thus, the error in salinity can be scaled to the

freshwater flux needed to explain the difference, such that the freshwater change, ΔQ, associated with changes in $(P-E)A_s$ and Q_f, can be written as

$$\Delta Q \approx -\frac{V}{\overline{S}}\frac{\Delta S}{\Delta t} \tag{2.6}$$

where V is the water volume and Δt is the time period of 1 year. Here $\overline{S}$ is the average and ΔS is the difference between the annual mean observed and modeled salinity. Fig. 2.3 shows ΔQ and its mean and *rms*. The mean error of the simulation period (1970-1994) is relatively small (600 $\mathrm{m^3 s^{-1}}$ which is 4% of the river runoff) while the *rms* error is 10 times larger (about 6000 $\mathrm{m^3 s^{-1}}$). This indicates that the model is reasonable accurate on longer time scales than 10 year, because the *rms* is a measure of the variability of ΔQ.

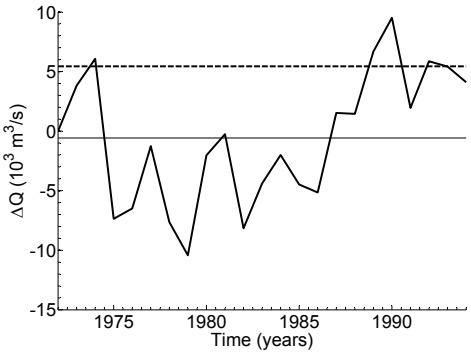

Figure 2.3: The difference between observed and modeled salinity represented by ΔQ. The dotted line is the *rms* and thin line is the mean of ΔQ.

Similar to the water cycle, the accuracy of the heat cycle was also estimated by calculating the mean and *rms* of the difference between observed and modeled annual basin average temperature. The temperature errors were coupled to variations in heat fluxes. Starting with the total heat content, the rate of change in the total heat content per square meter limited to the mixed layer, reads

$$\frac{dH}{dt} \approx \frac{\Delta}{\Delta t}\left(\rho_0 c_p \int_0^D T_{water} dz\right) \tag{2.7}$$

The temperature error, which is the difference between observed and calculated annual mean temperatures, ΔT, can thus be related to heat fluxes, ΔF, through the following relation:

$$\Delta F \approx \rho c_p D \frac{\Delta T}{\Delta t} \tag{2.8}$$

where D is the mixed layer depth and Δt is the studied time period of 1 year. ΔT is the temperature difference between observed and modeled temperature each year. ΔF is the corresponding error in the atmosphere-ocean net heat flux and Fig. 2.4 shows ΔF and its mean and *rms* errors.

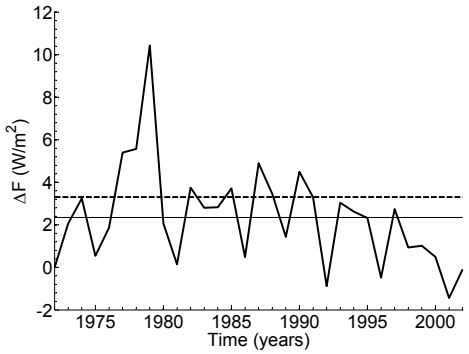

Figure 2.4: The difference between observed and modeled temperature represented by ΔF. The dotted line is the *rms* and thin line is the mean of ΔF.

In contrast to the errors in ΔS, the mean and *rms* temperature error over the simulation period (1970-2002) are both relatively small, 2 and 3 Wm^{-2}, respectively. This is 3-4% compared to the net heat flux (F_n), which indicates that modeling the heat flux is less demanding than the water budget.

2.4 Comments on some of the results

With new meteorological data, available for simulations covering the BALTEX/*Bridge*-period (October 1999-March 2002), the Baltic Sea model PROBE (Program for Boundary Layers in the Environment) [Svensson, 1998] was used as a tool for synthesizing available data and closing the water and heat balances. The modeling approach was validated against two independent data sets; observations of salinity and temperature and results from a coupled atmosphere-Baltic Sea model system, HIRLAM-BALTEX, that was run in a delayed data assimilation mode. The results obtained in **Paper I** supported earlier works, see a summary in Omstedt et al. [2004], and further indicated that accurate long-term water and heat balances can be calculated using current Baltic Sea modeling with meteorological and hydrological data available from the BALTEX data centers.

The calculated net heat loss between the atmosphere and the Baltic Sea during the BALTEX/*Bridge*-period indicated large inter-annual variability ($\pm 10 \mathrm{Wm}^{-2}$). The heat balances did not indicate any trend in the Baltic Sea heat loss, as shown by the annual mean temperature of the Baltic Sea in Fig. 2.5. Thus, the mean temperature in the Baltic Sea have been stable despite an atmospheric warming of 1 °C, which is also shown in Fig. 2.5. The annual mean and trend for observed and calculated water temperatures at the oceanographic station BY15 are plotted together with the annual mean air temperature and trend for the Baltic Sea. 30 years may seem to be a too short period to be able to make statements about trends. If it is used as an indicator for the temperature de-

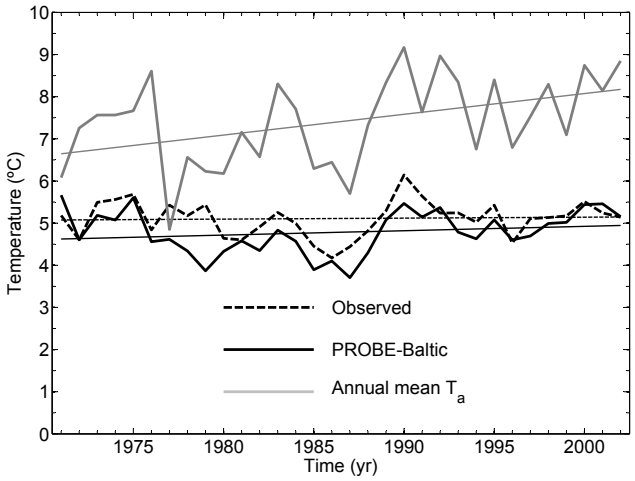

Figure 2.5: Annual mean temperature and trend lines for integrated ocean temperatures, observed (dashed line) and calculated (thick line) at BY15. Annual mean air temperature and the trend is also drawn (gray line) for the Baltic Sea.

velopment, however, it is shown that the integrated ocean temperature is quite stable, in contrast to the air temperature which is increasing. One reasonable explanation to the discrepancy is that the increased heat flux from the open water surface is balanced by an decrease in the cloudiness and consequently an increase in solar radiation [e.g. Karlsson, 2003]. In addition, the observed and calculated integrated temperature includes the deep water below the pycnocline. Water masses below the pycnocline are strongly dependent of the temperature of inflowing water through the entrance. The intrusion of new water is of seasonal character and the dense bottom current adds a time lag to the temperature signal because of a relatively long residence time for the bottom water, 5-6 year, compared to the residence time for heat in surface waters (1 year). Further does the temperature in the deep water depend on the time of deep water formation, which varies rather stochastic with each major inflow. Longer simulations than the simulation period used in **Paper I** are required to observe possible increases in temperature in the water masses.

The study also illustrated that annual negative precipitation-evaporation rates were possible, with the year 2002 standing out from the rest of the 30-year study period (see Fig. 2.6). Precipitation is provided as atmospherical forcing to the model, while evaporation rates are described by the formula [e.g. Gill, 1982, page 30]

$$E = \frac{\rho_a}{\rho_0} c_E W (q_s - q_a)(1 - A) \tag{2.9}$$

Here ρ_a is the air density and c_E is a constant parameter called the Dalton

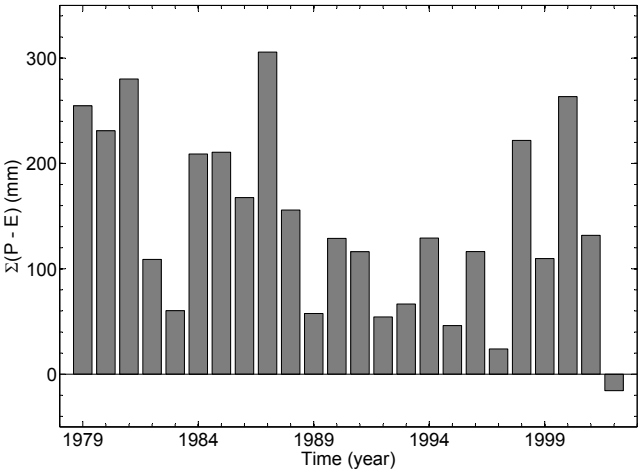

Figure 2.6: Precipitation - Evaporation annual sum for the Baltic Sea (excluding the Kattegat and the Belt Sea). 2002 was the only year with negative *P-E*.

number. The two important terms are q_a, the specific humidity at standard height above sea level and q_s the saturated specific humidity at the sea surface. The quantity q_a is often expressed as relative humidity ($= \frac{q_a}{/} q_s$) and is measured and provided with other atmospherical forcing like the wind speed (W). While the rest of the terms in Eq. (2.9) are given, the evaporation rate (E) can then be calculated by the model.

The individual terms in the water budget was compared with several other studies and the span in e.g. net precipitation ($A_s(P-E)$) varied between 1.5 and $1.99\times10^3\mathrm{m}^3\mathrm{s}^{-1}$ for ocean models and between 2.47 and $5.69\times10^3\mathrm{m}^3\mathrm{s}^{-1}$ for atmospheric models. A coupled model was also included in the comparison and in that study *P-E* was found to be $0.12\times10^3\mathrm{m}^3\mathrm{s}^{-1}$ [Meier and Doŝcher, 2002]. The results obtained in **Paper I** were $1.70\times10^3\mathrm{m}^3\mathrm{s}^{-1}$.

3 The source of energy for diapycnal mixing

3.1 The cascade of energy

3.1.1 Linear internal waves

In the ocean, except for quite small regions where events of convective overturning occur, density always increases with increasing depth, thus the water column is stable. The density is a function of salinity and temperature, such that generally cold water is denser than warm water and saline water is denser than fresh water.
When a parcel of water is displaced from its equilibrium in a stable stratification, gravity, or more precisely the buoyancy force, will drive the parcel towards its original position. Inertia will bring the parcel to oscillate around its original position. The frequency of the oscillation will be the Brunt-Väisälä frequency or buoyancy frequency if there are no rotational effects, i.e., the Coriolis[1] parameter $f = 0$. The Brunt-Väisälä frequency is defined as

$$N^2 \equiv -\frac{g}{\rho}\frac{\partial \overline{\rho}}{\partial z} \tag{3.1}$$

where g is the acceleration of gravity, ρ is a reference density, $\overline{\rho}$ the time mean density component and z is the vertical coordinate, positive upwards. In the situation described above, the stratification is stable and $N^2 > 0$. If the ocean is unstable, i.e. $N^2 < 0$, the parcel of water will accelerate away from its initial position due to the buoyancy force.
Disturbances in the stratification can make the parcel of water oscillate and internal waves emanate from these motions. Internal waves can be described by an infinitesimal motion in the fluid and the perturbations are described as $\rho' = \rho_0(z) + \rho(x, y, z, t)$ for the density and $p' = p_0(z) + p(x, y, z, t)$ for the pressure. The linearized[2] infinitesimal motion in a continuously stratified incompressible fluid, reads

[1] The Coriolis effect tends to deflect any free moving objects on the surface of the earth to the right on the northern hemisphere (left on the southern hemisphere).

[2] Linearized means that non-linear terms are neglected because they are products of two small quantities.

$$\frac{\partial u}{\partial t} - fv = -\frac{1}{\rho}\frac{\partial p'}{\partial x} \tag{3.2}$$

$$\frac{\partial v}{\partial t} + fu = -\frac{1}{\rho}\frac{\partial p'}{\partial y} \tag{3.3}$$

$$\frac{\partial w}{\partial t} = -\frac{1}{\rho}\frac{\partial p'}{\partial z} - g' \tag{3.4}$$

$$\frac{\partial u}{\partial x} + \frac{\partial v}{\partial y} + \frac{\partial w}{\partial z} = 0 \tag{3.5}$$

$$\frac{\partial g'}{\partial t} - N^2 w = 0 \tag{3.6}$$

where $g' = g\frac{\rho'}{\rho_0}$. In the following, and for simplicity, we adapt e.g. Turner [1973] who considered a time-dependent two dimensional (t, x, z) non-rotating fluid. By seeking plane wave-like solutions of e.g. the type $w = w_0 e^{i(kx+mz-\omega t)}$, the following dispersion relation[3] is found

$$\omega = N\sqrt{\frac{k^2}{k^2+m^2}} = Ncos(\theta) \tag{3.7}$$

This gives a relationship between the frequency (ω), the vertical (m) and the horizontal (k) wave numbers of the perturbation and the stratification (N). The phase velocity $(\boldsymbol{c})$ of the internal wave is defined as

$$\mathbf{c} = (\frac{\omega}{k}, \frac{\omega}{m}) \tag{3.8}$$

The terminology used for internal gravity waves is summarized in Fig. 3.1. Similar to surface waves we define short internal waves, i.e. when the wavelength is short compare to the water depth h ($kh \gg 1$ or $k^2 \gg m^2$)), the waves are dispersive. Whereas for long internal waves, i.e. when the horizontal wavelength is larger than the water depth ($kh \ll 1$ or $k^2 \ll m^2$), the waves are not dispersive. The internal waves are different from the surface waves in that the surface waves only propagate in the horizontal. The direction of propagation of internal waves $(\boldsymbol{K})$ depends on the ratio $\frac{\omega}{N}$. The energy flux of the waves follows the group velocity which is perpendicular to $(\boldsymbol{c})$,

$$\mathbf{c}_g = (\frac{\partial\omega}{\partial k}, \frac{\partial\omega}{\partial m}) \tag{3.9}$$

From Eq. (3.7) and Fig. 3.1, it can be seen that when $\omega \to N$, $\theta \to 0$ and the orbital motions are vertical and $(\boldsymbol{c})$ horizontal. If rotational effects are significant, the dispersion relation from the system of equation becomes

$$\omega^2 = N^2 cos^2(\theta) + f^2 sin^2(\theta) \tag{3.10}$$

[3]Motions in the fluid are generated with a given frequency but with different wavelengths. When moving away from the source, they will travel with different velocities and separate.

where f is the Coriolis[4] parameter. If $\omega \to f$, $\theta \to 90°$, the orbital motions become more horizontal with decreasing frequency. Another interpretation of Eq. (3.10) is that free internal waves solutions, i.e. k and m are real numbers, only exist for frequencies between the inertial frequency f and the buoyancy frequency N. Internal waves with frequencies lower than f can be for example so-called Kelvin waves that are trapped by the topography.

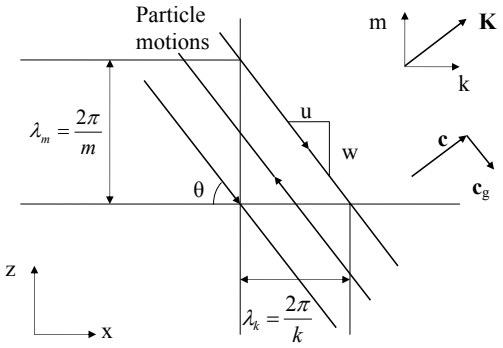

Figure 3.1: Internal wave terminology. Here u and w are the horizontal and vertical orbital velocity, respectively. The direction ($\boldsymbol{K}$) of the phase velocity ($\boldsymbol{c}$) is given by k and m, the horizontal and vertical wave numbers, respectively. The group velocity ($\mathbf{c}_g$) is normal to the phase velocity and is by definition the direction of energy transfer.

3.1.2 Descriptions in terms of modes

Another solution to Eq. (3.2-3.6) is found by seeking a wave like solutions for the vertical orbital velocity in two dimensions, $w(x,z,t) = F(z)e^{i(kx-\omega t)}$, with the boundary condition $w = F = 0$ at $z = 0$ and $z = H$. Thus the solution to Eq. (3.2-3.6) can now be expressed as

$$\frac{d^2F}{dz^2} + k^2\frac{N^2-\omega^2}{\omega^2-f^2}F = 0 \tag{3.11}$$

Eq. (3.11) can be solved analytically if N is constant and free wave solutions exists if $m^2 = k^2\frac{N^2-\omega^2}{\omega^2-f^2} > 0$, i.e. $f^2 < \omega^2 < N^2$. To find the waves of lower frequency than f one needs to consider also the other horizontal dimension, which allows for one complex and one real wave number. Another possibility, which we use here, is to disregard effects of rotation, i.e., setting $f = 0$. Assuming a plane wave solution of the type $F = b_n sin(mz)$, where $m = m_n = \frac{n\pi}{H}$ and b_n

[4]The Coriolis parameter or frequency, f, is equal to twice the rotation rate of the Earth, Ω, multiplied by the sine of the latitude, φ, $f = 2\Omega sin\varphi$

is the amplitude both for $n = 1, 2, 3, ...$ Here n is the vertical modes and the solution to the vertical orbital velocity becomes

$$w(x, z, t) = \sum_{n=1}^{\infty} b_n sin\frac{n\pi z}{H} sin(kx \pm \omega t) \tag{3.12}$$

and limiting ourselves to non-rotating long internal waves the dispersion relation is

$$\omega = \frac{NkH}{n\pi} \tag{3.13}$$

It is also possible to solve for the vertical wave modes for the horizontal orbital velocity ($\hat{u}_n$), thus the vertical and horizontal orbital velocity are related through continuity, Eq. (3.5). An example of the vertical wave modes of the vertical orbital velocities for a linear stratification, that is N = constant, is shown in Fig. 3.2.

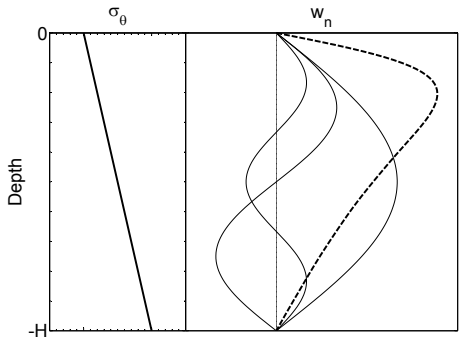

Figure 3.2: Density profile for constant N (left panel) and the first three vertical normal modes for the vertical orbital velocity w (solid lines) and the sum of these three (dashed line) (right panel).

If N describes an arbitrary stratification, the only way to solve Eq. (3.11) is by numerical techniques. This method imply that F is given by the eigenvalue problem, Eq. (3.14) and its boundary condition, Eq. (3.15) [e.g. Stacey, 1984]. The eigenvectors of Eq. (3.14) are found by the Runge-Kutta method, which is a refinement of the iterative methods for the approximation of solutions of ordinary differential equations. The structure of the vertical dependency is of the form

$$\frac{d^2\hat{W}_n}{dz^2} + \frac{N^2}{c_n^2}\hat{W}_n = 0 \tag{3.14}$$

with the boundary condition

$$\hat{W}_n(0) = \hat{W}_n(H) = 0 \tag{3.15}$$

where $w(x,z,t) = \sum_{n=1}^{\infty} \hat{W}_n(z) e^{i(m_n x - \omega t)}$ is the vertical orbital velocity of the nth internal wave mode. An example of the vertical wave modes of the vertical orbital velocity for an arbitrary stratification, is shown in Fig. 3.3. The method mentioned above also provides the dispersion relation c_n^2.

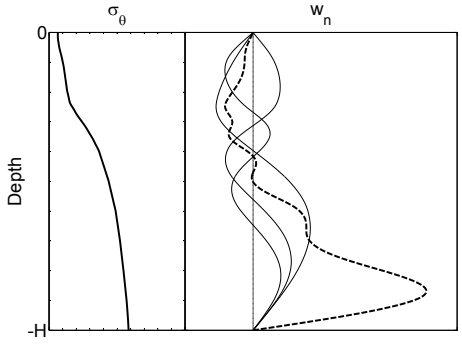

Figure 3.3: Same as Fig. 3.2, but for an arbitrary density profile.

All of these modes are called normal modes because they have the property of orthogonality, which means that the vertically integrated product of two different modes equals 0 and the modes do not contribute to any net transport of water.

3.1.3 Energy disintegration

By definition the group velocity determines the direction of the energy transfer. The group velocity for mode number n is defined as

$$\mathbf{c}_{g,n} = (\frac{\partial \omega}{\partial k_n}, \frac{\partial \omega}{\partial m_n}) \tag{3.16}$$

As seen from Fig. 3.1, when the phase propagation of an internal wave is upward, the energy transport is downward, and vice verse. The directions of the energy transfer coincide with the particle motions. Because the contribution from potential and kinetic energy is equal if averaged over a wavelength, a progressive internal wave's energy density per surface area equals

$$E_n = \frac{2}{T} \int_0^T \int_H^0 \frac{1}{2} \rho (\hat{u}_n^2 + \hat{W}_n^2) dz dt \tag{3.17}$$

and the total energy transport is

$$\epsilon = \sum_{n=1}^{\infty} c_{g,n} E_n \tag{3.18}$$

Each vertical internal wave mode provides an energy transport and the total energy transport is thus the sum of the contributions.

There is a general understanding that breaking internal waves are principal contributors of energy to diapycnal[5] mixing in the deep oceans. When internal waves get unstable, the waves break and the energy of the waves dissipate. A fraction of this energy is used for turbulent mixing. This fraction is called the *Richardson*-flux number (R_f), and typically 5-20% of the energy is used for mixing while the rest is transferred to heat. The stability of internal flows is dependent on the ratio between the stratification and the velocity shear, the *Richardson*-number

$$R_i = \frac{N^2}{\left(\frac{\partial u}{\partial z}\right)^2} \tag{3.19}$$

Here u is the water velocity and N is the typical frequency or inverse of the characteristic time-scale for perturbations on the isopycnal surface. The vertical gradient of the horizontal velocity can be interpreted as the inverse of the characteristic time-scale of vorticity created by the shear. If the time-scale of the vorticity is shorter than of the stratification, the stratification will not be restored by the force of gravity and vortices will carry denser water over less dense water as in Fig. 3.4. The motion is unstable if $R_i < R_{i(crit)} \simeq \frac{1}{4}$ and turbulence will be generated [Miles and Howard, 1964]. Fig. 3.4 shows an example of time development of instability, satisfying the above criteria. This mechanism is known as Kelvin-Helmholtz instability.

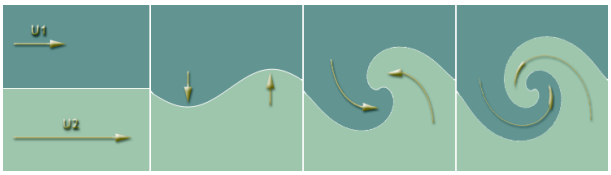

Figure 3.4: Example of time development of instability in a velocity shear. If $R_i < R_{i(crit)} \simeq \frac{1}{4}$, the wave will eventually break and result in turbulent mixing.

[5] Diapycnal is directly translated to "across the isopycnal" and surfaces of constant density is called "isopycnals". Thus, diapycnal mixing is by definition the process that mix water parcels of different density.

3.2 Mechanisms that generate energy for diapycnal mixing

Observations in the oceans show that turbulent mixing is weak over smooth topography and strong over rough topography [e.g. Polzin et al., 1997]. The energy loss from surface tides in areas with ridges and other seafloor topographic features has also been observed by means of satellite based altimetry data [Egbert and Ray, 2000, 2003, Garrett, 2003]. Model studies have also calculated the distribution of energy fluxes to deep ocean mixing processes due to topographically generated internal waves in the world oceans [e.g Sjöberg and Stigebrandt, 1992, Jayne and St Laurent, 2001, Gustafsson, 2002]. Both observations and computations support and confirm the hypothesis that deep ocean turbulent mixing achieves a considerable amount of energy from surface tides via breaking of internal waves [e.g. Garrett and St Laurent, 2002]. In the virtually tide less Baltic Sea, barotropic surface waves caused by the stochastic changes in the wind stress, may replace barotropic tides as a energy source for turbulent mixing. Perhaps, as an analogue to the deep ocean, also in the Baltic, energy to sustain vertical mixing may be generated by barotropic waves at steep topography.

3.2.1 Internal wave generation

There are basically two lines of theories that describe the energy transfer from barotropic motions to internal waves due to irregularities in topography. The first is the so-called local step-model [Stigebrandt, 1976, 1980, Sjöberg and Stigebrandt, 1992, Gustafsson, 2001, Stigebrandt, 1999, Johnsson et al., 2007] and the second is a regional roughness model that was proposed by Jayne and St Laurent [2001].

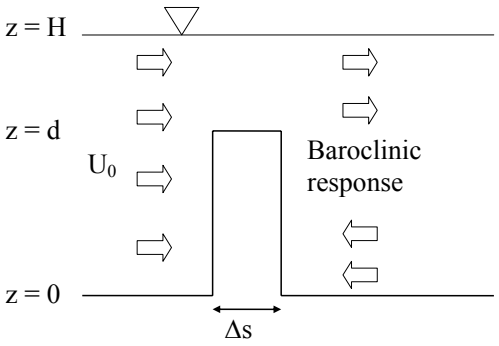

Figure 3.5: Conceptual sketch showing the step model.

The local step model is based on the difference between the height (d) and size (Δs) of an obstacle and the depth of the surrounding bottom (H), see Fig. 3.5. The basic idea is as follows: When a barotropic current meets an obstacle on the ocean floor, no water can penetrate the obstacle. At the obstacle, a baroclinic response is superimposed on to the barotropic tide so that the sum of barotropic and baroclinic currents is zero at the obstacle wall. The barotropic current is expressed as a wave, such that $U_0 = a_0 cos(k_0 x \pm \omega t)$. The term $(k_0 x \pm \omega t)$ describes a propagating wave that travels with the speed equal to $c_0 = \frac{\omega}{k_0}$ in either positive or negative direction. The total velocity is equal to the sum of the barotropic current and a sum of an infinite number of internal wave modes n

$$u(x,z,t) = a_0 cos(\omega t \pm k_0 x) + \sum_{n=1}^{\infty} a_n \hat{u}_n(z) cos(k_n x \pm \omega t) \tag{3.20}$$

where a_n is the amplitude and $u_n(z)$ is the horizontal orbital velocity of the nth normal mode. Using Eq. (3.20) to calculate the energy density with Eq. (3.17), the energy density now takes the form

$$E_n = \frac{\rho}{2} \frac{u_s^2 \left[\int_d^H \hat{u}_n dz\right]^2}{\int_0^H u_n dz} \tag{3.21}$$

where u_s is the velocity just above the obstacle. Inserting the above expression for E_n into Eq. (3.18), ϵ now correspond to the amount of energy that is removed from the barotropic wave as it passes the obstacle. In the local step model, the energy flux would be regarded as baroclinic wave drag.
The regional roughness model is not used in this thesis, however a short outline of the model is given here as an example, see Jayne and St Laurent [2001] and references therein for further details. The model is built on a wave number (ξ) and an amplitude (h) that characterizes the vertical variation of the bathymetry in a larger area. The wave number ξ is considered as a free parameter and it is allowed to be adjusted to minimize the difference between observed and modeled results, e.g. tides. The amplitude h is calculated by adjusting a polynomial sloping surface to the bottom topography and the residual heights are used to compute h, i.e. the mean-square bottom roughness averaged over the grid cell. The energy flux lost by the barotropic tide to internal waves is thus proportional to ξ, h^2 and the buoyancy frequency N.

3.2.2 Model approach

The main objective of **Paper II** was to investigate to what extent energy can be transferred via barotropic motion from the atmosphere to turbulent kinetic energy in the deep. For this purpose, a parametrization of wave drag were derived from the local step model and a first order approximation for the drag loss to the turbulent bottom boundary layer were used in a 2-dimensional shallow water model.

A two-layer internal wave generation model was developed and applied to the Oslofjord by Stigebrandt [1976]. He idealized the stratification of the fjord by having the interface between two water masses at the depth of the sill. It is clear that this energy transfer approach does not suit the Baltic Sea, see Fig. 3.6a. The solution using constant N was derived by Stigebrandt [1980] and applied to the Herdlafjord. This solution gives an infinite number of modes. Constant N is not a suitable approximation to the stratification in the Baltic Sea, see Fig. 3.6b. A theoretical density profile was used by Sjöberg and Stigebrandt [1992] to approximate stratification in the world oceans, see Fig. 3.6c. However, they only investigated the energy transfer below the mixed surface layer. In the Baltic Sea, there are reasons to believe that much of the energy is transferred into the first baroclinic mode which is associated with motions in the pycnocline. Hence, their approach is not valid in the Baltic Sea.

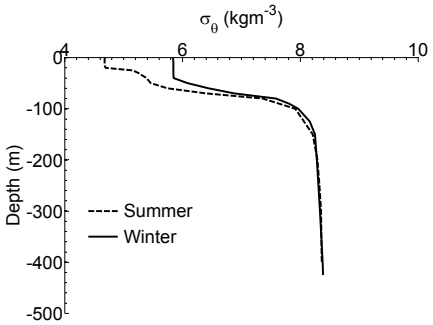

Figure 3.6: Three approaches to represents the density profile in the models of the barotropic to baroclinic energy transfer. Dashed line is summer and thin line is winter stratification. Thick line is the assumed density profile. Panel a is the two layer approach [Stigebrandt, 1976]. Panel b is the constant N [Stigebrandt, 1980]. Panel c is the theoretical density profile used by Sjöberg and Stigebrandt [1992] for the whole oceans.

Opposing the oceanic applications of Sjöberg and Stigebrandt [1992], Gustafsson [2001], the whole water column must be considered because one would expect a dominant influence of the first baroclinic mode. Therefore, a generalization of internal wave drag on barotropic currents for arbitrary stratification given by Stacey [1984] is adapted to give drag force in a two-dimensional shallow water model. In **Paper II**, the separation of variables described by Eq. (3.14) is used to approximate the stratification and find wave solutions [Stacey, 1984]. The horizontal (Eq. (3.20)) and vertical (Eq. (3.12)) velocities are related through the continuity, Eq. (3.5), such that there are barotropic and baroclinic continuities

$$\frac{du_0}{dx} + \frac{dw_0}{dz} = 0 \tag{3.22}$$

$$\frac{d}{dx}a_n\hat{u}_n(z)cos(k_nx \pm \omega t) + \frac{d}{dz}b_n\hat{W}_n(z)e^{i(k_nx\pm\omega t)} = 0 \tag{3.23}$$

Solving the barotropic part of the continuity, equals $a_n\hat{u}_nk_n = b_n\frac{d\hat{W}_n}{dz}$. This expression for $\hat{u}_n$ makes it possible to evaluate the energy density for individual vertical modes. The dissipation from barotropic motion in the model is given by $\epsilon_{SH} = \rho u_i F_w^x \Delta s$, where where F_w^x the drag force and Δs the grid spacing. The index i is the ith grid point. The same formulation is also valid for the jth grid point. The velocity u_s is the velocity at the shallow part, i.e. the obstacle of depth d while u_i formally is the velocity at average depth between the two adjacent grid cells, $\frac{1}{2}(H+d)$, where H is the maximum depth of the two adjacent grid cells and d is the minimum of the same. From volume conservations, $u_sd = u_i\frac{1}{2}(H+d)$. In the model the baroclinic drag coefficient at the grid point i is defined as $r_w^x = -\frac{F_w^x}{u_i}$. Now, inserting the expressions for $\hat{u}_n$ and u_s into Eq. (3.21), the baroclinic drag coefficient reads

$$r_w^x = -\frac{1}{2\Delta s}\left(\frac{H+d}{2d}\right)^2\sum_{n=1}^{\infty}c_n\frac{\hat{W}_n(d)^2}{\int_H^0\left[\frac{d\hat{W}_n}{dz}\right]^2dz} \tag{3.24}$$

The vertical orbital velocity, $\hat{W}_n$, and the group speed, $c_{g,n}$, is computed for the deepest of the two cells. The bottom drag force is approximated by

$$\mathbf{F}_b = -C_d\left|\mathbf{v}\right|\mathbf{v} \tag{3.25}$$

where C_d is a dimensionless drag coefficient and $\mathbf{v}$ is the velocity vector. One limitation to the shallow water equations is that parametrization of drag from bottom boundary layers becomes rather dubious for strongly stratified basins since the actual bottom near currents might not be related to the barotropic flow. However, the aim here is not to realistically simulate the vertical current structure, but to make an order of magnitude estimate of the possible energy conversion from atmospherically forced barotropic motion to internal motion and for this purpose the shallow water approximations will most probably suffice.

3.2.3 Some remarks on the results

The bottom near currents are determined to a large extent on the baroclinic response, thus the main focus in the following will be on the contribution from dissipation due to internal wave drag. The results from **Paper II** have shown that transfer of energy from low-frequency wind forced barotropic motions to internal waves potentially is an important driver of diapycnal mixing in the Baltic Sea. The magnitude of the dissipation by internal wave drag agrees well with earlier estimates of the needed energy supply to mixing. The vertically integrated transfer of energy from barotropic motion to internal waves for the Baltic proper was about 0.23 mW m^{-2}, which at first glance is substantially less

than the required energy supply from the surface layer of 2.1 mWm^{-2} [Liljebladh and Stigebrandt, 2000].

Dissipation due to wave drag is quite patchy with several hot spots. Particularly along the 50 m isobath, where costal jets and abrupt topography are causes for this enhanced energy transfer. Strong coastal currents also increase dissipation due to bottom stress at the shallower shelf, in particular shallower than the 50 m isobath. An examination of the vertical variation of dissipation due to internal wave drag brings another perspective to the results. The magnitude of the dissipation is quite different in the different areas, but it is of approximately the same magnitude for the whole water column and does not decrease with depth as fast as dissipation by bottom stress. Consequently, the relative contributions from internal wave drag increases at deeper parts of the basins. The change in dissipation is different in the different areas, e.g. in Landsort deep the dissipation increases with depth, while dissipation decreases to zero in Gotland deep. This broadly conforms with Axell [1998] who found that the work against buoyancy forces[6] decreased with depth in both areas. However, he found that the decrease started at above 300 m depth in Landsort deep and this might not be resolved in the present model. The influence from higher order modes becomes prominent at depth and it is more pronounced in some areas where it can contribute with about 40% of the mixing (see Fig. 9 in **Paper II**). The strong seasonal signal simulated in **Paper II** was also seen by Axell [1998], confirming that the main source of input for mixing must be the wind. During strong wind events, dissipation due to wave drag could easily increase 10 times the average dissipation.

How much does the energy transfer due to internal wave drag actually contribute to the deep water mixing? Assuming that dissipation only occur below a certain depth level, this dissipation is regarded as the supply of mechanical energy to the volume below that depth. However, only a fraction (R_f) of the dissipated energy in this particular volume can be used for mixing. With 50% increased wind speed (discussed below), we obtain dissipation due to wave drag below 150 m depth of e.g. 1-2 mWm^{-2} in the Landsort deep and 0.25 mWm^{-2} in the Gotland deep. If we use $R_f = 0.11$ as suggested by Arneborg [2002], we obtain work against buoyancy forces of $1 - 2 \times R_f = 0.1 - 0.2$ mWm^{-2} and $0.25 \times R_f = 0.027$ mWm^{-2}. Thus, the simulated dissipation due to wave drag is comparable to the work against buoyancy forces obtained by Axell [1998] of 0.25 and 0.03 mWm^{-2}, respectively. This means that dissipation due to wave drag simulated in **Paper II** could potentially explain all the deepwater mixing in the Baltic Sea. However, there are factors involved in the process of energy transfer that are not yet fully understood and these factors can both increase and decrease the magnitude of the simulated energy transfer. Some of these uncertainties will be addressed below to high-light the model sensitivity.

Geostrophic wind and pressure fields over the Baltic Sea, which are used to force the model, were extracted from a gridded meteorological database (Swedish Meteorological and Hydrological Institute, SMHI). The $1^\circ \times 1^\circ$ fields are generated

[6] Work against buoyancy forces is defined as dissipation due to e.g. wave drag $\times R_f$.

from synoptic stations and these can only be found on some major islands in the Baltic Sea. Consequently, the fields will be very smooth, small-scale pressure anomalies and strong wind events will not be resolved properly [e.g Omstedt et al., 2005]. Low variability in the forcing will reduce fluctuations in the barotropic currents and this underestimates the simulated energy conversions. In **Paper II**, we made a simple sensitivity test increasing wind stress with 25-75% and that caused the average energy loss due to wave drag increased with $\sim$ 30-110% and increases with up to 50% increased the accuracy of simulated coastal sea levels.

Another factor that could increase energy transfer is high frequency currents, see Fig. 3.7. High-frequency currents with periods less than 10 hours are underestimated in the model. Frequencies higher than the inertial frequency should theoretically be more efficient in producing free internal waves, thus we may not resolve an important part of the spectrum. The reason for that the model does not resolve these oscillation may party be due to resolution of the model and partly due to the smooth forcing.

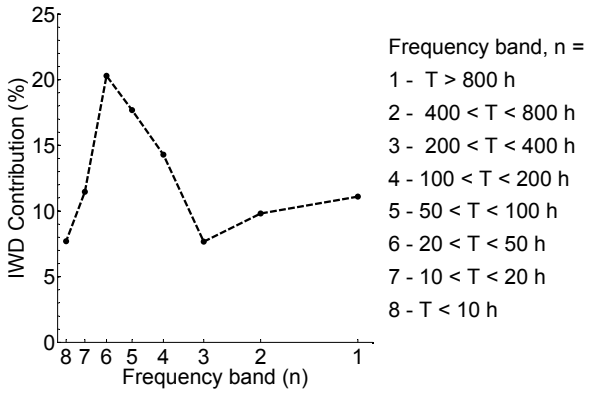

Figure 3.7: The relative internal wave drag response divided into frequency bands.

The validity of the step model was recently challenged by Laurent et al. [2003] and one of the concerns where the resolution dependence, in that the internal wave generation approached zero as the resolution was increased. The parametrization may be sensitive to the grid size, Δs. However, this issue was discussed in Sjöberg and Stigebrandt [1992] and Gustafsson [2002] arguing that the barotropic to baroclinic energy conversion was only weakly dependent on the resolution of the topography and that most of the energy transfer in the oceans occurs at steep topography. Thus that is 97% of the total energy transfer is confined to only 10% of the area. Because of the limitation in obtainable high resolution bottom topography, in **Paper II** we performed control runs with a interpolated grid size of 1 and 4 nm, that resulted in only a 10% change in the

total wave drag but in the small deep basins the sensitivity was higher. It was difficult to draw definite conclusions on the sensitivity on resolution since the finer grid was interpolated and did not contain smaller scale topography, and the coarser resolution does not really resolve the deep areas and the narrow straits properly.
In the present model, the baroclinic drag coefficient Eq. (3.24) only accounts for energy fluxes on the deep side of the step, where the water depth H is deeper than the step height d, c.f. Fig. 3.5. Laurent et al. [2003] analyzed the ratio between energy flux radiating away over the shallow side of the step to the total energy flux and they found a asymptotic behavior of the step height ratio, $\delta = \frac{d}{H}$. The energy density of the waves on the shallow side is however less than on the deep side because they assumed that the phase speed was proportional to the vertical wavelength. This indicate that the result in **Paper II**, may potentially be underestimated by approximately 20%.
Laurent et al. [2003] argued further that waves generated at different topographic steps are interacting with each other and the interaction affects the magnitude of the energy transfer. As they say:

> A valid model for internal tide generation at a series of steps must include interference phenomena occurring between internal tides generated at neighboring steps. Interference effects allow for convergence of internal tide estimates as the number of steps is increased to better resolve the topography.

We treat all steps between grid cells as autonomous wave makers, which means that we do not consider any interaction between waves generated in adjacent cells. This approach can naturally be challenged, especially considering that the grid cells are only some 3.7 km wide, which is similar to a Rossby radius. For comparison, an along-slope wavelength for Kelvin waves with these frequencies is approximate 100 km. Based on observations, Johnsson et al. [2007] found that two sills close to each other (distance $\approx$ 1 km) did act like autonomous wave makers for tidal currents. This result obtained by Johnsson et al. [2007] are in sharp contrast to the arguments by Laurent et al. [2003] while it supports the approach in **Paper II**.

4 Observing and modeling Sea Ice

In the first section (sec. 4.1) of this chapter a short, but general introduction to sea ice for those readers unfamiliar with the subject is provided. In the next section (sec. 4.2), a method to monitor sea ice motion and thickness in the Bothnian Bay is presented. Finally, in the last section (sec. 4.3) a new sea ice sub-model to be used in horizontal integrated coupled ocean models for the Baltic Sea is presented.

4.1 A short introduction to sea ice

4.1.1 Sea ice types

Sea ice is any form of ice found at sea that originates from the freezing of sea water. In sea ice terminology, differentiation is made between *undeformed* ice and *deformed* ice. Undeformed ice is solely created by thermodynamical processes, such as freezing and melting. Undeformed ice can either be fixed to the shoreline, so-called *fast ice*, or it can drift in the basin either as smaller *ice floes* or larger areas of *level ice*. Under influence of wind and ocean currents, ice floes drift together and create *pack ice fields*, and level ice can drift towards some kind of obstacle and become mechanically deformed and build *ridge ice* or *pressure ridges*. When ice drifts apart or warm water melts the ice, areas of open water appear, known as *leads* or *polynyas*. Some of these ice types are illustrated in Fig. 4.1a-c. The thickness of the ice inside the pack ice field ranges from a few centimeters of new ice to several tens of meters in the pressure ridges. There are three important properties of sea ice, i.e. internal sea ice stress (σ), strain (E) and strain rate (ϵ) and the relationships between the properties are shown in Fig. 4.2a-c. Given that strain results in the deformation of a body, it can be measured by calculating the change in length of a line or by the change in the angle between two lines (where these lines are theoretical constructs within the deformed body). This change is termed the stretch, absolute strain, or extension, and may be written as ΔL. The (relative) strain is given

$$E = \frac{\Delta L}{L_0} = \frac{L - L_0}{L_0} \tag{4.1}$$

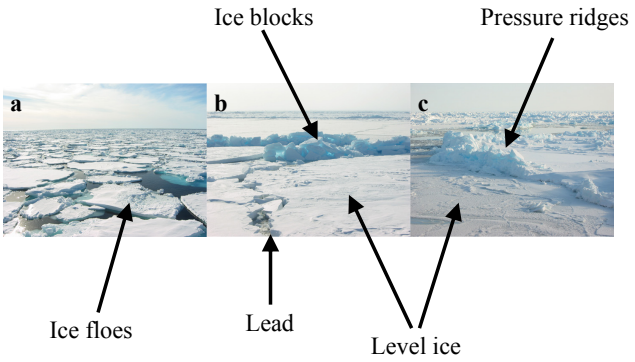

Figure 4.1: Typical sea ice types found in the ice covered oceans. Plate a shows loosely packed ice floes and plate b shows level ice that is crushed into ice blocks and a small crack is created, called a lead. Plate c shows level ice which is deformed into a ridge ice forming a pressure ridge.

where L_0 is the original length of the material and L is the current length of the material. The change of E per unit of time is called the rate of strain, or just strain rate:

$$\epsilon = \frac{1}{\delta t} E \tag{4.2}$$

If an ice field is loosely packed, i.e. there are areas of open water between the floes, the wind and water current will either spread the floes or move the floes closer to each other. If the floes are moved together and there are no obstacles downwind, the pack ice will move like a fluid in a *viscous* manner (c.f. Fig. 4.2a). If the wind speed increases and there are larger floes of level ice that are hampered by some obstacle, the ice floe may tend to buckle up downwind due to the integrated wind stress. As the wind diminishes, the ice floe will straighten out and thus the ice floe will behave in an *elastic* manner (c.f. Fig. 4.2b). If the wind instead pick up more speed, the ice floe will begin to deform at the downwind side and pressure ridges arises. The reason for this is that the integrated wind force becomes too strong for the internal ice stress to resist, and the ice floe is broken in pieces which is a typical *plastic* behavior (c.f. Fig. 4.2c).

4.1.2 Sea ice rheology

The rheology of sea ice is described by the internal distribution of the ice stresses. There are several mechanisms that create these stresses in the ice field and these

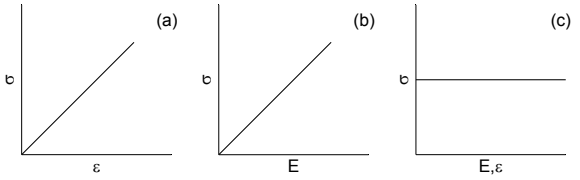

Figure 4.2: Sea ice behavior, acting a) linear viscous, b) linear elastic and c) plastic. The figures showing the relationships between internal sea ice stress (σ), strain (E) and strain rate (ϵ).

are: (i) floe collisions, (ii) floe break up, (iii) shear friction between floes, (iv) friction between ice blocks in pressure ridge formation and (v) potential energy production in the process of creating pressure ridges. The relationship between the strain of sea ice, its strain rate and sea ice states ($\mathbf{J}$) constitutes the internal stresses in sea ice, thus

$$\sigma = \sigma(E, \epsilon, \mathbf{J}) \tag{4.3}$$

Since ice is a three-dimensional medium, σ has 9 components, a so-called tensor[1]. The internal ice stresses are associated with compressive and shear stresses for each dimension. But for simplicity we only consider motion in x-and y-direction, neglecting any motion in the vertical z-direction. This reduces the number of components in σ to 4.
The physical meaning of the stress tensor is described in terms of invariants. As with a vector, there are certain invariants associated with the stress tensor. For a vector, there is only one invariant - the length (or the magnitude). For a tensor, there are three - the so-called eigenvalues of the stress tensor (σ_1, σ_2). The eigenvalues are called the principal stresses and they provide the direction and the magnitude. It is important to note that the only physically significant parameters of the stress tensor are its invariants, because they do not depend on the choice of the coordinate system used to describe the tensor.
In a 2-dimensional plastic problem there is a yield curve in the principal stress space, i.e. the curve where the critical yield stress σ_y of the ice is confined. The shape of this curve is debated and as examples, a teardrop [Coon et al., 1974]

[1] A tensor is an object which extends the notion of scalar and vector.

and an elliptical [Hibler, 1979] form are shown in Fig. 4.3. The interpretation of the curves is as follows: Inside the yield curve, the ice is rigid whereas the applied stress is too small to plastically deform it. Outside the yield curve, the ice behave viscous and/or elastic. If the applied force is directed along the center line, σ comprises of only a compressive stress[2] defined by the ice strength itself, otherwise if the applied force is not directly parallel to the center line, shear stresses[3] are induced.

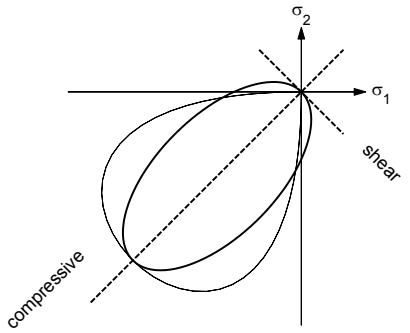

Figure 4.3: Examples of a teardrop and an elliptical yield curve for a 2-dimensional plastic problem.

4.1.3 Drifting sea ice

In the rheology problem of drifting sea ice, qualitatively and quantitatively different laws apply to different packing densities and thicknesses of the ice floes [Leppäranta, 2005]. One important rheology parameter is the ice strength, which is primarily a function of how the thickness of different ice types are distributed and how much open water there is in the ice cover [Thorndike et al., 1975]. The dynamic processes are connected to the distribution of ice thickness within the ice cover. For confined ice covers such as the Bothnian Bay much of the dynamics are controlled by the solid boundaries at the coast line or land fast ice such that pressure ridges tend to build up at the downwind side of the basin and open water forms at the upwind side.

The standard way to describe the motion of pack ice is to solve the momentum equation numerically on a two-dimensional grid for prescribed external forcing such as winds and ocean currents. The general system has two unknowns, the ice velocity vector $\mathbf{u}(x, y, t)$ and the ice state $\mathbf{J}$. The equations read

[2] Compressive stress is the stress applied to materials resulting in their compaction (decrease of volume).

[3] A shear stress is defined as a stress which is applied parallel or tangential to a face of a material, as opposed to a normal stress which is applied perpendicularly.

$$\begin{aligned} \rho_{ice} H_{ice} [\tfrac{D\mathbf{u}}{Dt} + f\mathbf{k} \times \mathbf{u}] &= \nabla \cdot \sigma + \mathbf{F}_{ext} \quad (a) \\ \tfrac{D\mathbf{J}}{Dt} &= \psi + \phi \qquad\quad (b) \end{aligned} \tag{4.4}$$

where H_{ice} is the thickness of the ice, ρ_{ice} is density of the ice, f the Coriolis parameter and $\mathbf{k}$ the unit vector pointing in z-direction. The term $\frac{D}{Dt}$ is the total derivative and it comprises of both local acceleration and the advective terms. Depending on the type of ice dynamics a certain model uses, the divergence of the internal ice stress ($\nabla \cdot \sigma$) can take many shapes, one or a combination of elastic, viscous and/or plastic rheological behaviors (cf. Fig. 4.2). The ice state consist of all the variables that describe the pack ice, e.g. the ice thickness for undeformed (H_l) and deformed ice (H_r), the compactness of the ice (A_i) i.e. how much open water there is between the separate ice floes, and so on. Thus $\mathbf{J} = \mathbf{J}(H_l, H_r, A_i, ...)$. A three-level distribution model usually has two ice types, undeformed level ice and deformed ridged ice, in addition to compactness. The ridging function (ψ) describes how the model handles deformation of sea ice and the thermodynamical function (ϕ) describes the ice growth and melt. When the internal ice stress is weak (i.e. thin ice or $A_i \ll 1$) the Coriolis force balances the external forces ($\mathbf{F}_{ext}$), and the resulting free drift ice motion (the directed motion is to the right of the wind on the northern hemisphere and left in the southern hemisphere).

4.1.4 Modeling sea ice

Two-dimensional dynamical ice models are used extensively in many investigations of pack ice in the Arctic, Antarctic and coastal seas such as the Baltic Sea. The central dynamic part is described by the rheology and there exists different lines of models treating the sea ice in different ways; e.g. the AIDJEX model where the rheology treats sea ice as an elastic medium at low levels of stress and plastic above critical levels of stress [Coon et al., 1974] and Hibler's approach where the ice is treated as a viscous medium at low level of stress and plastic otherwise [Hibler, 1977, 1979]. Another line of model combines all of the material behavior in an elastic-viscous-plastic rheology model [Hunke and Dukowicz, 1997], which improves the computational efficiency by letting the time scale determine if the ice field should behave elastic or viscous-plastic.
The majority of these models redistribute the ice volume after the ice cover has undergone plastic deformation. Ice thickness distribution, often referred to as *ITD*, is a way of bookkeeping the ice cover in terms of ice categories such that category 0 is the area fraction (a_0) of thinnest ice or open water, category 1 is the area fraction (a_1) of the next thicker ice and so on. After plastic deformation, a fraction of the volume of one single category of the thinnest ice is redistributed to a finite number of thicker categories after deformation. This is illustrated in Fig. 4.4. For a recent review of sea-ice thickness redistribution models, see e.g. Savage [2008].

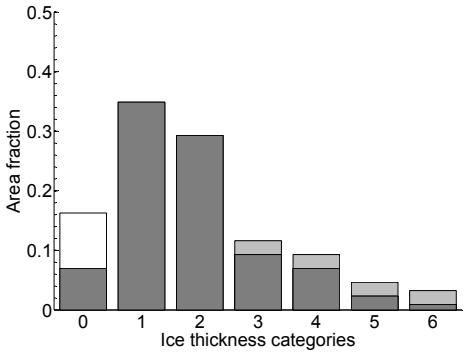

Figure 4.4: Example of ITD. The bars (dark gray) represent each category. This example shows how the volume of one single ice category (white area) is transferred to a finite number of thicker ice categories (light gray) by plastic deformation.

In the Baltic Sea modeling community, various horizontally integrated coupled column models are used for modeling the major oceanic features such as temperature and salinity structure with very satisfying results [e.g. Omstedt and Axell, 2003, Gustafsson, 2003]. One draw-back with all of these models is the lack of a physically correct description of ice dynamics in the ice sub-models. The thermodynamical ice growth is generally well handled, but the description of the ice dynamics is rater primitive. One example is the model by Omstedt and Axell [2003] where the the ice cover is described as a moving front. If the wind stress in the model is offshore and there exists open water, the front moves in free drift. The model does not account for the generated area of open water at the upwind coast and the size of open water area depends only of the location of the ice-front. When the wind stress in the model is onshore, the free drift is reduced by the compressive ice strength, following [Hibler, 1979]. The modeled ice strength is, however, not dependent on the ice thickness, instead it is normalized by the size of the ice cover. Furthermore, no ridging occurs in the model and the thickness is only thermodynamically controlled. Another example is the model by Gustafsson [2003], where the ice cover is separated into a number of categories with unique area coverage fractions, ice thickness, snow thickness and ice temperatures, following Björk [1992]. The ice velocity in the model depends on ice thickness so that the ice moves in free drift below a certain thickness. For thicker ice the wind speed/ice speed ratio decreases linearly up to a certain thickness, above which the ice cover becomes immobile. Deformation and ridging is implemented in the model such that the ridging is proportional to the ice speed. The leading idea behind that is that the ice cover must be deformed and ridge as soon as the ice starts to move when the basin is fully ice covered.

4.2 Observing sea ice motion and thickness

It is a demanding task to observe and monitor sea ice due to the complexity of the ice cover. This applies not only to the motion of the ice field, which in most cases is non-homogenous, but also the spatial distribution of the sea ice thickness, which varies due to mechanical processes. Considerable efforts have been made to make both qualitative and quantitative measurements of sea ice fields, but they are often time consuming and expensive to conduct. Some of the techniques used inside the Baltic Sea, such as SAR satellite and airborne Electro-Magnetic (EM), have given valuable information of the ice motion and thickness. Direct ice velocity observations with upward looking Acoustic Doppler Current Profiler (ADCP) have not previously been done inside the Baltic Sea. Successful measurements with ADCP have been, however, performed outside the Baltic Sea with interesting results [e.g. Belliveau et al., 1990, Shcherbina et al., 2005].

4.2.1 The ADCP

Observing ice drafts[4] with a bottom mounted ADCP, in combination with a depth gauge, is very accurate. An ADCP is a type of sonar that produces a record of water current velocities over a range of depths. The ADCP make use of 3 - 4 transducers made of ceramic or other piezo materials, which work in water similar to loud speakers and microphones in air. The transducers are directed in different angles so that the sound pulse they produce travels through the water in different directions. As the echo of the sound is returned by scatterers due to particles in the moving water, it shifts in frequency due to the Doppler effect. The Doppler shift is used to calculate the velocity shear in the water. By repetitive sampling of the return echo, and by gating the return data in time, the ADCP can produce a profile of water current shear over a range or bins of depths. In addition and most important for the present work, the ADCP can also measure the distance to and relative velocity of a "hard" surface, such as the sea bed or an ice surface, which gives a stronger echo than the water echoes do. This feature is most advantageous for the measurements of sea ice thickness and motion of the ice cover with an upward looking ADCP. The instrument stores ensembles of measurements from the beams and average it over a time step Δt. The highest detectable time resolution for the ADCP is given by the Nyquist-frequency $f_N = \frac{1}{2\Delta t}$, which can be translated to a length scale, $\lambda_N = 2u_{ice}\Delta t$ for a fixed ADCP observing moving ice with velocity u_{ice}. Structures with smaller length scale than this, e.g. ridges and leads, can not be resolved.

4.2.2 Data processing

Open water results in enhanced variance of the error velocity[5] [Belliveau et al., 1990] and hence it is quite clear whether there is open water or ice above the

[4] Ice draft refers to the ice thickness below the water level.
[5] Error velocity is a measure of the difference in vertical velocity between the four beams.

instrument. The open water increases the variance of the error velocity with a factor of 3, which was easily detected in the analysis.

Ice motion

Monitoring ice motion from just one point is not ideal for estimating sea ice dynamic in general, because it does not monitor shear effects in the ice cover. To include shear effects, at least 3 points are needed. However, the compressive force of the internal ice stress ($\nabla \cdot \sigma$) may be quantified from a simplified version of Eq. (4.4). Assuming that the ice motion is in steady-state, the ice velocity varies only in one direction, say x-direction, and $\mathbf{F}_{ext} = \tau_a + \tau_w$, Eq. (4.4) reduces to

$$\frac{\partial \sigma}{\partial x} + \tau_a + \tau_w = 0 \tag{4.5}$$

and it describes a balance between divergence in the internal ice stress, wind and water stress. Eq. (4.4) was derived assuming steady-state, which naturally is never strictly satisfied in real ice. However Eq. (4.4) can still be solved using a quasi[6] steady-state solution, which means that we theoretically apply steady-state for each time step imagining that the ice will remain its speed forever. However, the ice velocity will change the next time step if the forcing changes. If water velocity and wind speed are known for each time step, it is quite straight forward to compute the internal ice stress. Fig 4.5 shows two examples of calculated internal ice stress; one with approximately free ice drift (panel a) and one with high internal ice stress (panel b). For the free drift case, the $\nabla \cdot \sigma$-term is small and the ice velocity is forced by the wind stress. The relatively high water velocity is a result of the ice-water interaction. For the case where the $\nabla \cdot \sigma$-term is higher, the wind stress is not able to force the ice cover and the water velocity is also reduced.

Ice thickness

Even though the ice generally tends to float with ~10% of its volume above sea level, the density of the ice varies during the season. Cold ice, melting ice, ice with dry snow on top and ice with wet snow on top all have different density and buoyancy. The ice draft can be estimated using the distance between the ADCP and the bin with maximum echo intensity. It is possible to increase the resolution by fitting a curve to the vertical echo intensity distribution. Fig. 4.6 shows two possible solutions that can be used. It was shown in Shcherbina et al. [2005] that the modified Gaussian curve follows the echo intensity more qualitatively. In **Paper III**, the maximum point of the Gaussian curve was used to determine the distance from the instrument to the lower ice surface. This distance not only depends on the ice draft but also on the sea level. Since no depth gauge was deployed together with the ADCP that was used in **Paper**

[6]The term quasi implies that the system has not reached a "true" steady-state; we are merely neglecting the effect of changes in the slow process in computing the long-term behavior of the fast processes.

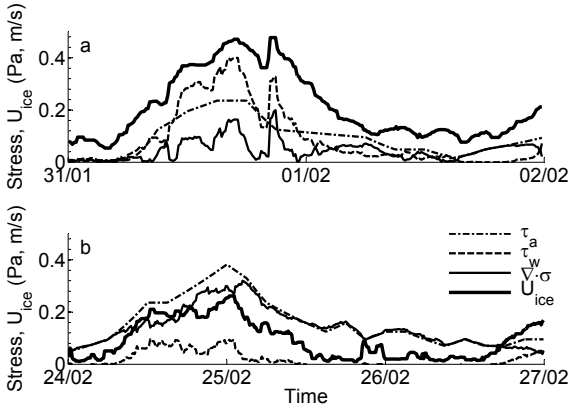

Figure 4.5: Stress vectors and ice velocity vectors during a period with free drift (panel a) and a period with high internal stress (panel b). The panels show magnitudes of the air stress, τ_a, the water stress, τ_w, the internal stress, $\nabla \cdot \sigma$ and the ice velocity, U_{ice}. All time series are low-pass filtered by a one hour moving median filter.

III, the actual ice draft was determined by subtracting the observed sea level from the distance estimated by the Gaussian curve (Fig. 4.7). Since the exact time of deployment and recovery was noted it was possible to match the sea level records from coastal mareograph stations[7] Ratan and Kalix, with ADCP measurements. The ice draft was then obtained as

$$H_{draft} = \left(H_{water} + \frac{\eta_{Ratan} + \eta_{Kalix}}{2}\right) - H_{BIN} - H_{ADCP} \qquad (4.6)$$

where the terms are defined in Fig. 4.7.

Ice thickness distribution

To compute the ice thickness distribution the average ice thickness was weighted by the length of a measuring cell, i.e. the average ice velocity multiplied with the length of the sampling interval. However, by using the average of four beams there is a risk of loosing thin or thick ice. The total footprint of the beams from the ADCP on the bottom of the ice depends on the water depth and beam angle and width. The actual footprint, in **Paper III**, on the ice gave a relatively large area when averaging the ice thickness. Also, features like ridges are assumed to have a small horizontal length scale and may pass by the the footprint to fast and thereby be underestimated in the sampled ice thickness distribution.

[7] A mareograph station is a recording sea level gauge, also known as a marigraph or tide gauge.

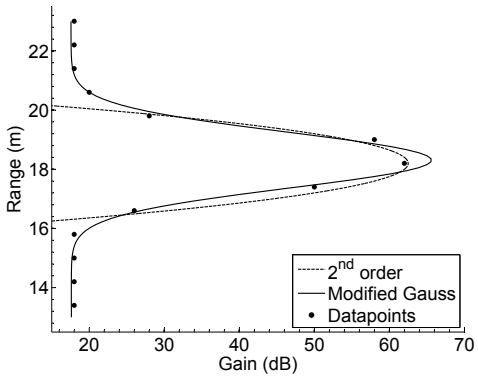

Figure 4.6: Estimation of the depth where maximum echo intensity appears using two different approaches, least-square fit of 2^{nd} degree and a modified gaussian curve.

4.2.3 Results from the ADCP measurements

Ice motion

The relation between wind forcing and ice motion was examined by assuming a linear dependence between the wind and ice velocity, thus by fitting a linear regression model to the data. The explained variance[8] was high, about 80%, in the beginning of the record and in March. This makes sense since the initial thin ice cover in early February and the subsequent weak internal ice stress, made the wind force easily moved the ice. This is also seen in the wind/ice speed ratio that was about 3%. Between these periods the explained variance was lower (40-60%) showing a less direct relation between ice and wind velocity as the ice thickness increased. The wind/ice speed ratio was also significantly lower (1-2%) during the same period. The explained variance appears to depend on the wind speed, with higher values for higher wind speeds. This is natural since a clearer wind dependence can be expected for strong winds when the wind

[8]Explained variance is how much of the variance of the ice motion that is explained by the linear model

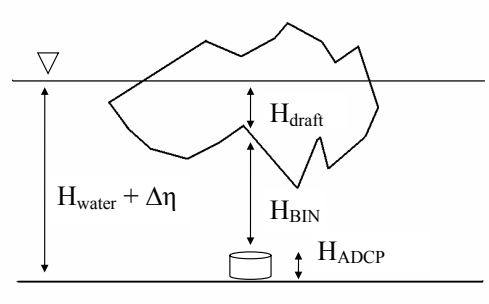

Figure 4.7: A sketch showing the ice draft measured by the ADCP. H_{draft} is the thickness of the ice draft, H_{BIN} is the estimated distance using the maximum echo intensity (Fig. 4.6) and H_{ADCP} is the height above bottom of the ADCP. $H_{water} + \Delta\eta$ is the water depth.

force can overcome the internal ice stress. However, the analysis of the data also shows that the ice speed was relatively small (< 10cm/s) for most of the time (70%) and stationary (< 0.5 cm/s) for 3% of the time. High ice speeds (20-50 cm/s) only occurred in relatively well-defined events, but made up a major part (70%) of the total drift distance. There is a general tendency that the ice is more mobile in events characterized by a large shift in wind direction. This is expected since open water is found on the upwind side of the basin after a strong event. It is also worth noting, based on wind fetch, motion data and Eq. (4.5), that a rough estimate gives a compressive ice strength of $9 \cdot 10^4 Nm^{-2}$. This is more than three times larger than the standard value $2.5 \cdot 10^4 Nm^{-2}$ regularly used in dynamic ice models. The location of the ADCP, close to the fast ice zone, implies a more rigid ice cover compared to the average mobility found in model results.

Ice draft

Fig. 4.8 shows the ice draft of the passing ice and the ice thickness distribution, as measured by the ADCP. Panel a) shows the ice thickness distribution for the period 11-17 February 2004, as can be seen, 61% of the ice passing by the ADCP was less than 1 meter in thickness. The maximum level ice measured in Bothnian Bay is typically 0.65-0.80 meter [Jacob and Omstedt, 2005], which implies that the total amount of ridges passing by the ADCP this particular period was 39% of the total record and the thickest ridge was 6.1 meter. It was shown in **Paper III** that up to 60% of the ice volume may consist of ridged ice during a sea ice season. This indicates that dynamical processes are important for the total ice production in the Bothnian Bay.

Ice motion in combination with thickness measurements from the ADCP gives quantitative measure of the ice thickness distribution including the ridges. The accumulated distance of the ice cover passing the ADCP was 600 km (see Fig. 4.8 panel b). This can be compared to the size of the basin, $\approx$ 200 x 300 km. It is also notable that the ice cover appears to move in events, coinciding with wind bursts. The ice drafts in panel c) are calculated based on the modified gaussian curve [Shcherbina et al., 2005] and it shows several ridges ($H_{draft} > 1$ meter) passing the instrument. It also has open or thin ice passing with little or no motion during February 13.

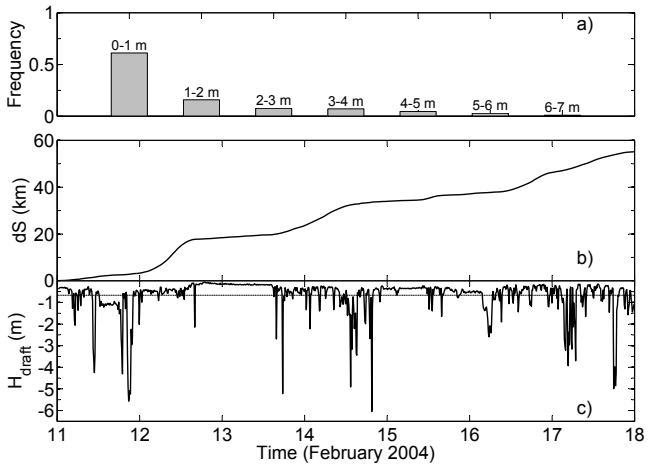

Figure 4.8: Details in the figure are collected during a short period in February 2004. Panel a) shows ice thickness distribution, panel b) shows the accumulated distance for the ice cover passing the ADCP and panel c) shows the calculated ice draft. Mean ice thickness for the period was 0.67 m.

4.3 Approaches to Mesoscale Sea Ice Modeling

The main purpose of developing the present type of dynamic sea ice model (**Paper IV**) was to improve the existing sub-models in the horizontal integrated coupled column models used in the Baltic Sea. The idea behind **Paper IV** was to combine (i) a classical example of an ice flow in an closed one-dimensional channel [e.g. Leppäranta, 2005, Chapter 7.2] and (ii) the results from studies of the Marginal Ice Zone[9], an area of enhanced ice drift, deformation and divergence (henceforth MIZ) [Leppäranta and Hibler, 1985, Leppäranta et al., 1989].

[9]Probably the most accepted definition of The marginal ice zone (MIZ) is that of Wadhams [1986] who describes it as "that part of the ice cover which is close enough to the open ocean boundary to be affected by its presence".

In the model, there are basically two scenarios for the wind influenced ice cover: Firstly the ice cover will move parallel to the coast, in the same manner as for the MIZ-flow, where the free drift is slowed down by the presence of a coastline. Secondly, if the moving ice encounter an obstacle downstream and the wind is strong enough, the ice will be deformed, in the same manner as for the closed one-dimensional channel. The mathematical formulation of the model will be described later in chapter 4.3.1.
The fundament of the sea ice model follows Björk [1992, 1997] where the ice cover is separated into a number n of ice categories $C_i, i = 0, n$. Each category is characterized by the five state variables:

$$C_i = (a_i, H_i, h_i, T_i, B_i) \tag{4.7}$$

where a_i is the fraction of the total area occupied by category i, H_i is the ice thickness, h_i the snow thickness and T_i the internal ice temperature. The new feature introduced is a property called formation direction B_i. Each time a new ice category is generated, a formation direction is given based on the direction of the wind generating the category. The use of this state variable is described below.
In the majority of two-dimensional sea ice dynamic models, H_{ice} is considered to be the mean ice thickness within the grid cell. The compressive ice stress is solved based on this assumption. The model outlined in **Paper IV**, however, assumes that the ice cover moves in a slab like fashion in the model domain. Hence, the ice dynamics is calculated for a single ice floe, or category [Leppäranta, 2005]. This concept of using only a single ice floe as H_{ice} and thereby consider the compactness $A \equiv 1$ will eventually allow us to calculate the ice velocity as a single velocity vector. This is the conceptual difference between the ice dynamics developed in this thesis and the ice dynamics used in e.g. the Arctic ocean [e.g. Flato and Hibler, 1995], GCM-models [e.g. Bitz et al., 2001] and in the Baltic Sea [e.g. Haapala and Leppäranta, 1996].
The main restriction with this concept is that the basin must be a semi-sized basin, i.e. the basin has to be large enough for the wind force to overcome the compressive ice strength and generate moving pack ice, but still small in comparison with weather systems so that the wind direction is approximately constant over the basin surface. The wind stress will then mainly pack the ice against the downwind coast and create an area of open water at the upwind coast. The open water area will freeze over rapidly during the winter, but as long as the new ice is relatively thin, it will remain as a weak part of the ice cover. The leading idea of the model presented in **Paper IV** is to utilize that the ice generally moves in a slab like fashion, with relatively small shearing motions in the central parts of a semi-sized basin like the Bothnian Bay. The model keeps track on the approximate location of where open water and new ice is formed by storing the formation direction (B), equal to the wind direction. The formation direction can then be used to determine the resistance of the ice to move according to subsequent wind forcing from various directions. By keeping track of the formation direction the local coordinate system can be rotated so

that it is aligned towards the weak part, each time the applied forcing generates ice motion. The model then solves for a single ice velocity vector. In the following, the internal ice stress is described as a medium with a viscous-plastic behavior (c.f. Fig. 4.2c).

4.3.1 Zonal sea ice drift

Here the mathematical expression for the two scenarios, MIZ-flow and closed channel flow, will be obtained. Fig. 4.9a shows a sketch of the classical one-dimensional steady-state channel approach. Under influence of a constant wind stress, the ice peals up against the channel end. The ice thickness will then increase in the channel length reaching a maximum at the channel end. The ice velocity is thus coupled to the ice thickness and decreases to zero in the channel end. With the prescribed concept of replacing the ice cover with a single ice floe (**Paper IV**) the ice floe will, if the wind force is stronger than the ice strength, be deformed at the channel end and create a pressure ridge (Fig. 4.9b). The thickness of the ice floe remains unchanged and the ice velocity is constant during the time the ice floe is deformed. The thickness of the pressure ridge is thus proportional to the ice velocity, since the ice volume is preserved.

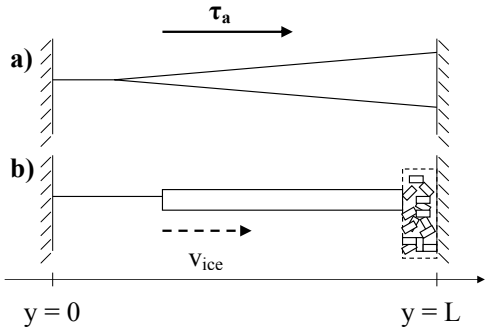

Figure 4.9: Panel (a) shows a side view of the classical one-dimensional channel approach where the ice thickness increases towards the channel end. Panel (b) shows a one-dimensional channel approach where the ice thickness is constant and a new pressure ridge is formed.

In ice covered seas, with an onshore wind and no obstacle downstream, a zone of typically sharp longitudinal boundary flow often emerges, so-called MIZ-flow. In a steady-state situation under quite general conditions a viscous-plastic rheology was used to define a compressive-to-shear stress ratio (γ) [Leppäranta and Hibler, 1985]. This ratio specifies the size and shape of the elliptic yield curve so the compressive ice stress can be related to shear ice stress according to

$$|\frac{\sigma_{compressive}}{\sigma_{shear}}| = \gamma \tag{4.8}$$

This notation can be used to reduce the two-dimensional flow in the MIZ to a one-dimension problem, e.g. a flow parallel to the shoreline without any stress derivatives orthogonal to the shoreline. Assuming that there is an obstacle downstream and that the MIZ is covered by a single ice floe, the approach for a single ice floe covered channel could then be applied for the MIZ flow as well. A sketch of the force balance in the MIZ flow is shown in Fig. 4.10.

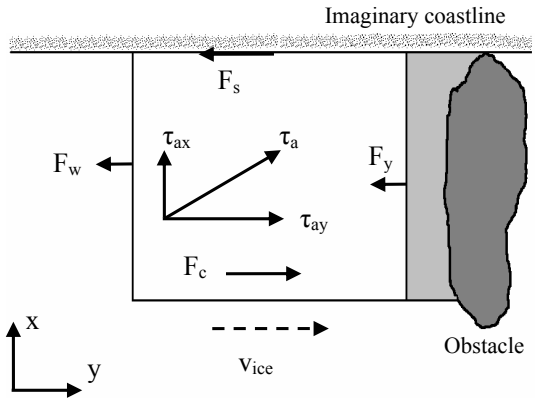

Figure 4.10: Sketch of the wind stress components and the force balance in the model during ice deformation. The coordinate system is defined so that x- and y-axis are parallel to the obstacle and the imaginary coast line, respectively. The model domain is given by the characteristic length scale, L, and the ice velocity is parallel to the coast line.

To move the ice parallel to the MIZ and towards the downstream obstacle, we introduce γ and the result is a one-dimensional balance of forces. In detail, the ice stress is balanced by the difference between the two wind-ice stress components and the water-ice stress. Using γ on Eq. (4.4) in steady-state the wind stress τ_a provides a compressive force $F_c = \tau_{ay} L$ and a shear force $F_s = |\gamma \tau_{ay}| L$, where L is the characteristic length scale, typical basin size. The ice strength is $F_y = \sigma$ and the water-ice force is $F_w = \rho_w C_w v_{ice}^2 L$. The balance of forces becomes

$$F_c = F_s + F_y + F_w \tag{4.9}$$

Now it is possible to solve for the ice velocity, thus

$$v_{ice} = \sqrt{\frac{(F_c - F_s) - F_y}{\rho_w C_w L}} \tag{4.10}$$

From Eq. (4.10) it can be seen that if the angle between the coastline and the wind stress τ_a changes, the ice velocity changes too. The direction of the wind stress as a function of the ice velocity is drawn in Fig. 4.11. Just a small change in this angle will drastically change the ice velocity, as the term $\left(F_c - F_s\right)$ will change.

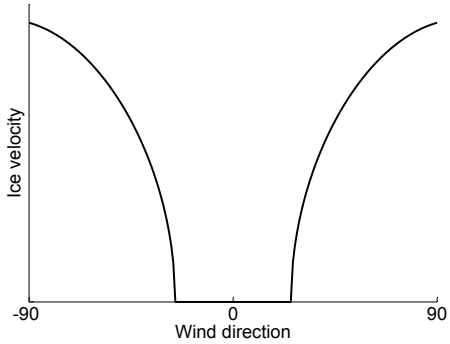

Figure 4.11: Ice speed as a function of wind direction. 0° is directed perpendicular to the MIZ.

4.3.2 The significance of the results

The study presented in **Paper IV** has some implications on sea ice modeling for the Baltic Sea. One of the characteristic features for the Bothnian Bay is the slab like motion of the ice cover, with formation of open water and new ice at the upwind coast. The sizes of these areas are critical quantities to be reproduced by ice models, because of the heat flux to the atmosphere and the subsequent large production of new ice. In addition, these will also represent the weakness in the ice cover (c.f. Fig. 4.10). If the modeled sizes of areas with open water or new ice are reasonably correct, one can also expect the rheology of the ice model to work properly. Areas of new ice and open water along the coast are relatively easy to identify in satellite images and should therefore be practical to use for model verification purposes (Fig. 4.12). An increased area of open water is likely to boost the deformation activity, and thereby the amount of pressure ridges formed, which is a problem for e.g. the naval traffic. It has also been shown that the amount of pressure ridges partly determines the spreading of seals, because seals tend to nurse cobs in the snow-drift captured by the ridges [Jüssi et al., 2008].

The results show that it is possible to simulate an entire ice season with an ice dynamic model that included simplified sea ice rheology.

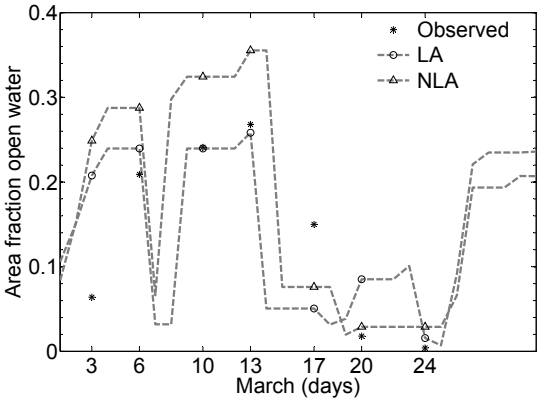

Figure 4.12: Observed area fraction of open water and simulated area fraction of open water, LA and NLA

Ice motion

If there are divergences in the ice cover, the motion is not homogenous which makes the comparison difficult. However, in a study of ERS-1 SAR images the ice motion in the central basin was shown to be rather uniform [Leppäranta et al., 1998]. This could also be seen in Zhang [2000] where five sea ice drifters was deployed near the Finish coast and all of them showed a counterclockwise motion. The results of these studies suggest that ice motion observed in a single point (**Paper IV**) can be used as validation for the model.

Compressive ice strength

In the linear approach, the compressive ice strength that best explain observed ice velocity is $P^* = 19$ kN/m^2. This is comparable to common values found in the literature [Leppäranta, 2005]. The optimal compressive ice strength for the non-linear approach was $\mu_0 = 22$ N/kg. A similar value for μ_0 was obtained in the coupled one-dimensional sea ice-ocean model for the Baltic Sea [Omstedt, 1990] while Overland and Pease [1988] obtained a value of only $\mu_0 = 1.6$ N/kg. This relatively low value was based on oceanic sea ice, which is weaker than brackish sea ice. By adjusting this ice strength for the Baltic Sea conditions a value close to the one found in **Paper IV** was obtained. Compressive ice strength in oceanic conditions is known to be softer due to e.g. higher contents of brines[10], and it is not unusual that the value of e.g. P^* for the linear approach is 5 times lower than for brackish conditions.

[10]Brine is small pockets inside the ice containing water with very high salinity, trapped during the ice formation.

Compressive-to-Shear ratio

The optimal value of γ (Eq. (4.8)) obtained in **Paper IV** was comparable to the one obtained in Leppäranta et al. [1989], but only half of the commonly used value in general ocean sea ice modeling. Fig. 4.13 shows the sensitivity of explained variance, E[11] for simulations with different combinations of P^*, μ_0 and γ. The variation in E indicates that in the Bothnian Bay, shear effects are of less importance and that compressive forces control much of the ice dynamic. This can be seen in Fig. 4.13a) and b) left side, where changes in P^* or μ_0 (solid lines) have a higher variability than changes in γ (dashed lines). This result is also in line with earlier observations of the ice dynamics [Leppäranta, 2005].

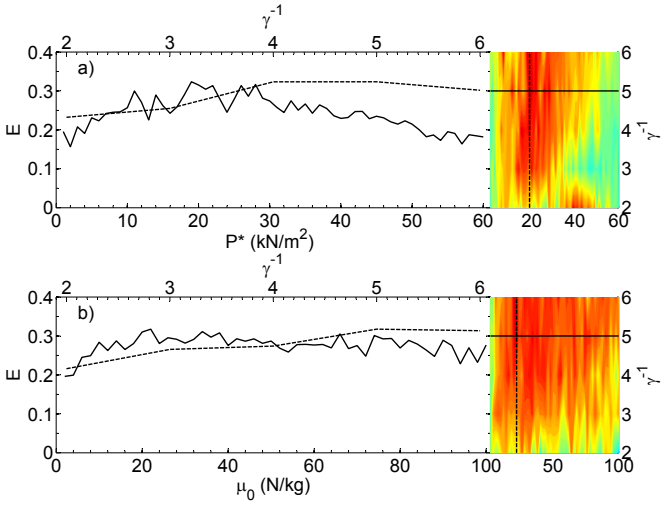

Figure 4.13: Figure showing explained variance, E, for the best cases found in the model for linear and non-linear approaches. Left side of panels illustrates E for the lines (solid and dashed) in the right side of panels. Red indicate high E. Pane a) shows E for linear approach when $\gamma^{-1} = 5$ (solid line) and when $P^* = 19$ kN/m^2 (dashed line). Panel b) shows E for non-linear approach when $\gamma^{-1} = 5$ (solid line) and when $\mu_0 = 22$ N/kg (dashed line).

Dynamical ice production

The total ice production is shown in Fig. 4.14. As can be seen there are significant difference between the linear and non-linear approaches and there is a tendency that the ice production, also the ice thickness distribution, is different (see **Paper IV**). There is also a tendency that the non-linear approach gives higher ice production for years with low wind speed and low temperature.

[11] In statistics, explained variance measures the proportion to which a mathematical model accounts for the variance of a given data set.

Weak winds favors larger ice production in the non-linear approach since the weaker thin ice causes more open water to be generated resulting in higher ice production. Also the temperature needs to be lower than normal in order to maintain a high heat loss to the atmosphere for weaker wind. The dynamic ice production found in the model typically increased the ice volume with more than 50% compared to the pure thermodynamic growth. Thus dynamic processes give a significant contribution to the total ice volume in the Bothnian Bay.

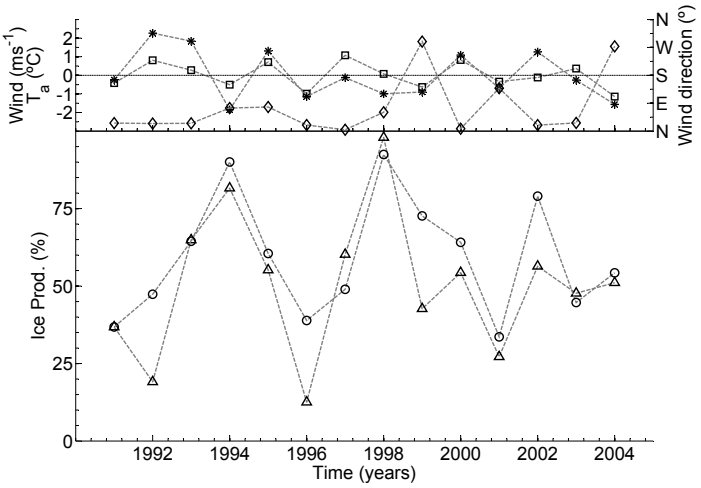

Figure 4.14: Upper panel shows anomalies of the five month means of air temperature ($*$), wind speed ($\square$) and wind direction ($\Diamond$) for each year over the period 1991-2004. Anomalies are defined as deviations from the mean over the entire period. The lower panel shows ice production each year over the period. Curve marked $\triangle$ is for the linear approach and curve marked with $\circ$ is for the non-linear approach.

5 Future Outlook

During my time as a PhD student, several ideas of improvements and future research have emerged while working with the different issues. A brief selection of some of the thoughts and ideas that I hope to elucidate in the future is shown below.

In **Paper I**, one of the conclusions made was that the accuracy of the different terms is unsolved both for water and for heat budgets. The ice sub model presented in **Paper IV** could potential improve the heat cycle in horizontally integrated but vertically resolved coupled models in the Baltic Sea [e.g. Omstedt and Axell, 2003, Gustafsson, 2003]. If it turns out that the heat cycle is improved by a realistic opening and closing of the ice cover, ice models are critical for modeling coupled air-sea-ice models because of the dynamic that opens and closes the ice cover. If the heat cycle is not improved, the focus must be shifted towards other processes more important in the heat balance, associated with opening of the ice cover and the arising dynamical ice production.
Another potent improvement to the heat cycle is to test the parameter settings that gave the interesting result of a negative $P - E$ in an arid tropical area, where the precipitation rate would virtually be equal to zero. In this way, it may be possible to obtain the correct contribution of the different terms in the water and heat budget, in particular for E.
However, the 30-year period that were simulated in **Paper I** may not have been long enough to constitute a base, upon which conclusions could be drawn about the development of the integrated water temperature compared to the warming of the atmosphere, because the whole water column was included in the analysis, not only the surface layer. Due to the heat capacity of water, it would take a long time to observe changes in water temperature as a result of the increased air temperature. The residence time for the Baltic Sea water is > 26 year and a long-time simulation over several decades is probably needed to be able to make conclusions about this issue.

The results obtained in **Paper II** showed that the magnitude of the forcing was an underestimated factor. Because of the scares numbers of synoptic stations, the wind and pressure fields are smooth and without any small-scale pressure anomalies and strong wind events. A simple sensitivity test revealed that with a 50% increase in the wind, the magnitude of the dissipation due to wavedrag

was comparable with earlier estimates. The frequency response < 10 hour was not resolved properly by the model and this could also be a caused by model forcing. The magnitude and frequency response would benefit from forcing the model with a high resolution wind and pressure field for the Baltic Sea [e.g. Kauker and Meier, 2002].
The objective of **Paper II** was to investigate the probability of internal wave generation due to baroclinic wavedrag using a so-called local step model. The validity of the step model was recently challenged by Laurent et al. [2003], where they argued for a resolution dependency in the internal wave generation. The formulation of the wavedrag of the local step model implies a limiting size of the grid size

$$\lim_{\Delta s \to 0} \frac{1}{\Delta s}$$

The limiting size have not yet been investigated, but there has been some efforts to the subject where the result showed that the major part of the energy transfer occur over steep topography [e.g. Gustafsson, 2002]. However, further work on the model sensitivity towards the grid size is needed to thoroughly validate the results presented here.

The results from **Paper III** pointed out that the method used was promising in providing more quantitative and qualitative ice thickness measurements. Unfortunately no depth gauge was present in the instrument setup, complicating the ice draft estimate unnecessarily. In addition to a pressure gauge, a combination of surface measurements would solve the whole ice thickness problem because the total ice thickness is made up of ice draft under and over the water level. However, the major challenge is obviously the problem with the synchronization in time calculating the real ice thickness. Another more feasible task is to deploy 3 or more ADCPs on the bottom of the sea. 3 ADCPs would capture the entire field and thereby capture the shear effects, instead of only one single point limited to the compressive effects. This would provide the divergence and convergence for the moving ice field. The enhanced data set will provide us with more insight and increase our knowledge on sea ice dynamics and kinematics.
Due to the shape of the ice drafts of deformed ice, they induce form drag that increases the ice water stress significantly and generates turbulence well below the water surface that may increase the overall mixing in the upper water mass. In ice-covered seas, this aspect has to the present authors best knowledge not been investigated in the Bothnian Bay. Analyzing the present data set with regards to water-ice drag and turbulent mixing should give some interesting aspects to mixing in ice-covered seas. To quantify this enhanced mixing would be a interesting task to achieve.

One of the more prominent shortcomings in **Paper IV**, is the stiffening of the ice cover seen in the velocity at the end of the season. From mid April (see. Fig. 8 in **Paper IV**), little or no motions are seen despite observations of strong events. The promising results obtained by the model may be useful as

an improvement to coupled 1D air-ocean models therefore this aspect deserves to be investigated further. One of the solutions to the shortcoming could be found in the melting process, which may not be sufficient solved in the model [Timco and Johnston, 2002]. The study concentrates on the increased volume of brine pockets due to melting and it would be of great interest to incorporate that knowledge into the model. Another obvious aspect of the shortcoming is the lack of multiple categories of open water. Open water will also increase the mobility of the ice cover because the melting of the individual ice categories will emerge all over the ice field. The number of categories with open water will increase; hence the probability of free drift is enlarged. Furthermore, another type of ice, is so-called *rafted ice*, which is not included in the model. *Rafted ice* is two ice floes of relatively thin ice thickness that drifts toward each other but due to the thickness of the floes, they do not create pressure ridges but glides on-top of each other. This will increase the ice velocity because thin ice tends to raft instead of ridge. There is of course reasons to believe that the effect is reduced due to the relative low ice strength. Nevertheless, such a process must be incorporated into a future model.

Sea ice extent and sea ice dynamics are important factors for the existence of seals in e.g. the Bothnian Bay [Jüssi et al., 2008]. Studies have shown that sea ice features like ridges favor the breeding of seals, because drifting snow tends to accumulate in between the ridges. Seals utilize these pockets of snow, making undetected breeding chambers for puppies with easy access to the water. Also the locations of these features are correlated with patchiness of different seal populations living on the ice. To be able to simulate the evolution of different seal populations, modeling sea ice extent and deformation activity during a long time period would give useful information. The model presented in **Paper IV** together with the improvements mentioned above, offers a possibility to simulated these features and would be another interesting study to do.

Acknowledgments

And now it is time to let out the superlatives and express my gratitude to those who made it possible for me to accomplish this demanding task. First of all I wish to thank my supervisor Bo Gustafsson for all the faith and support you have given me throughout this elapsed time. I am also most grateful to my other supervisor Göran Björk, for the clarifying and sometimes harsh but yet very righteous comments on drafts and model concepts. You gave me the opportunity to drink after-beer on the night-shift onboard the icebreaker Oden in the Arctic, which I will remember with gratitude. I would also mention Anna Wåhlin for reading and giving me valuable comments to improve the draft to this thesis onboard the same icebreaker Oden, this time on a cruise to the Antarctica. And, finally, the colleague's at the former department of Oceanography, thank you for making this voyage memorable.

During my time on the department, I have been involved in several courses, both as an assistant and as a teacher. One of the courses I must mention is "Vattenundersökningar". Even if it was quit intense from time to time, it has taught me a lot on how to think and how to solve problems. I specially wish to thank Anne-Marie Larsson for introducing me to this course. And also the boat crew on RV Skagerak deserves to be mentioned for making the boat trips very entertaining during the mini-expeditions and other field expeditions I have had the opportunity to participate on.

And my family which means the world to me; Anna, this education would never have happened, without your inspiration. You introduced me to this world with your dreams of the whales when we visited Andenes. You supported me and cared for me when the task was troublesome; you deserve a big warm hug! Simen, waking up with your blue eyes and the big smile in front of my face 4^{30} in the morning is beyond description! You give me so much tenderness and joy. Sadly, my parents did not stay to see you or the grand final, but I believe that they witnessed it anyway.

And Freia, you where always a happy girl. I enjoyed our long walks and the time we spent together. Very, very sad, you passed away all too soon, only 4-years old... Then you came along, Saga, our fragile little fairy tale. With your loud

greeting ceremony which leaves no one untouched, I really enjoy spending time with you. Pusekatten, from nearly newborn found under the firewood in the garden, you have become the the ultimate of your kind. Blizard Rouges, you give the word proud a new meaning, I have never met anyone like you! I am for ever grateful that I said yes to the clinic and experienced the true potential in you. I hope we will have lots of fun in the future. Fernando Gracioso, Lynx Toyboy and Miss Vintage Sparkle, you all contribute to the ultimate relaxation I needed in between my work hour. And of course; Sessan, Pricken and Emil, you all have a new home here with us now.

Bibliography

L. Arneborg. Mixing efficiencies in patchy turbulence. *Journal of Physical Oceanography*, 32(5):1496–1506, 2002. doi: 10.1175/1520-0485(2002)032<1496:MEIPT>2.0.CO;2.

L. B. Axell. On the variability of Baltic Sea deepwater mixing. *Journal of Geophysical Research*, 103(C10):21,667–21,682, 1998. doi: 10.1029/98JC01714.

BALTEX. Baltic Sea Experiment BALTEX. initial implementation plan. Technical Report International BALTEX Secr. Publ. Series, ISSN 1681-6471, No. 2., 84 pp., International BALTEX Secretariat. GKSS Geestacht, Germany, 1995.

BALTEX. The main BALTEX Experiment 1999-2001 BRIDGE. strategic plan. Technical Report International BALTEX Secr. Publ. Series, ISSN 1681-6471, No. 9., 78 pp., International BALTEX Secretariat. GKSS Geestacht, Germany, 1997.

D. Belliveau, G. Bugden, B. Eid, and C. Calnan. Sea ice velocity-measurements by upward-looking doppler current profilers. *Journal of Atmospheric and Oceanic Technology*, 7(4):596–602, 1990. doi: 10.1175/1520-0426(1990)007<0596:SIVMBU>2.0.CO;2.

S. Bergström and B. Carlsson. River runoff to the Baltic Sea: 1950 - 1990. *Ambio*, 23(4-5):280–287, 1994.

C. M. Bitz, M. M. Holland, A. J. Weaver, and M. Eby. Simulating the ice-thickness distribution in a coupled climate model. *Journal of Geophysical Research*, 106(C2):2441–2463, 2001. doi: 10.1029/1999JC000113.

G. Björk. On the response of the equilibrium thickness distribution of sea ice export, mechanical deformation, and thermal forcing with application to the Artic Ocean. *Journal of Geophysical Research*, 97(C7):11287–11298, 1992. doi: 10.1029/92JC00814.

G. Björk. The relation between ice deformation, oceanic heat flux, and the ice thickness distribution in the Artic Ocean. *Journal of Geophysical Research*, 102(C8):18681–18698, 1997. doi: 10.1029/97JC00789.

G. Björk, C. Nohr, B. G. Gustafsson, and A. E. B. Lindberg. Ice dynamics in the Bothnian Bay as inferred from ADCP measurements. *Tellus A*, 60(1): 178–188, 2008. doi: 10.1111/j.1600-0870.2007.00282.x.

M. Coon, G. Maykut, R. Pritchard, D. Rothrock, and A. Thorndike. Modeling the pack ice as an elastic-plastic material. *AIDJEX Bulletin*, 24:1–105, 1974.

G. D. Egbert and R. D. Ray. Significant dissipation of tidal energy in the deep ocean inferred from satellite altimeter data. *Nature*, 405:775–778, 2000. doi: 10.1038/35015531.

G. D. Egbert and R. D. Ray. Semi-diurnal and diurnal tidal dissipation from TOPEX/Poseidon altimetry. *Geophysical Research Letters*, 30(17):1907, 2003. doi: 10.1029/2003GL017676.

G. M. Flato and W. D. Hibler, III. Ridging and strength in modelling the thickness distribution of Arctic Sea ice. *Journal of Geophysical Research*, 100 (C9):18611–18626, 1995. doi: 10.1029/95JC02091.

C. Garrett. Internal tides and ocean mixing. *Science*, 301(5641):1858–1859, 2003. doi: 10.1126/science.1090002.

C. Garrett and L. St Laurent. Aspects of deep ocean mixing. *Journal of Oceanography*, 58(1):11–24, 2002. doi: 10.1023/A:1015816515476.

A. E. Gill. *Atmosphere-Ocean dynamics*, volume 30 of *International Geophysics Series*. Academic Press, 1982. ISBN 0-12-283522-0.

M. Granskog, H. Kaartokallio, H. Kuosa, D. N. Thomas, and J. Vainio. Sea ice in the Baltic Sea - a Review. *Estuarine Coastal And Shelf Science*, 70(1-2): 145–160, 2006. doi: 10.1016/j.ecss.2006.06.001.

B. G. Gustafsson. A time-dependent coupled-basin model of the Baltic Sea. Technical Report C47, Department of Oceanography, 2003.

B. G. Gustafsson. *Dynamics of the seas and straits between the Baltic and the North Seas.* Ph.D. Thesis, A23, Deparment of Oceanography, Earth Science Center, Göteborg University, Sweden, 1997.

B. G. Gustafsson and H. C. Andersson. Modeling the exchange of the Baltic Sea from the meridional atmospheric pressure difference across the North Sea. *Journal of Geophysical Research*, 106(C9):19731–19744, 2001. doi: 10.1029/2000JC000593.

K. E. Gustafsson. Computations of the energy flux to mixing processes via baroclinic wave drag on barotropic tides. *Deep-Sea Research I*, 48(10):2283–2295, 2001. doi: 10.1016/S0967-0637(01)00008-5.

K. E. Gustafsson. *Tidal energy losses by baroclinic wave drag and their importance for the thermohaline circulation.* Ph.D. Thesis, A80, Deparment of Oceanography, Earth Science Center, Göteborg University, Sweden, 2002.

J. Haapala and M. Leppäranta. Simulating the Baltic Sea ice season with a coupled ice-ocean model. *Tellus A*, 48A(5):622–643, 1996. doi: 10.1034/j.1600-0870.1996.t01-4-00003.x.

W. D. Hibler, III. A viscous sea ice law as a stochastic average of plasticity. *Journal of Geophysical Research*, 82(27):3932–3938, 1977. doi: 10.1029/JC082i027p03932.

W. D. Hibler, III. A dynamic thermodynamic sea ice model. *Journal of Physical Oceanography*, 9(4):815–846, 1979. doi: 10.1175/1520-0485(1979)009<0815:ADTSIM>2.0.CO;2.

E. C. Hunke and J. K. Dukowicz. An elastic-viscous-plastic model for sea ice dynamic. *Journal of Physical Oceanography*, 27(9):1849–1867, 1997. doi: 10.1175/1520-0485(1997)027<1849:AEVPMF>2.0.CO;2.

IRIS. Ice Ridging Information for Decision Making in Shipping Operations, 2003. URL `EU project homepage: http://www.tkk.fi/Units/Ship/Research/Iris/Public/`.

D. Jacob and A. Omstedt. BALTEX PHASE 1: 1993-2002, state of the art report. Technical Report BALTEX Publication No. 31, 181 pages, 2005.

S. R. Jayne and L. C. St Laurent. Parameterizing tidal dissipation over rough topography. *Geophysical Research Letters*, 28(5):811–814, 2001. doi: 10.1029/2000GL012044.

M. Johnsson, J. A. M. Green, and A. Stigebrandt. Baroclinic wave drag from two closely spaced sills in a narrow fjord as inferred from basin water mixing. *Journal of Geophysical Research*, 112:C11002, 2007. doi: 10.1029/2006JC003694.

M. Jüssi, T. Härkönen, E. Helle, and I. Jüssi. Decreasing ice coverage will reduce the breeding success of Baltic Grey Seal (halichoerus grypus) females. *Ambio*, 37(2):80–85, 2008. doi: 10.1579/0044-7447(2008)37[80:DICWRT]2.0.CO;2.

K. Karlsson. A 10 year cloud climatology over Scandinavia derived from NOAA advanced very high resolution radiometer imagery. *International Journal of Climatology*, 23(9), 2003. doi: 10.1002/joc.916.

F. Kauker and H. E. M. Meier. Reconstructing atmospheric surface data for the period 1902-1998 to force a coupled ocean-sea ice model of the Baltic Sea. Technical Report RO 99, Swedish Meteorological and Hydrological Institute, 2002.

L. S. Laurent, S. Stringerb, C. Garrettc, and D. Perrault-Joncasd. The generation of internal tides at abrupt topography. *Deep Sea Research Part I*, 50(8): 987–1003, 2003. doi: 10.1016/S0967-0637(03)00096-7.

A. Lehmann and H. H. Hinrichsen. The importance of water storage variations for water balance studies of the Baltic Sea. *Physics and Chemistry of the Earth, Part B: Hydrology, Oceans and Atmosphere*, 26(5-6):383–389, 2001.

M. Leppäranta. *The drift of sea ice*. Springer in ass. with Praxis Publishing, Chichester, UK, 2005. ISBN 3-540-40881-9.

M. Leppäranta and W. D. Hibler, III. The role of plastic ice interaction in marginal ice zone dynamics. *Journal of Geophysical Research*, 90(C6):11899–11909, 1985. doi: 10.1029/JC090iC06p11899.

M. Leppäranta, M. Lensu, and Q.-M. Lu. Shear flow of sea ice in the Marginal Ice Zone with collision rheology. *Geophysica*, 25(1-2):57–74, 1989.

M. Leppäranta, Y. Sun, and J. Haapala. Comparison of sea-ice velocity fields from ERS-1 SAR and a dynamical model. *Journal of Glaciology*, 44(147): 248–262, 1998.

M. Leppäranta. The dynamics of sea ice. In M. Leppäranta, editor, *Physics of Ice-Covered Seas*, volume 1 of *Lecture notes from a summer school in Savonlinna, Finland 6-17 june 1994*, pages 305–342. Helsinki University Press, 1998.

M. Leppäranta and R. Hakala. The structure and strength of first-year ice ridges in the Baltic Sea. *Cold Regions Science and Technology*, 20:295–311, 1992. doi: 10.1016/0165-232X(92)90036-T.

M. Leppäranta and A. Omstedt. A review of ice time series of the Baltic Sea. *Publications Instituti Geographici Universitatis Tartuensis*, 84:7–10, 1999.

B. Liljebladh and A. Stigebrandt. *The contribution of the surface layer via internal waves to the energetics of deepwater mixing in the Baltic*. Paper III, Ph.D. Thesis A56, Deparment of Oceanography, Earth Science Center, Göteborg University, Sweden, 2000.

H. E. M. Meier. Modeling the age of Baltic Sea water masses: Quantification and steady state sensitivity experiments. *Journal of Geophysical Research*, 110(C02006):1–14, 2005. doi: 10.1029/2004JC002607.

H. E. M. Meier and R. Doscher. Simulated water and heat cycles of the Baltic Sea using a 3D coupled atmosphere-ice-ocean model. *Boreal Environmental Research*, 7(4):327–334, 2002.

J. W. Miles and L. N. Howard. Note on a heterogeneous shear flow. *Journal of Fluid Mechanics*, 20(2):331–336, 1964. doi: 10.1017/S0022112064001252.

A. Omstedt. A coupled one-dimensional sea ice-ocean model applied to a semi-enclosed basin. *Tellus A*, 42(5):568–582, 1990. doi: 10.1034/j.1600-0870.1990.t01-3-00007.x.

A. Omstedt and L. B. Axell. Modeling the variations of salinity and temperature in the large Gulfs of the Baltic Sea. *Continental Shelf Research*, 23(3-4):225–394, 2003. doi: 10.1016/S0278-4343(02)00207-8.

A. Omstedt and C. Nohr. Calculating the water and heat balances of the Baltic Sea using ocean modelling and available meteorological, hydrological and ocean data. *Tellus A*, 56:4, 2004. doi: 10.1111/j.1600-0870.2004.00070.x.

A. Omstedt and A. Rutgersson. Closing the water and heat cycles of the Baltic Sea. *Meteorologische Zeitschrift*, 9:57–64, 2000.

A. Omstedt, B. Gustafsson, J. Rodhe, and G. Walin. Sea modelling to investigate the water and heat cycles in GCM and regional climate models. *Climate Research*, 15(-):95–108, 2000. doi: 10.3354/cr015095.

A. Omstedt, J. Elken, A. Lehmann, and J. Piechura. Knowledge of the Baltic Sea physics gained during the BALTEX and related programmes. *Progress in Oceanogrphy*, 63(1-2):1–28, 2004. doi: 10.1016/j.pocean.2004.09.001.

A. Omstedt, Y. Chen, and K. Wesslander. A comparison between the ERA40 and the SMHI gridded meteorological databases as applied to Baltic Sea modelling. *Nordic Hydrology*, 36(4-5):369–380, 2005.

J. E. Overland and C. H. Pease. Modeling ice dynamics of coastal seas. *Journal of Geophysical Research*, 93(C12):15619–15637, 1988. doi: 10.1029/JC093iC12p15619.

K. L. Polzin, J. M. Toole, J. R. Ledwell, and R. W. Schmitt. Spatial variability of turbulent mixing in the abyssal ocean. *Science*, 276(5309):93–96, 1997. doi: 10.1126/science.276.5309.93.

A. Rutgersson, A. Omstedt, and J. Räisänen. Net precipitation over the Baltic Sea during present and future climate conditions. *Climate Research*, 22(1): 27–39, 2002. doi: 10.3354/cr022027.

M. Samuelsson and A. Stigebrandt. Main characteristics of the long-term sea level variability in the Baltic Sea. *Tellus A*, 48(5):672–683, 1996. doi: 10.1034/j.1600-0870.1996.t01-4-00006.x.

S. B. Savage. Two-component sea-ice thickness redistribution model. *Cold Regions Science and Technology*, 51(1):20–37, 2008. doi: 10.1016/j.coldregions.2007.06.002.

A. J. Semtner Jr. A model for the thermodynamic growth of sea ice in numerical investigations of climate. *Journal of Physical Oceanography*, 6(3):379–389, 1975. doi: 10.1175/1520-0485(1976)006<0379:AMFTTG>2.0.CO;2.

A. Shcherbina, D. Rudnick, and L. Talley. Ice-draft profiling from bottom-mounted ADCP data. *Journal of Atmospheric and Oceanic Technology*, 22 (8):1249–1266, 2005. doi: 10.1175/JTECH1776.1.

B. Sjöberg and A. Stigebrandt. Computations of the geographical distribution of the energy flux to mixing processes via internal tides and the associated vertical circulation in the ocean. *Deep-Sea Research*, 39(2A):269–291, 1992. doi: 10.1016/0198-0149(92)90109-7.

M. W. Stacey. The interaction of tides with the sill of a tidally energetic inlet. *Journal of Physical Oceanography*, 14(6):1105–1117, 1984. doi: 10.1175/1520-0485(1984)014<1105:TIOTWT>2.0.CO;2.

A. Stigebrandt. Physical Oceanography of the Baltic Sea. In F. Wulff, L. Rahm, and P. Larsson, editors, *A systems analysis of the Baltic Sea*, pages 19–74. Springer Verlag, 2001.

A. Stigebrandt. Regulation of vertical stratification, length of stagnation periods and oxygen conditions in the deeper deepwater of the Baltic proper. *Meereswissenschaftliche Berichte*, 54:69–80, 2003.

A. Stigebrandt. Vertical diffusion driven by internal waves in a sill fjord. *Journal of Physical Oceanography*, 6:486–495, 1976. doi: 10.1175/1520-0485(1976)006<0486:VDDBIW>2.0.CO;2.

A. Stigebrandt. Some aspects of tidal interactions with fjord constrictions. *Estuarine Coastal Marine Science*, 11:151–166, 1980.

A. Stigebrandt. Resistance to barotropic tidal flow in straits by baroclinic wave drag. *Journal of Physical Oceanography*, 29:191–197, 1999. doi: 10.1175/1520-0485(1999)029<0191:RTBTFI>2.0.CO;2.

A. Stigebrandt and B. G. Gustafsson. Response of the Baltic Sea to climate change-theory and observations. *Journal of Sea Research*, 49(4):243–256, 2003. doi: 10.1016/S1385-1101(03)00021-2.

A. Stigebrandt, H. U. Lass, B. Liljebladh, P. Alenius, J. Piechura, R. Hietala, and A. Beszczýnska. DIAMIX-An experimental study of diapycnal deepwater mixing in the virtually tide-less Baltic Sea. *Boreal Environmental Research*, 7(4):363–369, 2002.

A. Svansson. Physical and chemical oceanography of the Skagerrak and the Kattegat, 1. Open sea conditions. Technical Report 1, Fishery Board of Sweden, Marine Research Institute, 1975.

U. Svensson. PROBE, Program for Boundary Layers in the Environment: System description and manual. Technical Report RO 24, Swedish Meteorological and Hydrological Institute, 1998.

A. S. Thorndike, D. A. Rothrock, G. A. Maykut, and R. Colony. The thickness distribution of sea ice. *Journal of Geophysical Research*, 80(33):4501–4519, 1975. doi: 10.1029/JC080i033p04501.

G. Timco and M. Johnston. Ice strength during the melt season. In *Proceedings of the 16th IAHR International Symposium on Ice*, volume 2, pages 187–193, Dunedin, New Zealand, 2002.

J. S. Turner. *Buoyancy effects in fluids*. Cambridge Monographs on Mechanics and Applied Mathematics Series. Cambridge University Press, 1973. ISBN 0-521-29726-5.

J. Uotila. Observed and modelled sea-ice drift response to wind forcing in the northern Baltic Sea. *Tellus A*, 53A(1):112–128, 2001. doi: 10.1034/j.1600-0870.2001.01172.x.

P. Wadhams. The seasonal ice zone. In N. Untersteiner, editor, *The Geophysics of Sea Ice*, volume 146: of *NATO ASI, Ser. B*, pages 825–991. Plenum Press, 1986.

Z. H. Zhang. Comparisons between observed and simulated ice motion in the northern Baltic Sea. *Geophysica*, 36(1-2):111–126, 2000.

Part II

Papers I-IV

Paper I

Tellus (2004), 56A, 400–414
Printed in UK. All rights reserved

TELLUS

Calculating the water and heat balances of the Baltic Sea using ocean modelling and available meteorological, hydrological and ocean data

By ANDERS OMSTEDT* and CHRISTIAN NOHR, *Earth Sciences Centre-Oceanography, Göteborg University, PO Box 460, SE-405 30 Göteborg, Sweden*

(Manuscript received 24 September 2003; in final form 16 March 2004)

ABSTRACT

In this paper we aim to analyse Baltic Sea water and heat balances for the BALTEX/*BRIDGE* study period and to put these into a climatic perspective. The study period—the three years starting October 1999—was a time of enhanced observational and modelling activities in the Baltic Sea region and of the major field activity of BALTEX Phase I programme. The present study follows the example of earlier work, where Baltic Sea modelling was used as a tool for synthesizing available data and closing the water and heat balances. The modelling approach was validated with independent data sets of observations from salinity and temperature. The model simulation was also compared with the coupled atmosphere–Baltic Sea model system, HIRLAM–BALTEX, which was run in a delayed data assimilation mode.

The results indicate that accurate long-term net water and net heat balances (mean errors over decadal time scales are about 600 $m^3\ s^{-1}$ and 2 $W\ m^{-2}$ respectively) can be calculated using current Baltic Sea modelling and meteorological and hydrological data available from the BALTEX data centres. The accuracy of the individual terms in the water and heat balances is, however, still unknown. The study illustrated that negative net precipitation rates are possible, with the year 2002 standing out from the rest of the 30-yr study period. The calculated inter-annual variability of the net heat loss between atmosphere and Baltic Sea during the BALTEX/*BRIDGE* period indicated large variations ($\pm 10\ W\ m^{-2}$). It has also been shown that the Baltic Sea annual mean temperature has not increased during the studied period despite an atmospheric warming of 1 °C. The reason has been explained by the heat balance that indicated no trend in the Baltic Sea net heat loss.

1. Introduction

The Global Energy and Water Experiment (GEWEX) was developed within the framework of the World Climate Research Programme (WCRP). Its aim was to improve understanding of global, regional, and local processes that exchange water and energy in the climate system. Within GEWEX, several continental-scale experiments were initiated in various regions, including the Baltic drainage basin. In the Baltic Sea Experiment (BALTEX), the whole drainage basin includes a region that has about 90 million inhabitants. Planning for the BALTEX programme (Fig. 1) started in early 1990 and has now been running for 10 yr (BALTEX, 1995). Several key questions about water and heat cycles were raised in the programme. For example, is net precipitation over the Baltic Sea positive (freshwater being added to the sea) or negative?

The main experiment of BALTEX Phase I period (1993–2002) was called *BRIDGE*, to signal the collaboration of scientists from various scientific backgrounds from around the Baltic Sea (BALTEX, 1997). The *BRIDGE* experiment was performed from October 1999 to March 2002, the first three months being the pilot phase and the remaining 27 months the basic observational phase.

Different aspects of the Baltic Sea water and heat cycles are given in Bengtsson (2001), Jacob (2001), Lehmann and Hinrichsen (2002), Meier and Döscher (2002), Omstedt and Rutgersson (2000), Raschke et al. (2001), Hennemuth et al. (2003) and Ruprecht and Kahl (2003). Several recent results related to the understanding of these cycles can also be found in special issues of journals emerging from some BALTEX Study Conferences. These include issues of *Tellus* (48A, No. 5, 1996), *Meteorological and Atmospheric Physics* (77, 2001), *Meteorologische Zeitschrift* (9, 2000), and *Boreal Environment Research* (7, 3 and 4, 2002).

In the present paper we examine the water and heat balances of the Baltic Sea during the *BRIDGE* period in relation to

*Corresponding author.
e-mail: Anders.Omstedt@gvc.gu.se

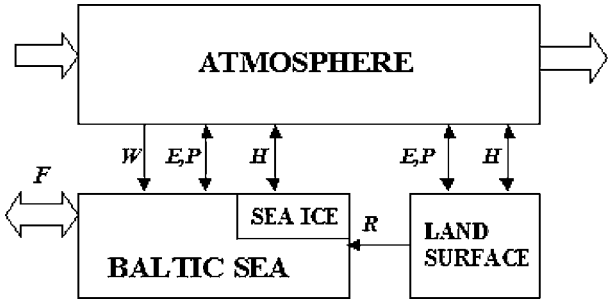

Fig 1. The BALTEX box where W indicates wind, E and P are evaporation and precipitation, H denotes heat fluxes, F is inflows and outflows, and R is river runoff.

current climatic conditions (1970–2002), using the PROBE-Baltic ocean model (Omstedt and Axell, 2003). The paper is intended to contribute to improving our basic understanding of the Baltic Sea and to validating climate models (as in Omstedt et al., 2000). The approach follows that of some earlier studies (Omstedt et al., 1997; Rutgersson et al., 2002), where Baltic Sea modelling is used as a tool for synthesizing available data and to improve our physical understanding of the marine system. The study asks three basic questions. (1) What are the values of the individual terms of the water and heat balances during the BALTEX/*BRIDGE* period and how do they vary over time? (2) How accurately can these balances be calculated? (3) Can detection of climate change signals be done more easily for the water and heat-cycle components compared to standard parameters such as temperature?

The outline of the paper is as follows. In Section 2 we provide the data and models used. Then, in Section 3, the current modelling system is validated using independent data obtained from the Baltic Sea. The meteorological conditions during the study period are discussed in Section 4. In Section 5 we present the results regarding the water and heat cycles. In Section 6 we compare the HIRLAM–BALTEX system and the present modelling approach. In Section 7 we provide a summary and some conclusions.

2. Material and methods

The meteorological forcing data were extracted from the SMHI gridded data base, which has a time resolution of 3 h and $1^\circ \times 1^\circ$ grid resolution, available from the BALTEX Hydrological Data Centre (BHDC). The meteorological parameters include U- and V-components of geostrophic winds, temperature at 2 m, relative humidity at 2 m, total cloudiness, surface pressure and precipitation. River runoff data were also made available from BHDC as monthly mean data. The water level forcing from the North Sea was calculated on the basis of daily mean sea levels from the Kattegat. For validation, vertical profiles of observed salinity and temperature were extracted from the Swedish national database, SHARK, and made available by the Ocean Data Centre of BALTEX (ODCB). Annual maximum ice extent values were made available by the Finnish Institute of Marine Research. For details about the forcing and validation data, the reader is referred to Omstedt and Axell (2003).

In calculating the water and heat cycles, the PROBE-Baltic model was used without any data assimilation. This is a process-oriented, time-dependent coupled basin model, a description of which is given in Omstedt and Axell (2003). For purposes of comparison, monthly mean atmospheric fluxes from the HIRLAM–BALTEX reanalysis were also used. The HIRLAM–BALTEX model uses a special version of the atmospheric model, HIRLAM (Källén 1996), where data assimilation and a coupled ice–ocean model for the Baltic Sea are used (Gustafsson et al., 1998). In the HIRLAM–BALTEX model, calculated sea surface temperatures were adjusted (twice a week) through a nudging process using observed sea surface temperatures obtained from the marine service at SMHI.

3. Validation

3.1. Modelled and observed mean salinity

The model simulation has been carefully examined using a large number of measured salinity and temperature profiles. Some examples are given in Fig. 2, which depicts both observed and calculated data from three sub-basins in the Baltic Sea. The figure illustrates that the model results follow the observations closely and that the observations are irregularly distributed in space and time. Typical values of mean error and root mean square (rms) error for sea surface salinity are −0.3 and 0.5 psu for individual sub-basins (Omstedt and Axell 2003).

To draw conclusions as to the quality of the water balance calculations, we need to examine the observed and modelled mean salinity of the whole Baltic Sea, excluding the Kattegat and the Belt Sea (Fig. 3). We used the mean Baltic Sea salinity (vertically as well as horizontally integrated) as a measure of the quality of the water balance. The calculated mean salinity was compared with the estimated mean salinity by Winsor et al. (2001, 2003). The estimated mean salinity was calculated by first using salinity profiles from all major sub-basins of the Baltic Sea for the 1977–1987 period, a period with good coverage in all sub-basins. Then this mean was compared with data from the central Baltic Sea (BY15), a station that has observations for more than 100 yr. The comparison illustrated that the station BY15 well represents the Baltic Sea and based on data from this station the mean salinity was estimated for the 20th century. From the data presented in Fig. 3 we can note that the present calculated mean salinity is 0.57 less than that calculated by Winsor et al. (2003), which is due to different means when initializing the ocean model. The salinity in our paper is given according to the Practical Salinity Scale defined as a pure ratio without dimensions or units. This is the standard since 1981 when UNESCO adopted the scale. After adjusting the initial value in the Winsor curve to that calculated

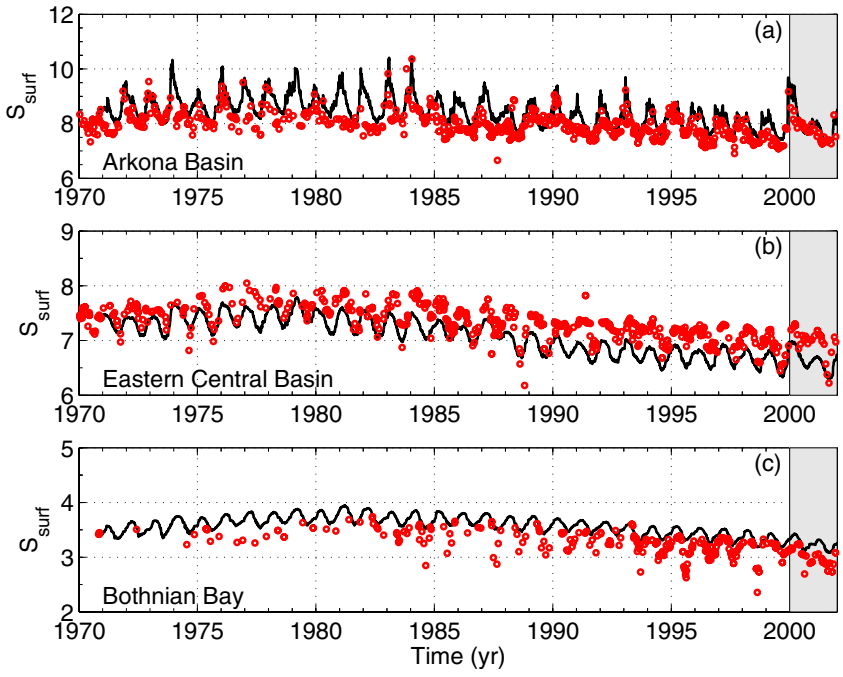

Fig 2. Observed (circles) and modelled (lines) sea surface salinity (S_{surf}) from the Arkona Basin (a), the Eastern Gotland Basin (b), and Bothnian Bay (c). The BALTEX/*BRIDGE* period is marked.

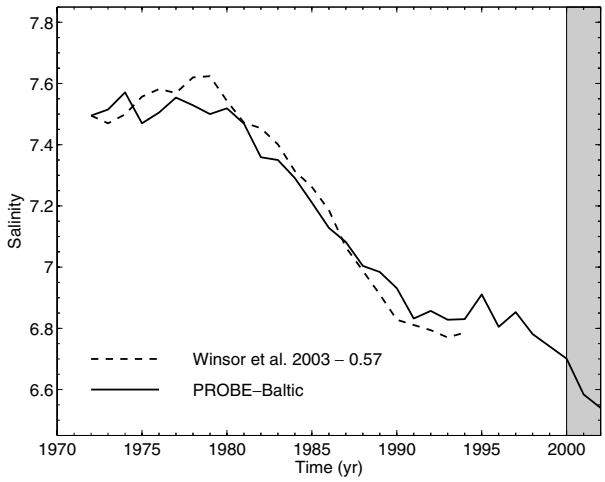

Fig 3. Observed (dashed line) and modelled (solid line) annual variation of Baltic Sea mean salinity. The BALTEX/*BRIDGE* period is marked.

from 1972, we find that the curves follow each other closely. We now translate the error between calculated and observed mean salinities into an estimation of the accuracy in the net water balance. Referring to salt conservation principles, the freshwater change (ΔQ) associated with a salinity difference (ΔS) can be written as

$$\Delta Q = -\frac{V\,\Delta S}{S\,\Delta t}, \tag{1}$$

where V is the water volume, S is the salinity and Δt is the time period. With $V = 2 \times 10^{13}$ (m^3) and Δt equal to 1 yr, the mean and rms errors in the freshwater balance are less than 600 and 6000 m^3 s^{-1}, respectively. The mean error is calculated as the sum of the differences between calculated and observed annual mean salinities divided by the number of observations. The rms error is calculated as the square root of the sum of the square of the difference between calculated and observed annual means divided by the number of observations. If we can trust the Winsor estimated mean salinity, the mean error in the water balance calculation is much less than the river runoff (4% of the river runoff), less than the net precipitation (40% of the net precipitation rate) and of the same size as the estimated ground-water flow to the Baltic Sea (Peltonen, 2002), a term often neglected in water balance studies. This is of course a positive result, indicating that the net freshwater balance averaged over decades is quite accurate. The rms error is 10 times as large as the mean error; which implies that water balance studies on time-scales shorter than a decade could have quite large errors. The accuracy of the individual terms in the water balance is, however, not known.

The observed mean salinity could include errors, as the sampling of the salinities in the Baltic Sea was not well distributed in time and space, particularly in the large gulfs. Further work is therefore needed in analysing and calculating the observed Baltic Sea mean salinity, as this information is of great value in water balance studies.

3.2. *Modelled and observed mean water temperature*

In this section we examine both the observed and modelled temperatures. Figure 4 depicts the match between the observed and modelled sea surface temperatures from three

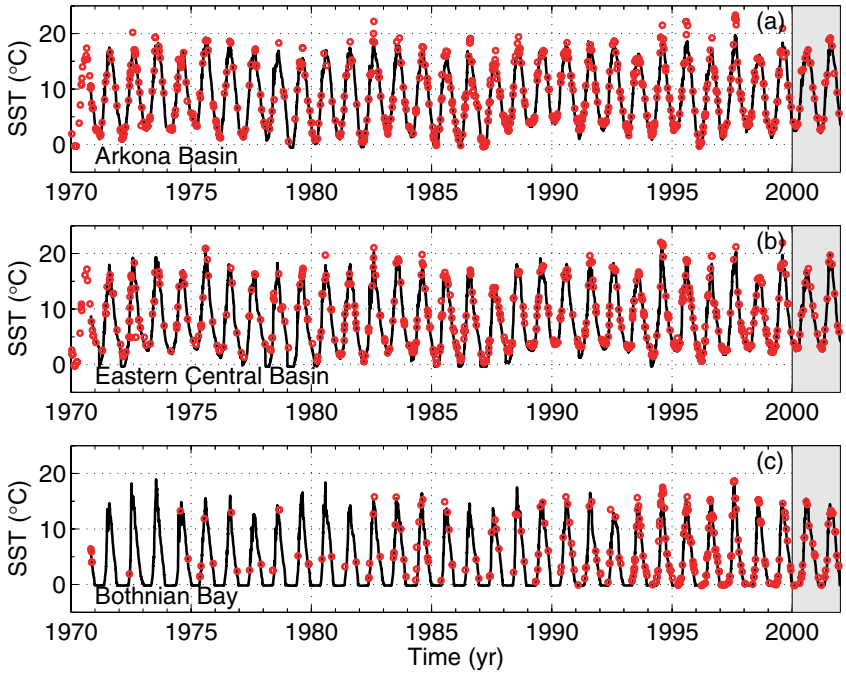

Fig 4. Observed (circles) and modelled (lines) sea surface temperatures (SST) from the Arkona Basin (a), the Eastern Gotland Basin (b), and Bothnian Bay (c). The BALTEX/*BRIDGE* period is marked.

sub-basins. Sea surface temperature is of major importance in the atmosphere–ocean heat exchange, and accurate modelling is needed. The calculated sea surface temperatures closely match the observed data, while the modelled data fills in for missing observations in a realistic manner. Typical values of mean error and rms error for sea surface temperatures are −1 °C and 1–2 °C for the individual sub-basins (Omstedt and Axell, 2003).

We then consider the mean (vertically as well as horizontally integrated) water temperature of the Baltic Sea (Fig. 5). The observed and calculated mean temperatures follow each other closely without any drift. In this case, the observed Baltic Sea mean temperature time series is calculated from 1744 measured profiles from the major sub-basins in the Baltic Sea.

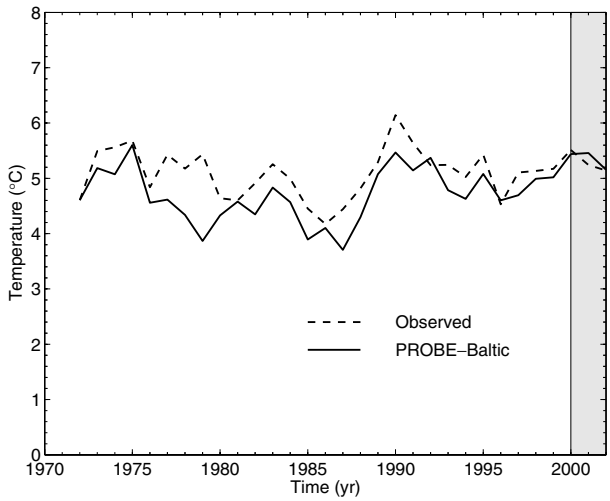

Fig 5. Observed (dashed line) and modelled (solid line) annual variation of Baltic Sea mean water temperature. The BALTEX/*BRIDGE* period is marked.

The temperature error (difference between observed and calculate annual mean temperatures), ΔT, can be related to fluxes through the following relation:

$$\Delta F = \frac{\rho C_{\mathrm{p}} \Delta T D}{\Delta t}. \qquad (2)$$

Here, ΔF is the corresponding error in the atmosphere–ocean net heat flux, ρ is the water density, C_{p} is the specific heat of water, D is the mixed layer depth, and Δt is the studied time period. Using eq. (2) and calculating the mean and the rms flux errors based on the differences between observed and calculated annual mean temperatures, the errors become equal to 2 and 3 W m^{-2}, respectively. We may thus conclude that the net heat balance can be modelled with good precision. The errors in the individual terms in the heat balance are probably one order of magnitude larger.

In calculating the observed Baltic Sea mean temperature, data from stations in the deeper parts of the sub-basins have been used. The effects of the coastal zones are therefore not included, but over inter-annual and decadal time-scales these effects are probably quite small. This is because coastal zones represent only a fraction of the total sea volume, and because the seasonal temperature cycle is generally wider in range in the coastal zones, temperatures being both warmer and colder than in the open sea. However, effects on the coastal zone, including up- and down-welling, need further consideration when calculating the mean observed Baltic Sea temperature.

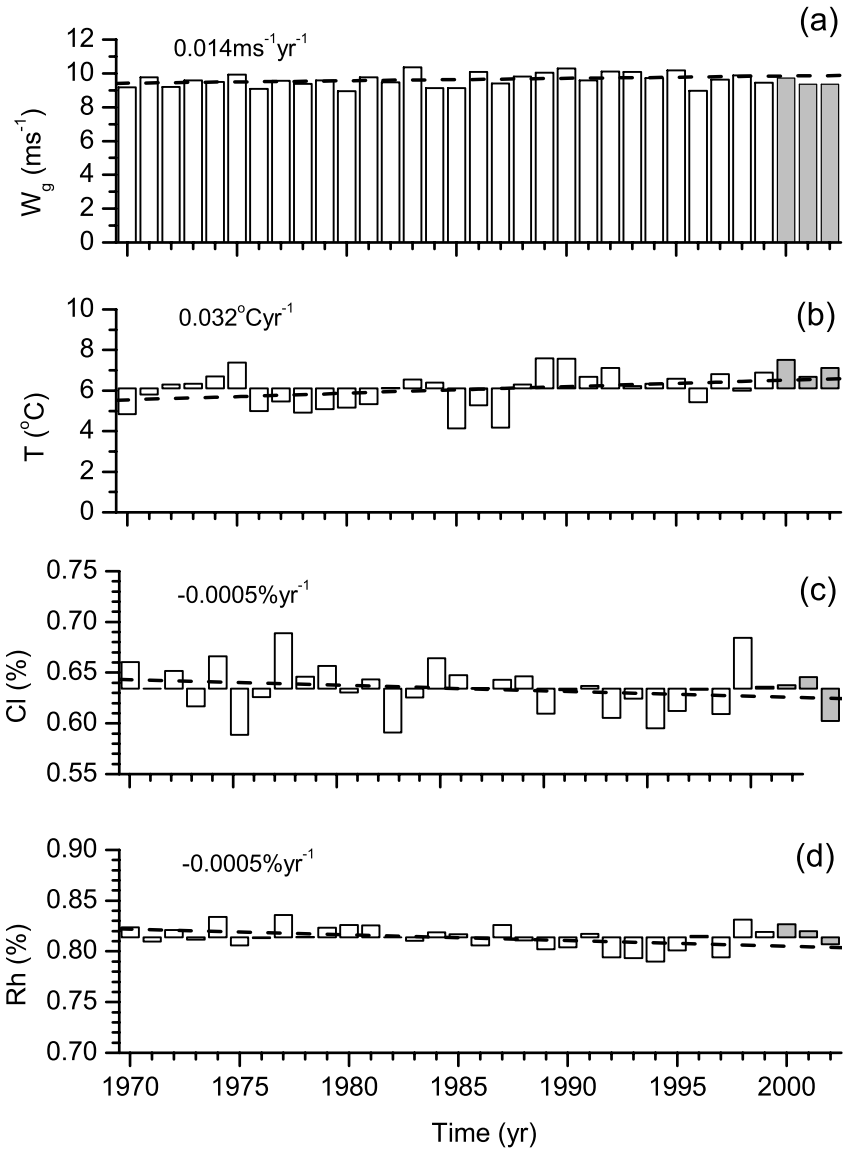

Fig 6. The Baltic Sea horizontal averaged geostrophic wind speed (a), air temperature (b), total cloudiness (c) and relative humidity (d). The figure depicts yearly means calculated over the Baltic Sea surface region (the Belt Sea and the Kattegat excluded) based on the SMHI meteorological data base. The dashed lines indicate the linear trends and the BALTEX/*BRIDGE* period is marked.

Validation of model simulations of sea ice (not shown) indicates that the model realistically simulates sea ice with mean and rms errors of 10 and 41 $\times$ 10^3 km^3, respectively. With a mean error of 10 $\times$ 10^3 km^3 the relative error becomes about 5%. This is close to the estimated accuracy of the observed maximum ice extent data based on modern ice mapping techniques using satellite data.

4. Baltic Sea mean meteorology conditions

Before analysing the various components of the water and heat cycles, we first examine the meteorological mean parameters (horizontally averaged over the Baltic Sea inside the Danish Straits) during the study period. The meteorological data were extracted from the SMHI gridded data base and horizontal mean fields were calculated over the Baltic Sea area.

The horizontal Baltic Sea mean geostrophic wind speed is depicted in Fig. 6a, where we can observe how the annual mean wind speed varies and note that the wind speed has tended to increase over the studied period. Examining this in more detail (not shown) reveals that the annual westerly wind component has increased, while the annual southerly wind component has decreased. The results are in accordance with studies of trends in near-surface flow over the Baltic Sea by Pryor and Barthelmie (2003). From National Center for Environmental Prediction/National Center for Atmospheric Research (NCEP/NCAR) reanalysis fields over the Baltic region, they found that the wind had increased during the study period, with the largest annual increase in the south-west of the Baltic Sea (+0.025 m s^{-1} yr^{-1}). Increased frequency of storms during the second half of the 20th century has been observed on the coast of Estonia (Orviku et al., 2003). Trends of storms (1880–1998)

derived from pressure data have been examined by Alexandersson et al. (2000). They found that the stormy period centred around 1990 had been broken.

Observation of the horizontal Baltic Sea mean air temperature (Fig. 6b) indicates an increasing annual temperature. Temperatures during the BALTEX/*BRIDGE* period were warm, almost similar to temperatures around 1990. Mean cloudiness (Fig. 6c) decreased slightly, with particularly low values occurring in 2002. Relative humidity (Fig. 6d) also indicated a slight decreasing trend.

Analysis of the Baltic Sea horizontal annual mean meteorological forcing parameters indicates that the BALTEX/*BRIDGE* period did not stand out from the range of variation of the last 30 yr, but showed warm annual means with reduced geostrophic wind speeds. In 2002, the mean cloudiness and relative humidity were also reduced. For long-term climate change statistics over the Baltic Sea region, the reader is referred to Omstedt et al. (2004), where the Baltic Sea climate conditions over the past 200 yr are analysed.

5. Results

5.1. Water balance

The water balance involves many processes related to the hydrological cycle in the atmosphere, the land and the ocean climate systems. Starting from the volume conservation principle, we can write the Baltic Sea water balance as follows (Omstedt and Rutgersson, 2000; Stigebrandt, 2001):

$$A_s \frac{dz_s}{dt} = Q_i - Q_o + (P - E)A_s + Q_r + Q_{ice} + Q_{rise} + Q_T + Q_S + Q_g. \quad (3)$$

Here, A_s is the surface area of the Baltic Sea, z_s is the water level of the Baltic Sea, Q_i and Q_o are the inflows and outflows through the Baltic entrance area, P and E are the precipitation and evaporation rates, Q_r is the river runoff, Q_{ice} is the volume change due to ice advection from the Baltic Sea, Q_{rise} is the volume change due to land uplift, Q_T and Q_S are the volume changes due to thermal expansion and salt contraction, and Q_g is the ground-water inflow.

In the following discussion, we neglect contributions from Q_{ice} (of the order of 10^2 m^3 s^{-1}; Omstedt and Rutgersson, 2000), Q_{rise} (of the order of 10^1 m^3 s^{-1}; Omstedt and Rutgersson, 2000), Q_T, Q_S (small on annual time-scales) and Q_g (of the order of 10^2 m^3 s^{-1}; Peltonen, 2002).

An estimate of Q_S can be derived by considering that a change of 1 in salinity corresponds to about a 1-cm change in sea level (the slope from Bothnian Bay to Skagerrak drops about 35 cm as the salinity increases from zero to almost 35). Winsor et al. (2001, 2003) indicate that Baltic Sea salinity varies about 1 per 30 yr. We estimate then that the volume change due to salt contraction on an annual basis is about 1/15 cm or of the order of 10^1 m^3 s^{-1} (Baltic Sea surface area inside the entrance sills is about 370 000 km^2). Thermal expansion due to heating and cooling may cause seasonal variation in volume flow of the order of 10^3 m^3 s^{-1} (Stigebrandt, 2001), but on an annual scale the volume flow is at least one order of magnitude less. The left term in eq. (3) is the change in water storage (positive for volume increase) and is important for short-term estimations of the water balance (Lehmann and Hinrichsen, 2001). See Table 1 for estimates of the various terms.

The calculated long-term means of the various components of the water balance are presented in Table 2. In the table we distinguish between the BALTEX/*BRIDGE* period, defined as

Table 1. Estimated annual mean volume flows for the Baltic Sea (order of magnitude). The flows are denoted by: inflow (Q_i), outflow (Q_o), net precipitation ($P - E$), river runoff (Q_r), the volume change due to ice advection from the Baltic Sea (Q_{ice}), the volume change due to land uplift (Q_{rise}), the ground-water inflow (Q_g), the volume changes due to thermal expansion (Q_T) and salt contraction (Q_S). A_s denotes the Baltic Sea surface area

Q_i (m^3 s^{-1})	Q_o (m^3 s^{-1})	$Q_o - Q_i$ (m^3 s^{-1})	$(P - E)A_S$ (m^3 s^{-1})	Q_r (m^3 s^{-1})	Q_{ice} (m^3 s^{-1})	Q_{rise} (m^3 s^{-1})	Q_g (m^3 s^{-1})	Q_T (m^3 s^{-1})	Q_S (m^3 s^{-1})
10^5	-10^5	-10^4	10^3	10^4	-10^2	-10^1	10^2	$\pm 10^2$	$\pm 10^1$

Table 2. Mean water balance for the Baltic Sea (the Belt Sea and the Kattegat excluded) average (in units of 10^3 m^3 s^{-1}). The flows are denoted as river runoff (Q_r), net precipitation ($P - E$), inflow (Q_i), outflow (Q_o), and storage change. A_s denotes the Baltic Sea surface area

Author	Q_i (m^3 s^{-1})	Q_o (m^3 s^{-1})	$Q_o - Q_i$ (m^3 s^{-1})	Q_r (m^3 s^{-1})	A_s $(P - E)$ (m^3 s^{-1})	Storage change (m^3 s^{-1})	Period
Present	38.44	56.32	17.88	14.88	2.05	−0.95	BALTEX/*BRIDGE* 2000–2002
Present	42.75	59.41	16.76	14.96	1.70	−0.11	1979–2002

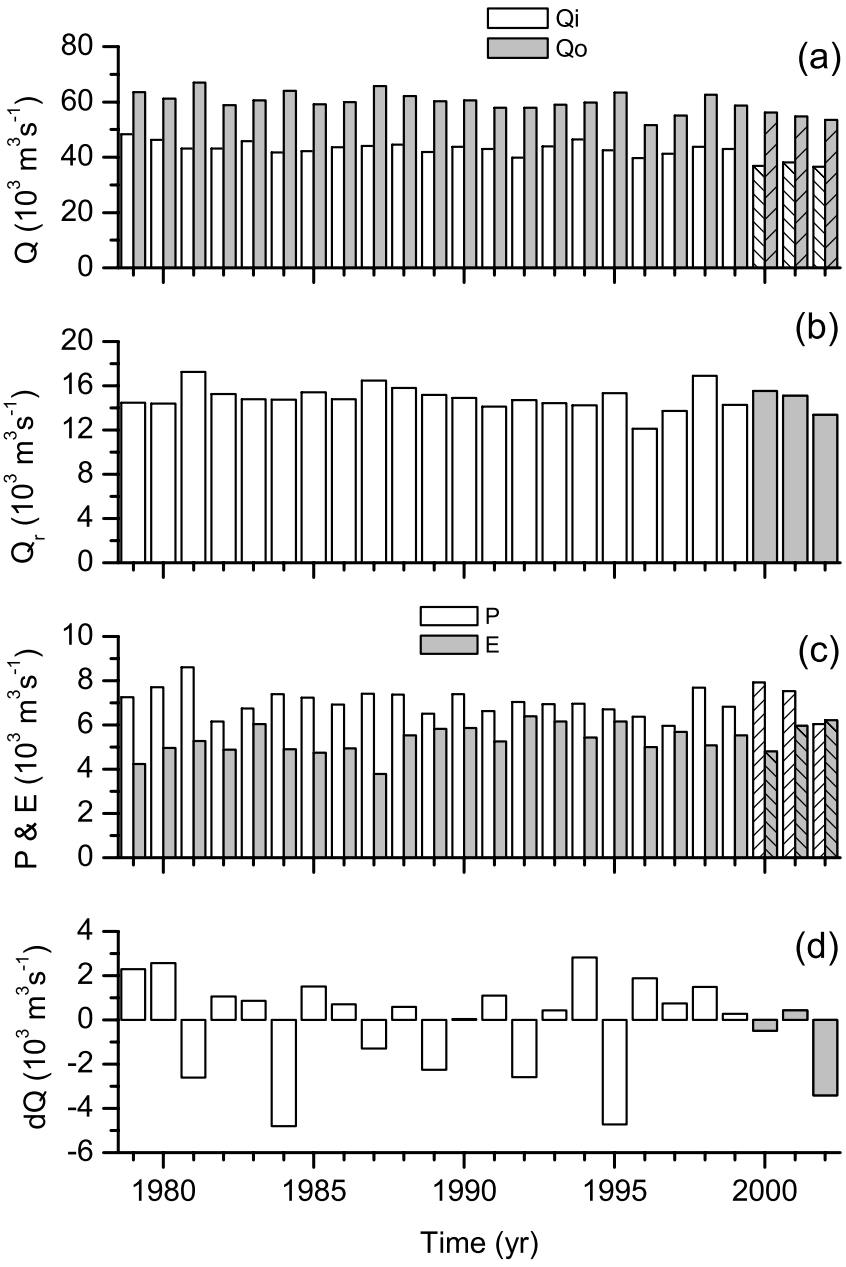

Fig 7. Baltic Sea (excluding the Kattegat and the Belt Sea) annual means of inflows and outflows (a), river runoff (b), precipitation and evaporation (c), and net volume change (d). The BALTEX/*BRIDGE* period is marked.

the three years from 2000 to the end of 2002, and the reference period, illustrated by the period 1979–2002. The annual means are presented in Fig. 7, and the monthly means of the major water balance components are given in Appendix A.

The values calculated for the various water balance components are in good accordance with earlier studies (e.g. Omstedt and Rutgersson 2000; Omstedt and Axell, 2003). The major component comprises inflows and outflows through the Baltic Sea entrance area. The largest inflow was 48 268 m^3 s^{-1} in 1979, while the largest outflow was 67 008 m^3 s^{-1} in 1981. The latter year corresponded to the maximum freshwater inflow, with 17 242 and 3329 m^3 s^{-1} being contributed by river runoff and net precipitation, respectively. The wettest year was 1981, when the sum of net precipitation and river runoff was 20 571 m^3 s^{-1}, while the driest year was 1996, when total freshwater inflow was 13 493 m^3 s^{-1}. The years 1981 and 1996 were also the years with the largest and smallest annual mean net outflows, calculated as 23 902 and 11 928 m^3 s^{-1}, respectively.

The water balance values for the BALTEX/*BRIDGE* period are in line with those of the longer time period with one important exception. The net precipitation was calculated as negative during 2002. This clearly deviates from the findings of earlier studies which have analysed net precipitation over other recent periods. This is due to the unusually warm year, 2002, as

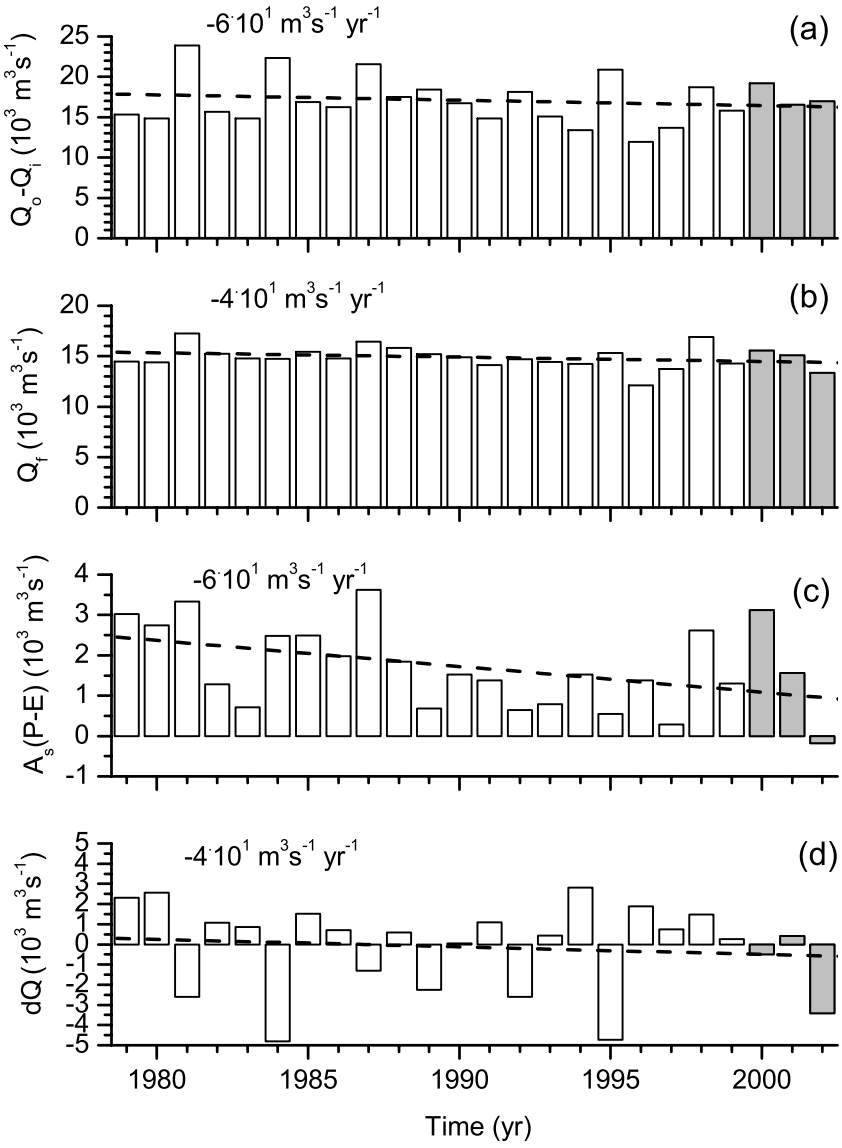

Fig 8. Baltic Sea (excluding the Kattegat and the Belt Sea) annual means of the water balance components: difference between outflows and inflows (a), river runoff (b), net precipitation (c), and net volume change (d). The dashed lines indicate the linear trends and the BALTEX/*BRIDGE* period is marked.

indicated in Section 4, which had a particularly warm and dry autumn with low winds. The autumn of 2002 also witnessed an unusual inflow event, when warm, saline bottom water flowed into the Baltic Sea (Piechura and Beszczynska-Möller, 2003).

The trends in the different water balance components are illustrated in Fig. 8. In general, we can notice a negative trend in the net outflow, the river runoff and the net precipitation. The decreasing net outflow ($Q_o - Q_i$) balances the reduction in river runoff, net precipitation, and storage change.

5.2. Heat balance

From the heat conservation principles, we can write the heat balance equation (Omstedt and Rutgersson 2000) for the Baltic Sea according to

$$\frac{\mathrm{d}H}{\mathrm{d}t} = (F_\mathrm{i} - F_\mathrm{o} - F_\mathrm{loss})A_\mathrm{s}, \tag{4}$$

where $H = \int\int \rho c_\mathrm{p} T \, \mathrm{d}z \, \mathrm{d}A$ is the total heat content of the Baltic Sea, F_i and F_o are the heat fluxes associated with inflows and outflows, and F_loss is the total heat loss to the atmosphere (note that the fluxes are positive when going from the water to the atmosphere). F_loss reads

$$F_\mathrm{loss} = (1 - A_\mathrm{i})\left(F_\mathrm{n} + F_\mathrm{s}^\mathrm{o}\right) + A_\mathrm{i}\left(F_\mathrm{w}^\mathrm{i} + F_\mathrm{s}^\mathrm{i}\right) - F_\mathrm{ice} + F_\mathrm{r} + F_\mathrm{g} \tag{5}$$

where

$$F_\mathrm{n} = F_\mathrm{h} + F_\mathrm{e} + F_\mathrm{l} + F_\mathrm{prec} + F_\mathrm{snow}. \tag{6}$$

Table 3. Estimated annual mean heat fluxes for the Baltic Sea (order of magnitude). The fluxes are denoted as net heat flux (F_n), sun radiation to the open water surface (F_s^o), heat flow from water to ice (F_w^i), sun radiation through ice (F_s^i), the heat fluxes associated with precipitation in the form of rain (F_{prec}) and snow (F_{snow}), the heat sink associated with ice advection from the Baltic Sea (F_{ice}), heat flows associated with river runoff and ground-water flow F_r and F_g, the heat fluxes associated with inflows (F_i) and outflows (F_o), and the total heat loss to the atmosphere (F_{loss}). The fluxes are positive when going from the water to the atmosphere

F_n (W m^{-2})	F_s^o (W m^{-2})	F_w^i (W m^{-2})	F_s^i (W m^{-2})	F_{prec} (W m^{-2})	F_{snow} (W m^{-2})	F_{ice} (W m^{-2})	F_r (W m^{-2})	F_g (W m^{-2})	$F_o - F_i$ (W m^{-2})	F_{loss} (W m^{-2})
10^2	-10^2	10^0	-10^{-1}	10^{-1}	10^{-1}	-10^{-1}	10^{-1}	10^{-1}	10^{-1}	-10^0

Table 4. Mean heat balance of the Baltic Sea (the Belt Sea and the Kattegat excluded). The fluxes are positive when going from the water to the atmosphere. The fluxes are denoted as sensible heat (F_h), latent heat (F_e), net long-wave radiation (F_l), sun radiation to the open water surface (F_s^o), sun radiation through ice (F_s^i), heat flow from water to ice (F_w^i), and net heat loss $F_{loss} = (1 - A_i)(F_h + F_e + F_l + F_s^o) + A_i(F_s^i + F_w^i)$, where A_i is the ice concentration

Author	F_h (W m^{-2})	F_e (W m^{-2})	F_l (W m^{-2})	F_s^o (W m^{-2})	F_w^i (W m^{-2})	F_s^i (W m^{-2})	F_{loss} (W m^{-2})	Period
Present	10	37	37	−88	3	−0	−0	BALTEX/*BRIDGE* 2000–2002
Present	9	35	36	−85	4	−0	−1	1970–2002

The various terms in eqs. (5) and (6) are denoted as follows. A_i is ice concentration, F_h is the sensible heat flux, F_e is the latent heat flux, F_l is the net long-wave radiation, F_{prec} and F_{snow} are the heat fluxes associated with precipitation in the form of rain and snow, respectively, F_s^o is the short-wave radiation to the open water surface, F_w^i is the water flux to the ice, F_s^i is sun radiation through the ice, F_{ice} is the heat sink associated with ice advection out from the Baltic Sea, and F_r and F_g are heat flows associated with river runoff and ground-water flow, respectively. The orders of magnitude of the different terms are given in Table 3; F_{prec}, F_{snow}, F_{ice}, F_r and F_g are neglected in the present analysis.

The calculated long-term means of the various components of the heat balance appear in Table 4, while the annual means appear in Fig. 9 and the monthly means of the major heat balance components are given in Appendix A. The estimated net heat loss during the BALTEX/*BRIDGE* period was zero, while for the whole period it was -1 W m^{-2}. This is in good accordance with earlier results (Omstedt and Rutgersson, 2000; Meier and Döscher, 2002), and is important as it illustrates that the Baltic Sea is almost in local balance with the atmosphere over long time-scales. The inter-annual variations in net heat loss, Fig. 9d, indicate an inter-annual variability of ± 10 W m^{-2}.

The largest inter-annual variability was found in short-wave radiation, which ranged between -74.1 and -93.3 W m^{-2}. The inter-annual variabilities of the sensible (F_h), the latent (F_e) heat flux, the net long-wave radiation (F_l) and the heat flux from water to ice (F_w^i) were in the range of ± 5, ± 8, ± 8 and ± 3 W m^{-2}, respectively. It is interesting to note that the inter-annual variation in net heat loss was largest during the BALTEX/*BRIDGE* period.

Trends in some of the major heat balance components are illustrated in Fig. 10. The increase in net heat flux ($F_n = F_h + F_e + F_l$) to the open water surface balances the increase in sun radiation (F_s^o). The net Baltic Sea heat loss (F_{loss}) indicates no trend. This is also indicated in the observed Baltic Sea mean temperature, Fig. 5, where no trend can be noticed. The study thus shows that even if we have had an increasing air temperature of about 1°C during the studied 30-yr period, we cannot notice any changes in the annual Baltic Sea mean temperature. The result indicates that the Baltic Sea climate is influenced by negative feedback mechanisms that stabilize trends in the annual mean air temperature.

6. Comparison between ocean and atmospheric calculated heat fluxes

The scientific objectives in BALTEX include the determination of the water and energy cycles in the Baltic Sea region by combined data and modelling exercises, and the development of coupled, high-resolution forecasting systems for a better handling of the complex weather and climate processes. It is well known today that the weather forecasting of precipitation (and evaporation) provides the largest problems in weather predictions. This is also true for meteorological reanalysis such as the NCEP/NCAR data (Ruprecht and Kahl, 2003).

During the BALTEX/*BRIDGE* period, the coupled HIRLAM–BALTEX system was run for 1 yr (September 1999 to the end of October 2000) in a delayed data assimilation mode (Fortelius et al., 2002). The coupled model system was claimed to simulate the essential features of the water and energy cycles. To examine

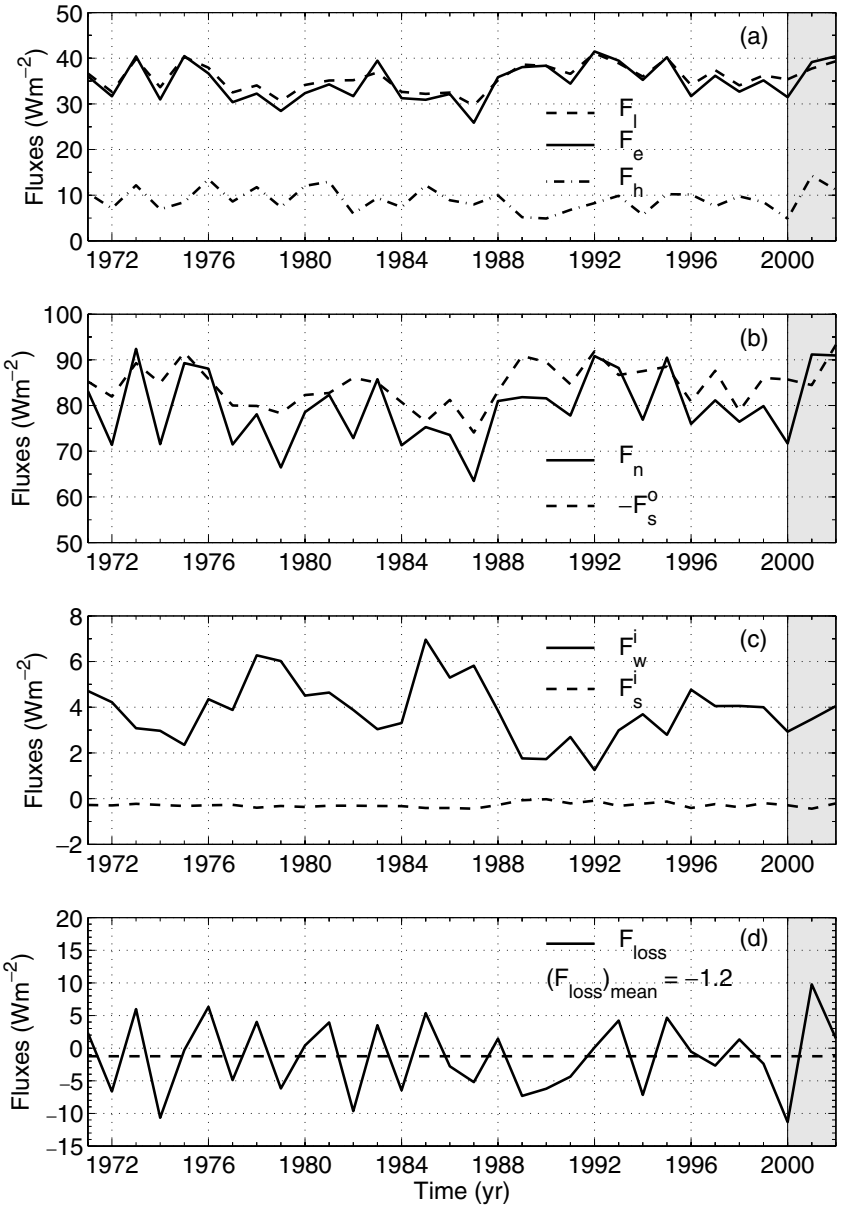

Fig 9. Annual means of sensible heat (F_h), latent heat (F_e), net long-wave radiation (F_l), net heat flux ($F_n = F_h + F_e + F_l$), sun radiation to the open water surface (F_s^o), sun radiation through ice (F_s^i), heat flow from water to ice (F_w^i), and net Baltic Sea heat loss $F_{loss} = (1 - A_i)\,(F_s^o + F_h + F_e + F_l) + A_i(F_s^i + F_w^i)$, where A_i is the ice concentration.

Table 5. A comparison between fluxes calculated by the PROBE-Baltic model and the HIRLAM–BALTEX model. For details of the nomenclature, see Table 4

Author	F_h (W m^{-2})	F_e (W m^{-2})	F_l (W m^{-2})	F_s^o (W m^{-2})	F_{loss} (W m^{-2})	Period
Fortelius (private communication)	7	44	54	−123	−18	1999–2000
Present	7	38	38	−88	−5	1999–2000

the output from the HIRLAM–BALTEX system, we analyse the heat balance in some more detail and particularly the closure of the Baltic Sea heat balance.

The calculated monthly mean heat fluxes from the HIRLAM–BALTEX system appear in Table 5 and Fig. 11 and are compared with those obtained in the present study. The estimated sensible heat fluxes show good agreement, but the latent heat fluxes estimated using the HIRLAM–BALTEX system are slightly higher than those estimated with PROBE-Baltic system. The main differences are found in the net long-wave and short-wave radiation, where the HIRLAM–BALTEX system calculates unrealistically large net fluxes.

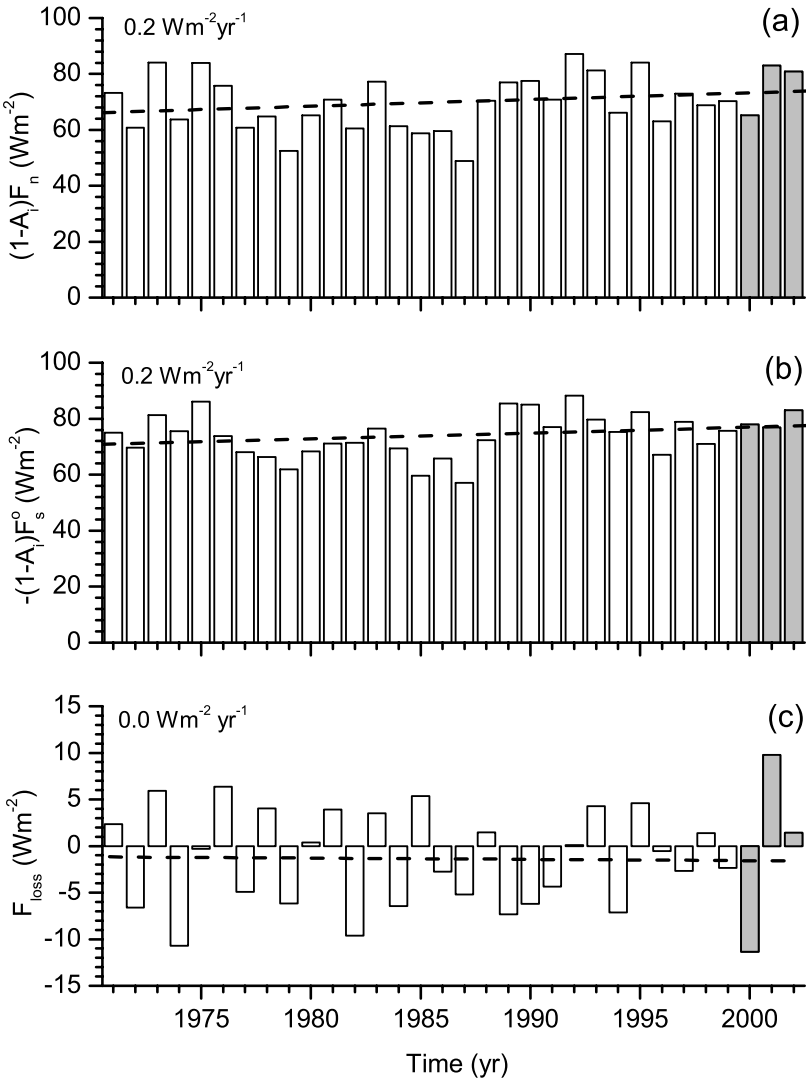

Fig 10. Annual means of some major heat fluxes: net heat flux ($F_n = F_h + F_e + F_l$), sun radiation to the open water surface ($-F_s^o$), and net Baltic Sea heat loss $F_{loss} = (1 - A_i)(F_s^o + F_h + F_e + F_l) + A_i(F_s^i + F_w^i)$, where A_i is the ice concentration. The dashed lines indicate the linear trends and the BALTEX/*BRIDGE* period is marked.

From the net heat loss we conclude that HIRLAM–BALTEX system gives an unrealistically high net input. This is probably because the HIRLAM–BALTEX system underestimates the cloud cover over the Baltic Sea (Fortelius, private communication), producing too high values for both short-wave and long-wave radiation.

7. Summary and conclusions

The main BALTEX experiment (*BRIDGE*) was the central element in the BALTEX (Baltic Sea Experiment) Phase I programme, with the aim of improving our understanding of water and energy cycle in the climate system. This work has examined the Baltic Sea water and heat balances for the *BRIDGE* period (2000–2002) in relation to current climatic conditions (1970–2002). The study follows on from earlier work in which Baltic Sea modelling is used as a tool for synthesizing available data. The modelling approach was validated with independent data sets of observations from salinity, temperature and ice extent. Data assimilation methods have therefore not been introduced in the modelling efforts.

The basic questions raised in the paper were as follows. (1) What are the values of the individual terms of the water and heat balances during the BALTEX/*BRIDGE* period and how do they vary over time? (2) How accurately can these balances be calculated? (3) Can detection of climate change signals be carried out more easily for the water and heat-cycle components compared to standard parameters such as temperature?

The values of the individual terms are illustrated in the figures and given as table values. Monthly mean values for the different terms during the BALTEX/*BRIDGE* period are also given in Appendix A. The calculated values show large seasonal and inter-annual variations in most components and do not reveal any strong climate change trends, except that net precipitation over the Baltic Sea was negative in 2002. This year stands out from the rest of the study period, when net precipitation was

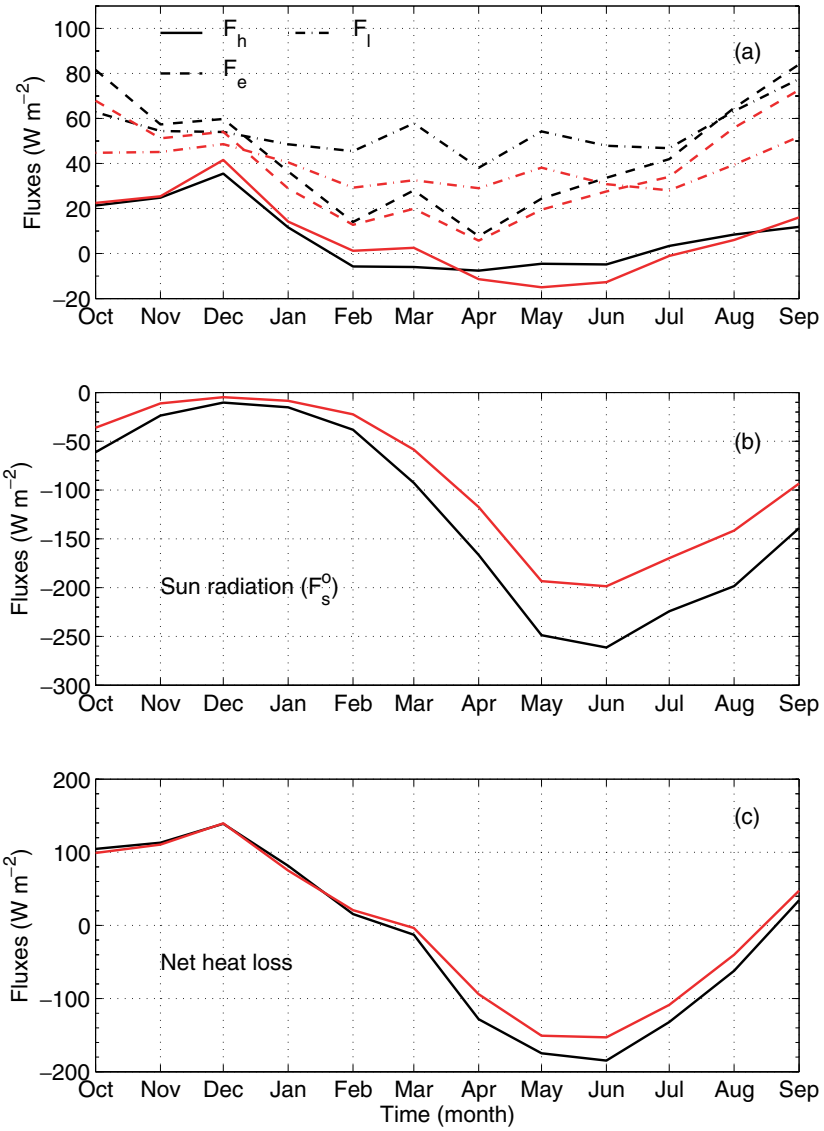

Fig 11. Comparison between flux calculations from the HIRLAM–BALTEX (black) and the PROBE-Baltic (red) model systems. For nomenclature, see caption to Fig. 9.

positive. Also, the inter-annual variability of net heat flux between the atmosphere and the Baltic Sea showed large variations during the *BRIDGE* period.

The errors in the water balance were investigated by comparing calculated and, from observations, estimated mean salinities of the Baltic Sea. The results imply that the mean error in the net water balance is much less than the river runoff (4% of the river runoff). This indicates that the net freshwater balance averaged over decades is quite accurate. The rms error is 10 times as large as the mean error, which implies that water balance studies on time-scales shorter than a decade could have large errors. The corresponding mean and rms errors in the net heat flux, determined by comparing calculated and observed mean temperatures of the Baltic Sea, were estimated as 2 and 3 W m^{-2}, respectively.

Detection of climate change signals can be found in different time series. Here we have examined both time series of mean meteorological conditions over the Baltic Sea and the corresponding calculated water and heat balances. The water and heat balances involve many different processes that may cause positive or negative feedback mechanisms. Despite observed atmospheric warming over the Baltic Sea during the 30-yr study period, no trends were observed in the annual mean water temperature or the net heat loss. The reason was that the increased net heat flux from the open water surface was balanced by an increase in sun radiation. Detection of climate change signals was not easier to observe in the water and heat balance studies, but these studies provide another item of information that can explain more about how the climate system responds to changes in forcing. Water and heat balance studies should therefore be used together with trend analysis on observed time series as tools in climate change studies.

The conclusions from the paper can be summarized as follows.

(i) Current Baltic Sea modelling and the meteorological and hydrological data available from the BALTEX data centres indicate that the net water balance and the net heat flux can be

estimated with good accuracy (mean errors over decadal timescales being about 600 $m^3\ s^{-1}$ and 2 $W\ m^{-2}$ respectively). The accuracy of the individual terms is still unknown.

(ii) Negative net precipitation was calculated for 2002; this year stands out from the rest of the 30-yr period when annual mean net precipitation rates were always positive. The calculated inter-annual variability of the net heat loss between atmosphere and Baltic Sea during the BALTEX/*BRIDGE* period indicated large variations ($\pm 10\ W\ m^{-2}$).

(iii) The Baltic Sea annual mean temperature has not increased during the study period despite an atmospheric warming of 1 °C. The reason was explained by the heat balance that indicated no trend in the Baltic Sea net heat loss.

8. Acknowledgments

This work is part of the GEWEX/BALTEX programme and has been funded by Göteborg University and the Swedish Research Council under the G 600-335/2001 contract. We would like to thank Carl Fortelius for making the HIRLAM–BALTEX data available. The data support from the BALTEX Hydrological Data (Bengt Carlsson) and Ocean Data Centres (Bertil Håkansson and Phillip Axe) and from SMHI (Barry Broman) are also acknowledged. The annual maximum ice extent values were made available by the Finnish Institute of Marine Research (Ari Seinä). Phil Graham at the SMHI-Rossby Centre made calculated river runoff data available. We would also like to thank the reviewer for constructive comments.

Finally we would like to thank all the enthusiastic scientists who have made BALTEX and Baltic Sea basic research possible.

9. Appendix A: Calculated major components in the water and heat balances during the BALTEX/*BRIDGE* period

Table A1. Monthly mean water balance for the Baltic Sea (the Belt Sea and the Kattegat excluded). The flows are denoted as: difference between outflows and inflows ($Q_o - Q_i$), river runoff (Q_r), net precipitation ($P - E$), storage change, and A_s the Baltic Sea surface area

Year	Month	$Q_o - Q_i$ ($10^3\ m^3\ s^{-1}$)	Q_r ($10^3\ m^3\ s^{-1}$)	$A_s\ (P - E)$ ($10^3\ m^3\ s^{-1}$)	Storage change ($10^3\ m^3\ s^{-1}$)
1999	10	9.98	10.59	−2.02	−1.41
1999	11	1.53	10.37	−4.96	3.88
1999	12	10.31	10.65	0.29	0.63
2000	1	4.67	10.87	−1.19	5.00
2000	2	24.27	12.48	2.49	−9.30
2000	3	40.99	14.56	1.96	−24.47
2000	4	30.67	19.27	4.68	−6.73
2000	5	−0.57	21.24	1.99	23.80
2000	6	16.50	17.76	5.36	6.62
2000	7	26.25	18.54	8.23	0.52
2000	8	21.66	17.78	−1.93	−5.81
2000	9	36.66	13.74	−8.05	−30.96
2000	10	−15.26	11.37	2.02	28.64
2000	11	26.68	14.47	5.79	−6.42
2000	12	2.22	14.44	0.52	12.74
2001	1	36.31	12.16	−0.45	−24.60
2001	2	4.91	12.01	−0.89	6.21
2001	3	38.54	12.60	0.42	−25.52
2001	4	3.91	17.48	6.31	19.87
2001	5	10.50	21.39	2.13	13.02
2001	6	23.94	16.91	5.89	−1.14
2001	7	8.30	15.26	1.43	8.39
2001	8	11.70	15.76	0.44	4.49
2001	9	37.04	16.56	3.44	−17.03
2001	10	−18.62	14.98	−1.40	32.19
2001	11	17.59	14.11	−6.88	−10.36
2001	12	5.54	11.82	−6.19	0.09
2002	1	−9.57	12.16	4.03	25.76
2002	2	16.89	12.01	5.94	1.06
2002	3	59.75	12.60	2.33	−44.82

Table A2. Monthly mean heat balance of the Baltic Sea (the Belt Sea and the Kattegat excluded). The fluxes are positive when going from the water to the atmosphere. The fluxes are denoted as: sensible heat (F_h), latent heat (F_e), net long-wave radiation (F_l), sun radiation to the open water surface (F_s^o), heat flow from water to ice (F_w^i), net heat loss (F_{loss}), and A_i the calculated Baltic Sea monthly mean ice coverage

Year	Month	F_h (W m^{-2})	F_e (W m^{-2})	F_l (W m^{-2})	F_s^o (W m^{-2})	F_w^i (W m^{-2})	F_{loss} (W m^{-2})	A_i
1999	10	23	70	45	−34	0	104	0
1999	11	26	54	45	−10	0	115	0
1999	12	48	61	51	−4	0	157	0
2000	1	20	36	42	−8	6	97	0.14
2000	2	5	17	32	−22	10	41	0.29
2000	3	5	23	33	−56	9	13	0.30
2000	4	−11	5	28	−112	7	−83	0.17
2000	5	−17	14	36	−189	0	−155	0
2000	6	−18	17	29	−200	0	−170	0
2000	7	−5	25	26	−170	0	−124	0
2000	8	4	50	39	−141	0	−49	0
2000	9	15	73	55	−94	0	49	0
2000	10	10	43	35	−34	0	54	0
2000	11	19	39	32	−9	0	80	0
2000	12	32	43	44	−4	0	115	0
2001	1	31	41	42	−7	0	107	0
2001	2	39	41	45	−24	15	116	0.22
2001	3	9	19	31	−49	11	20	0.38
2001	4	−8	6	26	−100	10	−67	0.18
2001	5	−17	12	37	−190	0	−158	0
2001	6	−16	11	29	−197	0	−173	0
2001	7	−6	38	35	−201	0	−134	0
2001	8	4	56	39	−143	0	−45	0
2001	9	16	62	37	−75	0	40	0
2001	10	13	45	37	−34	0	62	0
2001	11	41	82	53	−11	0	165	0
2001	12	65	65	53	−4	1	180	0.02
2002	1	18	25	29	−6	10	75	0.27
2002	2	5	20	30	−22	9	42	0.28
2002	3	1	17	33	−59	7	−1	0.27

References

Alexandersson, H., Tuomenvirta, H., Schmith, T. and Iden, K. 2000. Trends in storms in NW Europe derived from an updated pressure data set. *Climate Res*. **14**, 71–73.

BALTEX 1995. Baltic Sea Experiment BALTEX. Initial Implementation Plan. International BALTEX Secr. Publ. Series, ISSN 1681-6471, No. 2. International BALTEX Secretariat. GKSS Geestacht, Germany, 84 pp.

BALTEX 1997. The Main BALTEX Experiment 1999–2001—*BRIDGE*. Strategic Plan. International BALTEX Secr. Publ. Series, ISSN 1681-6471, No. 9. International BALTEX Secretariat. GKSS Geestacht, Germany, 78 pp.

Bengtsson, L. 2001. Numerical modelling of the energy and water cycle of the Baltic Sea. *Meteorol. Atmos. Phys*. **77**, 9–17.

Fortelius, C., Andræ, U. and Forsblom, M. 2002. The BALTEX regional reanalysis project. *Bor. Env. Res*. **7**, 193–201.

Gustafsson, N., Nyberg, L. and Omstedt, A. 1998. Coupling of a high-resolution atmospheric model and an ocean model for the Baltic Sea. *Mon. Wea. Rev.* **126**, 2882–2846.

Hennemuth, B., Rutgersson, A., Bumke, K., Clemens, M., Omstedt, A. et al. 2003. Net precipitation over the Baltic Sea for one year using models and data-based methods. *Tellus* **55A**, 352–367.

Jacob, D. 2001. A note to the simulation of annual and inter-annual variability of the water budget over the Baltic Sea drainage basin. *Meteorol. Atmos. Phys*. **77**, 61–73.

Källén, E. 1996. HIRLAM documentation manual, System 2.5. Technical report, HIRLAM project SMHI, SE-601 76 Norrköping, Sweden.

Lehmann, A. and Hinrichsen, H.-H. 2001. The importance of water storage variations for water balance studies of the Baltic Sea. *Phys. Chem. Earth (B)*, **26 (5-6)**, 383–389.

Lehmann, A. and Hinrichsen, H.-H. 2002. Water exchange between the deep basins of the Baltic Sea. *Bor. Env. Res*. **7**, 405–415.

Meier, M. and Döscher, R. 2002. Simulated water and heat cycles of the Baltic Sea using a 3D coupled atmosphere–ice–ocean model. *Bor. Env. Res.* **7**, 327–334.

Omstedt, A. and Axell, L. 2003. Modeling the variations of salinity and temperature in the large Gulfs of the Baltic Sea. *Continental Shelf Research* **23**, 265–294.

Omstedt, A. and Rutgersson, A. 2000. Closing the water and heat cycles of the Baltic Sea. *Meteorol. Z.* **9**, 57–64.

Omstedt, A., Meuller, L. and Nyberg, L. 1997. Inter-annual, seasonal and regional variations of precipitation and evaporation over the Baltic Sea. *Ambio* **26** (8), 484–492.

Omstedt, A., Gustafsson, B., Rodhe, J. and Walin, G. 2000. Use of Baltic Sea modelling to investigate the water and heat cycles in GCM and regional climate models. *Clim. Res.* **15**, 95–108.

Omstedt, A., Pettersen, C., Rodhe, J. and Winsor, P. 2004. Baltic Sea climate: 200 yr of data on air temperature, sea level variation, ice cover, and atmospheric circulation. *Clim. Res.* **25**, 205–216.

Orviku, K., Jaagus, J., Kont, A., Ratas, U. and Rivis, R. 2003. Increasing activity of coastal processes associated with climate change in Estonia. *J. Coastal Res.* **19**(2), 364–375.

Peltonen, K. 2002. Direct ground-water inflow to the Baltic Sea. *TemaNord, 503*. Nordic Council of Ministers, Copenhagen, Denmark.

Piechura, J. and Beszczynska-Möller, A. 2003. Inflow waters in the deep regions of the southern Baltic Sea: transport and transformations. *Oceanologia* **45**(4), 593–621.

Pryor, S. C. and Barthelmie, R. J. 2003. Long-term trends in near-surface flow over the Baltic. *Int. J. Climatol.* **23**, 271–289.

Raschke, E., Meywerk, J., Warrach, K., Andrea, U., Bergström, S. et al. 2001. BALTEX (Baltic Sea Experiment): A European contribution to investigate the energy and water cycle over a large drainage basin. *Bull. Am. Meteorol. Soc.* **82**(11), 2389–2413.

Ruprecht, E. and Kahl, T. 2003. Investigation of the atmospheric water budget of the BALTEX area using NCEP/NCAR reanalysis data. *Tellus* **55A**, 426–437.

Rutgersson, A., Omstedt, A. and Räisänen, J. 2002. Net precipitation over the Baltic Sea during present and future climate conditions. *Climate Res.* **22**, 27–39.

Stigebrandt, A, 2001. Physical Oceanography of the Baltic Sea, Ch. 2. In: *A Systems Analysis of the Baltic Sea* (eds F. Wulff, L. Rahm and P. Larsson). Springer-Verlag, Berlin.

Winsor, P., Rodhe, J. and Omstedt, A. 2001. Baltic Sea ocean climate: an analysis of 100 yr of hydrographic data with focus on the freshwater budget. *Climate Res.* **18**, 5–15.

Winsor, P., Rodhe, J. and Omstedt, A. 2003. Erratum: Baltic Sea ocean climate: an analysis of 100 yr of hydrographic data with focus on the freshwater budget. *Climate Res.* **25**, 183.

Paper II

,

Computation of energy for diapycnal mixing in the Baltic Sea due to internal wave drag acting on wind-driven barotropic currents

Christian Nohr[*,a], Bo G. Gustafsson[b]

[a] *Department of Oceanography, Earth Science Center, University of Gothenburg, Box 460, SE-405 30 Göteborg, Sweden*
[b] *Baltic Nest Institute - Stockholm Resilience Center, Stockholm University, SE-106 91 Stockholm, Sweden*

Abstract

The pathways of energy supply for mixing the deep waters of the Baltic Sea is largely unknown. In this paper, a parameterization of the internal wave drag forces on barotropic motion is developed and implemented into a two-dimensional shallow water model of the Baltic Sea. The model is validated against observed sea levels. The dissipation of barotropic motion by internal wave drag that is quantified from the model results shows that breaking internal waves generated by wind forced barotropic motions can contribute significantly to the diapycnal mixing in the deep water of the Baltic Sea.

Key words: Baltic Sea, Turbulent mixing, Internal waves

1. Introduction

The Baltic Sea is a huge fjord-like estuary with a strong permanent haline stratification and long deep-water residence times (Stigebrandt, 2001, 2003; Meier, 2005). A substantial freshwater surplus in combination with limited ocean exchange makes the Baltic permanently salt stratified. In the main basin, the Baltic proper, the halocline is located at a depth of approximately 60 m, and below 125-150 m the water is only exchanged intermittently. A seasonal thermocline is formed at 15-20 m during summer and also during winter if temperature decrease below that of maximum density (see Fig. 2).

A restricted water exchange with the North Sea in combination with a large surface area efficiently filters external high frequency sea level oscillations and therefore the contribution of tides to sea level variability is insignificant (Stigebrandt, 1980a; Samuelsson and Stigebrandt, 1996; Gustafsson and Andersson, 2001). Thus, tides as a source of energy for diapycnal mixing is excluded in the Baltic Sea. Still, estimates reveal that the energy supply to perform observed changes in stratification is of the order of 2.1 mW m^{-2} (Liljebladh and Stigebrandt, 2000), which is actually of similar order of magnitude as observed in smaller fjord basins on the Norwegian coast that are subject to strong tidal currents (Stigebrandt and Aure, 1989).

[*] Corresponding author.
Email addresses: chno@oce.gu.se (Christian Nohr), bo.gustafsson@stockholmresilience.su.se (Bo G. Gustafsson)

A number of processes can contribute to diapycnal mixing in the Baltic Sea. Vertically propagating near-inertial waves driven by variability in the wind field was thought to be of major importance until Liljebladh and Stigebrandt (2000) managed to quantify its contribution to about 0.35 mW m^{-2}. Observations of strong baroclinic eddies in the deep water lead to the speculation that these might give a substantial contribution to diapycnal mixing (cf. Meier et al., 2006; Stigebrandt et al., 2002, and references in these). This speculation was challenged by Svensson (2005) who estimated from observations that mesoscale eddies do not contribute significantly to diapycnal mixing. Double-diffusive mixing may occur periodically when intrusions of warm and salty waters are interleaved in the stratification (e.g. Kuzmina et al., 2005), but in general this should not be a factor either for the overall mixing since the absolute majority of deep water is quite strongly salt stratified. Coastal dynamics may enhance mixing due to up- and downwelling, which is exemplified in Stigebrandt et al. (2002). Döös et al. (2004) estimated a dissipation rate of 0.4 - 1.2 mW m^{-2} by turbulent bottom friction from simulations with a barotropic numerical model. A portion of these losses could possibly be used for mixing. Axell (1998) estimated from observations of stratification that the needed energy supply for mixing in the deeper deep waters (depth > 150 m) was about 5 and 0.6 mW m^{-2} in the Landsort deep and Eastern Gotland Basin, respectively. He found a strong seasonal cycle that largely follows that of the wind. However, there are still gaps in our understanding on how energy is transferred from the atmosphere to the turbulent mixing in the deep.

Although conversion of barotropic to baroclinic waves has been under intense focus during the past decade, there are no conclusive ways to quantify the energy flux. The part of the problem that involves the excitation of internal waves at (idealized) topography and given stratification is fairly straightforward, but it becomes virtually impossible to solve for a realistic topography and including processes like wave-wave interaction and non-linear dissipation due to breaking waves. The importance of small-scale processes is evident from studies of internal tides in fjord basins. For example, Berntsen et al. (2008) demonstrated sub-grid scale closure and resolution dependence in very high resolution (10 - 100 m) simulations of internal tides with a non-hydrostatic model and Johnsson et al. (2007) showed experimentally that two very closely spaced sills (about 1 km or 1/7 of the internal Rossby radius) generated internal tides without interaction. Thus, one has to reside on various extremely simplified parameterizations. In recent quantifications of internal wave drag on barotropic tides using shallow water models, parameterizations based on simple analytical considerations and scale arguments have been used (e.g. Sjöberg and Stigebrandt, 1992; Gustafsson, 2001; Jayne and St Laurent, 2001; Egbert et al., 2004; Nycander, 2005; Tanaka et al., 2007). There are also examples of direct numerical simulations of generation of internal tides using three-dimensional models (e.g. Niwa and Hibiya, 2001; Merrifield and Holloway, 2002; Simmons et al., 2004, and several others).

In this paper, we investigate to what extent energy can be transferred from the atmosphere via barotropic motion to turbulent kinetic energy in the deep. One possibility is that internal waves are generated at steep topography, as it does for tides in the deep oceans and in sill fjords, and another is that turbulence is generated in the bottom boundary layer. We use a 2-dimensional shallow water model forced by observed winds and air pressure fields to estimate the energy loss from the barotropic motion due to internal wave drag and bottom friction. The parameterization of wave drag follows the so-called step model (Stigebrandt, 1976, 1980b; Sjöberg and Stigebrandt, 1992; Stigebrandt, 1999; Gustafsson, 2001; Johnsson et al., 2007). Opposing the oceanic applications of Sjöberg and Stigebrandt (1992) and Gustafsson (2001), we expect a dominant influence of the first baroclinic mode and therefore we must consider the stratification of the whole water column. A generalization of internal wave drag on barotropic currents for arbitrary

stratification given by Stacey (1984) is adapted to give drag force in a two-dimensional shallow water model. The validity of the step model was recently challenged by St. Laurent et al. (2003), primary concerns are the assumption of local non-interacting wave generation at each step and that a resolution dependence was found that the internal wave generation approach zero as resolution is increased. We will discuss this further in the discussion section in light of present results, however, noteworthy are the experiences from Egbert et al. (2004) that the step model gives similar internal wave drag as some other parameterizations.

This paper is outlined as follows, the model and the implementation of the model is described in Section 2, the performance of the model is evaluated by comparison with observed sea levels in Section 3. In Section 4 we present the results from the simulations and the paper ends with a discussion on the results and their implications.

2. Method

2.1. Model description

The model is based on the two-dimensional shallow water equations, hence, density variations, non-linear interaction in vertical shear flow and non-hydrostatic pressure are all disregarded. This results, of coarse, in severe limitations on the realism of the results for a basin that is strongly stratified. However, the aim here is not to realistically simulate the vertical current structure, but to make an order of magnitude estimate of the possible energy conversion from atmospherically forced barotropic motion to internal motion and for this purpose the shallow water approximations will most probably suffice. A more severe limitation of the shallow water equations in the present context is that parameterization of drag from bottom boundary layers becomes rather dubious since the actual bottom near currents might not be related to the barotropic flow.

The numerical scheme follows closely the classic model by Arakawa and Lamb (1981). The following form of the momentum equations are discretized,

$$\frac{\partial \mathbf{v}}{\partial t} + q\mathbf{k} \times \mathbf{v}^* + \nabla (K + \Phi) = \frac{\mathbf{F}}{h} \tag{1}$$

where h is height of the water column, $\mathbf{v}$ is the velocity vector, $\mathbf{v}^* = \mathbf{v}h$ is the flow vector and $K = \mathbf{v}^2/2$ is the specific kinetic energy . The potential vorticity q is defined as

$$q = \frac{\zeta + f}{h} \tag{2}$$

where ζ is the vorticity and f is the Coriolis parameter that in this case is considered as constant ($F = 1.2 \times 10^{-4}$ s^{-1}). The pressure Φ is given by

$$\Phi = g(h - D) + \frac{P_a}{\rho_0} \tag{3}$$

where $g = 9.8$ m s^{-1} is acceleration of gravity, D is the equilibrium water depth, P_a is the atmospheric pressure and $\rho_0 = 1010$ kg m^{-3} is a reference density of sea water. The body force $\mathbf{F}$ comprises of three parts: the wind force $\mathbf{F}_{wind}$, bottom drag force $\mathbf{F}_b$ and internal wave drag force $\mathbf{F}_w$.

The sea surface height is determined from the continuity equation

$$\frac{\partial h}{\partial t} + \nabla \cdot \mathbf{v}^* = 0 \tag{4}$$

The spatial discretization is done on a uniform C-grid and following the Arakawa-Lamb scheme (Arakawa and Lamb, 1981) that ensures energy and entropy conservation. The Arakawa-Lamb scheme requires a computational boundary condition on the tangential velocity at solid boundary and for this we used a free-slip condition. The temporal evolution is computed with a third-order Runge-Kutta solver following Williamson (1980). Body forces are applied explicitly.

Experimentally the drag force due small scale flow separation and bed friction can be estimated from the current velocity squared at a fixed height above the sea bed and a drag coefficient that depends on the structure of the sea bed (e.g. Dyer, 1986; Soulsby, 1997). The first order approximation is to use this parameterization for the drag loss to the turbulent bottom boundary layer $\mathbf{F}_b$ of the barotropic currents as well,

$$\mathbf{F}_b = -C_d \, |\mathbf{v}| \, \mathbf{v} \tag{5}$$

where C_d is a dimensionless drag coefficient. There are frequent examples of usage of the quadratic drag law in ocean tidal models (e.g. Egbert et al., 2004; Arbic et al., 2004; Tanaka et al., 2007; Weis et al., 2008). In a classic variant of Eq. 5 commonly used in shelf seas applications, the drag coefficient is a more or less weak function of depth through introduction of a depth-dependent Chezy coefficient or Manning number (e.g. Soulsby, 1997; Umgiesser, 1997; Verboom et al., 1992; Jakobsen et al., 2002). We use Eq. 5 with constant drag coefficient, however we will investigate the sensitivity of the results to varying values on the coefficient.

2.2. Derivation of the internal wave drag force

The basic assumption for the derivation of the wave drag parameterization is that the depth changes abruptly from one grid cell to another, thus forming a step, and that velocity must be zero at the vertical wall defined by the step. Internal waves are added to satisfy this boundary condition. The step-model was originally proposed for sill fjords where the sill itself constitutes the step (Stigebrandt, 1976, 1980b), but was generalized to a discrete two-dimensional grid of sea floor by Sjöberg and Stigebrandt (1992). Stacey (1984) generalized the model by Stigebrandt (1976, 1980b) to arbitrary continuous stratification. We use the work of Stacey (1984) to formulate wave drag in the shallow water model.

We show the derivation of the internal wave drag parameterization in the x-direction, since the derivation of the drag in y-direction is be completely analogous. All effects of earth rotation on the internal waves are disregarded and the justification and consequences of this is discussed later in this paper, see section 5.

Consider two adjacent grid cells, one deeper with depth H_b and one shallower with depth d. The velocity in the deeper grid cell is given by a superposition of a barotropic wave defined by velocity amplitude u_0, frequency ω and wave number k_0, and an infinite number of internal wave modes $\hat{u}_n(z)$ of amplitudes a_n and wave numbers k_n.

$$\begin{aligned} u(x,z,t) &= u_0 cos(\omega t + k_0 x) + \\ &\quad \sum_{n=1}^{\infty} a_n \hat{u}_n(z) cos(\omega t + k_n x) \end{aligned} \tag{6}$$

We assume that no internal waves are generated in the shallower grid cell and therefore the velocity in the shallower grid cell is barotropic with amplitude, u_s. The boundary condition at the step ($x = 0$) becomes

$$u_0 + \sum_{n=1}^{\infty} a_n \hat{u}_n(z) = \begin{cases} u_s & 0 \geq z \geq -d \\ 0 & -d > z \geq -H_b \end{cases} \tag{7}$$

Since the internal wave modes, $\hat{u}_n$, are zero in mean and orthogonal, the amplitudes are given by

$$a_n = u_s \frac{\int_{-d}^{0} \hat{u}_n dz}{\int_{-H_b}^{0} \hat{u}_n^2 dz} \tag{8}$$

Horizontal and vertical modes are related via the continuity equation

$$\hat{u}_n = \frac{1}{k_n} \frac{d\hat{W}_n}{dz} \tag{9}$$

The vertical structure of the modes for arbitrary continuous stratification can be found by solving the following vertical velocity eigenvalue problem

$$\frac{d^2\hat{W}_n}{dz^2} + \frac{N^2}{c_n^2}\hat{W}_n = 0 \tag{10}$$

where $N^2 = -\frac{g}{\rho}\frac{d\rho}{dz}$ is the buoyancy frequency (squared) and c_n the wave speed of mode n. The boundary conditions are

$$\hat{W}_n(0) = \hat{W}_n(-H_b) = 0 \tag{11}$$

Thus, the horizontal velocity amplitudes (Eq. 8) can be calculated from Eqs. (9 and 10), and from the amplitudes the energy density of each the modes is straightforward,

$$E_n = \frac{\rho}{2} \frac{u_s^2 \hat{W}_n(-d)^2}{\int_{-H_b}^{0} \left[\frac{d\hat{W}_n}{dz}\right]^2 dz} \tag{12}$$

Note that the energy density does not depend on the normalization of $\hat{W}_n$ since any scale factor is eliminated. The energy flux radiating with internal waves (per unit width) away from the step is given by

$$\epsilon = \sum_{n=1}^{\infty} c_n E_n \tag{13}$$

where c_n is the group speed which is equal to the phase speed since we are only considering long waves. Dissipation from barotropic motion in the x-direction in the shallow water model, say ϵ_{SH}, is given by

$$\epsilon_{SH} = \rho u_i F_w^x \Delta s \tag{14}$$

where u_i is the velocity, F_w^x the drag force and Δs the grid spacing. Following the definition of the Arakawa C-grid, the velocity u_i is defined at the average depth of the two adjacent grid cells. By neglecting differences in sea surface elevation we can express the velocity in the shallower grid cell, u_s, in the model velocity u_i,

$$u_s d = u_i \frac{1}{2}(H_b + d) \tag{15}$$

By imposing that $\epsilon_{SH} = -\epsilon$ and substitute u_s with u_i we get the following expression on the wave drag in the x-direction

$$F_w^x = -\frac{u_i}{2\Delta s}\left(\frac{H_b + d}{2d}\right)^2 \sum_{n=1}^{\infty} c_n \frac{\hat{W}_n(-d)^2}{\int_{-H_b}^{0}\left[\frac{d\hat{W}_n}{dz}\right]^2 dz} \tag{16}$$

A baroclinic drag coefficient $r_w^x = \frac{F_w^x}{u_i}$ at grid point *i,j* can be defined as

$$r_w^x = -\frac{1}{2\Delta s}\left(\frac{H_b + d}{2d}\right)^2 \sum_{n=1}^{\infty} c_n \frac{\hat{W}_n(-d)^2}{\int_{-H_b}^{0}\left[\frac{d\hat{W}_n}{dz}\right]^2 dz} \tag{17}$$

where the depths are calculated from equilibrium depths of the adjacent grid cells, and $\hat{W}_n$ and c_n are computed for the deepest of the two cells.

A completely analogous expression is derived for baroclinic drag in the y-direction. To write the wave drag in vector notation we can define a matrix $\mathbf{R_w}$ that has the drag coefficients r_w^x and r_w^y, for x and y-directions, respectively, as diagonal elements, that is,

$$\mathbf{F_w} = \mathbf{R_w} \cdot \mathbf{v} \tag{18}$$

2.3. Derivation of an approximate drag force

In a strongly two-layer stratified basin, like the Baltic Sea, it may be possible to use a simplified form of the wave drag. It can easily be shown that the total energy density of the internal waves are independent of the stratification, see Sjöberg and Stigebrandt (1992). In our notation the total internal wave energy density becomes

$$E = \frac{\rho}{2} u_s^2 d\left(1 - \frac{d}{H_b}\right) \tag{19}$$

If we use Eq. 15 and define $H = \frac{1}{2}(H_b + d)$ and $\Delta H = \frac{1}{2}(H_b - d)$, the energy density can be written as

$$E = \rho u_i^2 \frac{1}{1 - \left(\frac{\Delta H}{H}\right)^2} \Delta H \tag{20}$$

If a the first mode dominates, one can estimate the energy flux of the internal waves by using the group speed of that mode, say c_g, and derive an expression for the wave drag by equality between energy flux of the internal waves and the dissipation in the barotropic model as in Section 2.2. The result is

$$F_w^x = -c_g \frac{1}{1 - \left(\frac{\Delta H}{H}\right)^2} \frac{\Delta H}{\Delta s} u_i \tag{21}$$

There are practical advantages if this can be used, since only an estimate of the first mode group speed is needed instead of continuous density profiles. For long waves the group speed can be approximated by

$$c_g = \sqrt{g\frac{\Delta\rho}{\rho}h_p\left(1-\frac{h_p}{H_b}\right)} \tag{22}$$

where h_p is the depth of the pycnocline and $\Delta\rho$ a typical difference between surface and deep water density. Naturally $c_g = 0$ if $h_p \geq H_b$.

2.4. Implementation

Three equidistant grids, 1x1 nm, 2x2 nm and 4x4 nm, were interpolated from a bathymetry with an original resolution of 2 minutes in longitude and 1 minute in latitude (Seifert et al., 2001). The 2x2 nm bathymetry (shown in Fig. 1) was used in all simulations, except those testing the sensitivity of the results to changed horizontal resolution. A sponge zone was added at the open boundary towards the North Sea by adding 20 identical points westwards (see Fig. 1). In this zone, velocity and surface elevation was relaxed towards the external boundary condition following the flow relaxation method devised by Martinsen and Engedahl (1987). The open boundary towards the North Sea is forced by hourly sea level observations from Hirtshals. We assume that the sea level gradually changes from the observed level at the coast with the length scale of the local Rossby radius. The velocity is specified according to Flather (1976). Thus, the equations for sea level and currents along the open boundary are

$$\frac{d\eta}{dy} = -\frac{f}{\sqrt{gD}}\eta \tag{23}$$

and

$$u = \sqrt{\frac{g}{D}}\eta \tag{24}$$

In the equation for sea level, η, y is directed along the open boundary, f is the Coriolis parameter, g is acceleration of gravity and D is the depth.

The model is forced by geostrophic wind and air pressure fields with a time resolution of 3 hours and a grid resolution of $1^\circ \times 1^\circ$. The database is available from the BALTEX Hydrological Data Center (BHDC), and it is here interpolated to fit the grid of the model domain. The wind stress is calculated from geostrophic wind in two steps. First, the geostrophic wind is reduced to 10-m wind using $\mathbf{w}_{10} = \mathbf{M} \cdot \mathbf{w}_g$. The reduction is found by comparing with wind observations in central Baltic proper. The conversion matrix that is used is

$$\mathbf{M} = \begin{bmatrix} 0.645 & 0.215 \\ 0.229 & 0.645 \end{bmatrix} \tag{25}$$

The wind force is calculated from

$$F_{wind} = \frac{\rho_a}{\rho_0}C_a|\mathbf{w}_{10}|\mathbf{w}_{10} \tag{26}$$

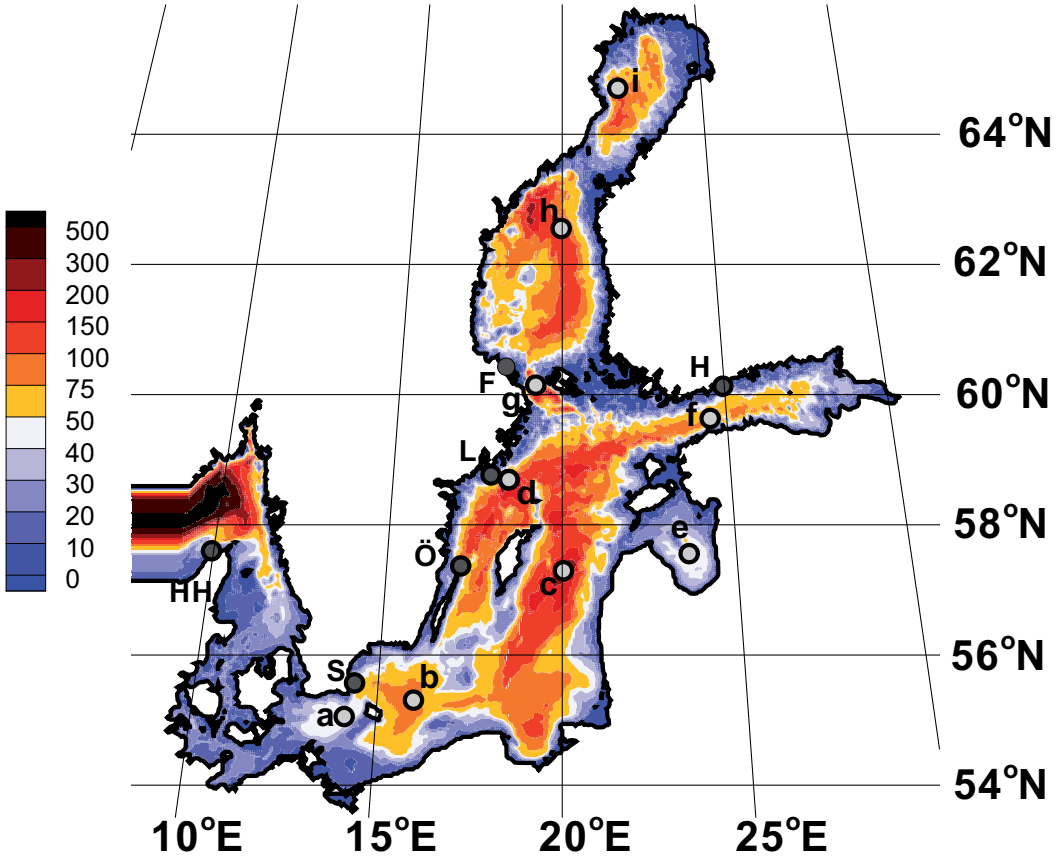

Figure 1: The 2x2 nm model bathymetry, including the added sponge zone at the border to the North Sea. The locations of mereographs used in this paper are indicated. The abbrevations are: HH=Hirtshals, S=Simrishamn, Ö=Ölands Norra Udde, L=Landsort, F=Forsmark and H=Helsinki. The hydrographic stations used for calculation of dynamic wave modes are indicated by light grey circles and the legend for the lower case letters is a=BY2, b=BY5, c=BY15, d=BY31, e=Gulf of Riga, f=LL11, g=F64, h=US5B and i=F9. The depths in the colour scale are given in meters.

where $\rho_a = 1.25$ kg m^{-3} is the density of air. The drag coefficient, C_a, is computed following Smith (1980), i.e.,

$$C_a = \begin{cases} 1.1 \times 10^{-3} & |\mathbf{w}_{10}| < 6m/s \\ (0.73 + 0.063|\mathbf{w}_{10}|) \times 10^{-3} & |\mathbf{w}_{10}| \geq 6m/s \end{cases} \quad (27)$$

The main simulation period was chosen to be 1992-01-01 - 1992-12-31, a year with no major deep-water inflows. This was also a warm year with only limited ice extent and therefore only limited effects of sea ice on the momentum fluxes at the sea surface are expected.

In our standard case we use a bottom drag coefficient $C_d = 3 \times 10^{-3}$. However, a series of simulations are performed varying the bottom drag coefficient (C_d), spatial resolution, wind stress and without wave drag. Also the simplified drag formula is tested.

2.5. Calculation of the baroclinic drag coefficient.

Observed density profiles from 9 oceanographic stations (locations shown in Fig. 1) are used to calculate the vertical dynamic modes $\hat{W}_n$ and the corresponding phase speeds c_n. The data from each station is assumed to be representative for a part of the Baltic Sea so that in all the 9 stations covers the model domain inside the sills. Fig. 2 shows typical winter and summer stratification in the three regions in the Baltic Sea, the Gotland Deep (BY15), the Landsort Deep (BY31) and the Åland Sea (F064). A characteristic summer thermocline is seen at about 20 m and a perennial pycnocline at about 60 m depth. Wave drag is not computed for the Skagerrak and Kattegat. The procedure for calculating the wave drag coefficients, $\mathbf{R_w}$, are as follows: The depths H_b and d are determined for each grid cell pair. The buoyancy frequency profile N is calculated either as a summer (mean for the month May-August) or a winter (mean for the month November-March) profile from the oceanographic station in the vicinity of the grid cell. Data from 1988-1992 were used to calculate summer and winter mean profiles. The vertical resolution was 5 m and linearly interpolated to 1 m resolution. The profiles are truncated at the depth of the deeper grid cell, i.e., at H_b. The vertical dynamic modes problem is solved using numerical integration techniques, in this case *Runge-Kutta* with the shooting method. The methods of *Runge-Kutta* uses a trial step to the midpoint of an interval to cancel out lower-order error terms. The shooting method is a method for solving a boundary value problem by reducing it to the solution of an initial value problem, the analysis is described in e.g. Press et al. (1997). The 10 first modes are calculated.

In the calculation with the approximate wave drag formula (Eq. 21), we used a constant $\Delta\rho = 3$ kg m^{-3} and $h_p = 65$ m throughout the Baltic Sea, although the figures are representative for the Baltic proper only.

3. Model performance

Model results are validated against hourly data from five sea level monitoring stations, Simrishamn, Landsort, Ölands Norra Udde, Helsinki and Forsmark (locations shown in Fig. 1. The stations are selected to cover the main parts of the Baltic proper. The time-series of simulated and observed sea levels for the whole simulation are drawn in Fig. 3. Since the model starts with zero sea level everywhere, there is a spin-up period of about 20 days before the volume of the Baltic is adjusted to the boundary conditions. The model captures most of the sea level variations, but generally underestimates the magnitude of short extreme sea level events. The high frequency variability is larger in the Bay of Bothnia and Gulf of Finland (Forsmark and Helsinki, Fig. 3a

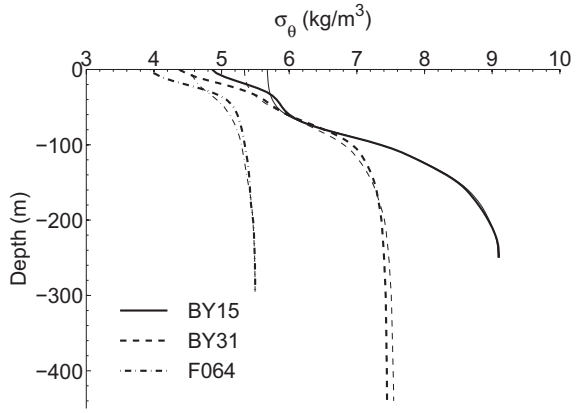

Figure 2: Examples of typically vertical winter and summer stratification from Gotland Deep (BY15), Landsort Deep (BY31) and Åland Sea (F064).

and 3b), and in the southern Baltic (Simrishamn, Fig. 3e) compared to the central Baltic (Landsort, Fig. 3c) due to wind set-up. There is a spurious deviation between model and observation at about 320-340 days at Forsmark that is difficult to explain as the model performs well at other locations during this time.

Power spectra of modeled and observed sea levels at the five sea level monitoring stations are shown in Fig. 4. The computation was done with a 256 hours long Hanning window with 50% overlap, which gave a total of 67 independent determinations. At all positions, semidiurnal tides (M_2 = 12.42 hour) are seen in both observations and simulated sea levels. There is a tendency for a diurnal tide in some of the sea level observations that do not show up in the model results as diurnal tidal signal is primarily locally driven and not imported from the North Sea. As indicated above in the time-series plots (Fig. 3), the model underestimates variance in the high frequency part of the spectrum. In relative terms, the performance at high frequencies are better at Forsmark and Simrishamn at Landsort and Ölands Norra Udde. The probable cause is that the variability close to the nodal line of oscillations is to a larger degree depending on small-scale features in forcing and topography than near the anti-nodes. The time resolution of the forcing prevents the model from capturing periods shorter than 3 hours. Sea level response above periods of 10 hours has energy comparable with observations and at some stations the model results show comparable energy levels to as low periods as 4 - 5 hours. In Figure 5, coherence and phase spectra are shown. Even though power density spectra indicate that the model produces significant amount of energy at relatively high frequency, coherence decrease for periods below 20 hour and is below about 0.5 for shorter periods than 10 hours. The coherence between modeled and observed sea levels is high and the phase differences are small at all stations for periods longer than 20 hours. For the really long periods the phase difference increase somewhat. Especially in central Baltic proper, namely Landsort and Ölands Norra Udde, observed sea levels have a daily cycle that is not caught by the model. The driving forces behind the daily cycle is evidently not resolved by the model.

A quantitative skill assessment of the standard case and a number of simulations with varying bottom drag coefficient, wind forcing and wave drag is made in terms of correlation squared (r^2) and root mean squared (RMS) error. To avoid corruption from the spin-up of the model all statistics are computed excluding the initial 30 days, leaving 8040 data points for the statistics. Since changing friction and resolution of the model greatly influence the filling and emptying of the Baltic through the Danish Straits, we also made a simple estimate of the high-frequency

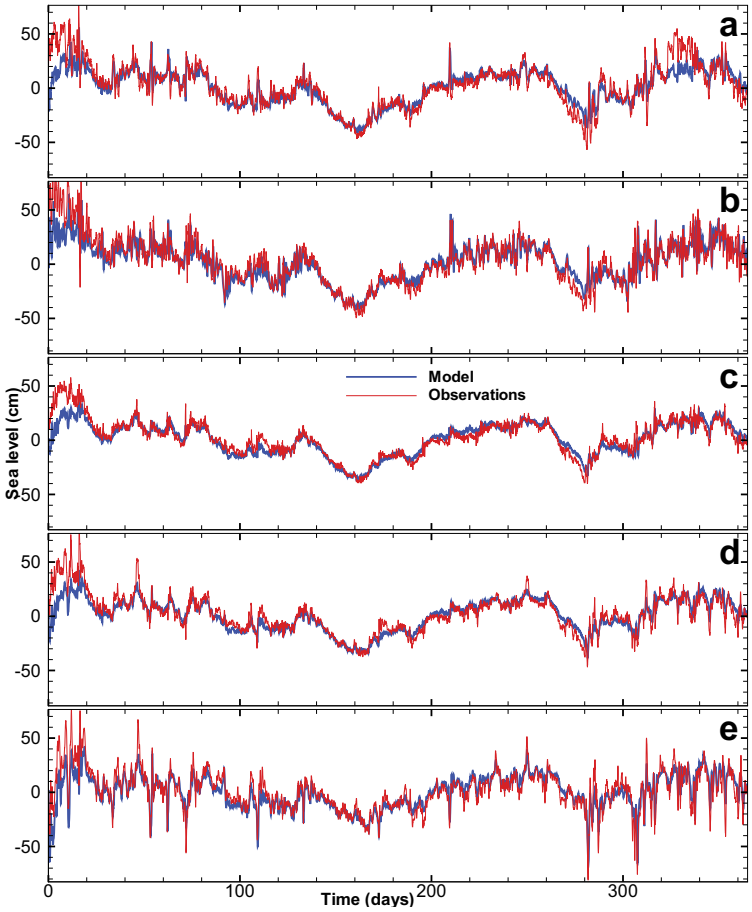

Figure 3: Observed and modeled sea levels at Forsmark (a), Helsinki (b), Landsort (c), Ölands Norra Udde (d) and Simrishamn (e).

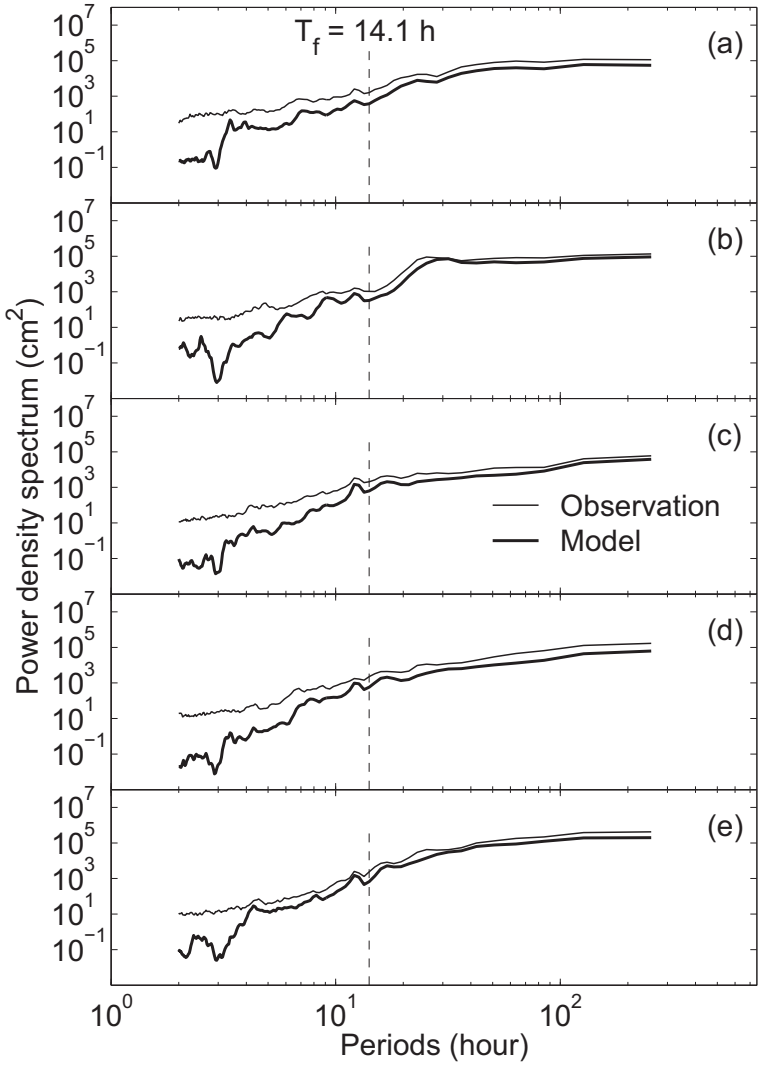

Figure 4: Spectra of simulated and observed sea levels at Forsmark (a), Helsinki (b), Landsort (c), Ölands Norra Udde (d) and Simrishamn (e).

part of the error that to a larger degree reflects effects of changing parameters on the internal oscillations of the Baltic Sea (e.g. Samuelsson and Stigebrandt, 1996). The high-frequency part of the RMS error is estimated by first cutting the time-series into 240 h long time-slices and for each of these compute error variance and then compute RMS error from the average of these variances, i.e.,

$$RMS_h = \sqrt{\frac{1}{M}\sum_{m=1}^{M}\frac{1}{N}\sum_{n=1}^{N}\left(\eta_{n,m}^{mod} - \bar{\eta}_m^{mod} - \eta_{n,m}^{obs} + \bar{\eta}_m^{obs}\right)^2} \tag{28}$$

where η^{mod} and η^{obs} are modeled and observed sea levels, respectively. $N = 240$ is the number of observations in each of the $M = 33$ slices. Quantities with bars above are averaged for each slice. In addition to the correlation and RMS computations we made a Kruskal-Wallis non-parametric ANOVA test to elucidate which simulations that gave a significantly different result compared to the simulation with the standard parameter setting (i.e.,$p < 0.05$ for the null hypoth-

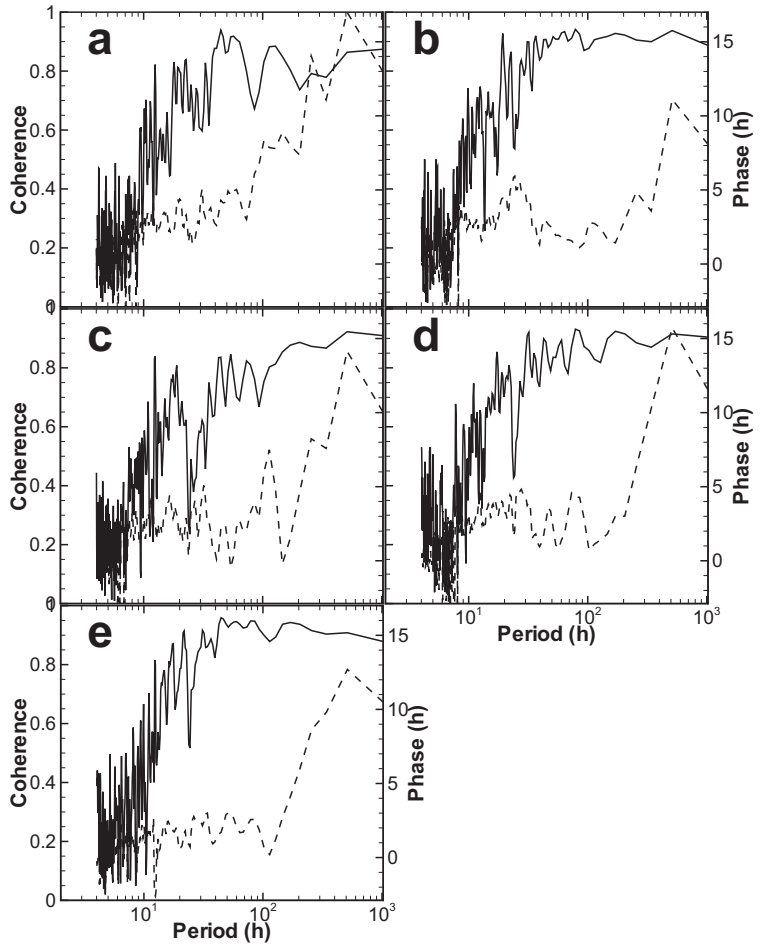

Figure 5: Coherence and phase spectra between observed and simulated sea levels at a) Forsmark, b) Helsinki, c) Landsort, d) Ölands Norra Udde and e) Simrishamn.

esis that they are similar). We also performed the test between simulations and observations, and found that all simulation results were significantly different from the observations.

The correlations and RMS errors for all runs are summarized in Tables 1 and 2. Also indicated in Table 1 are the results from the Kruskal-Wallis test, showing that only a few of the test cases are significantly different from the control run. The correlation between observed and simulated sea levels are in general quite high and RMS errors are less than 50% of the standard deviation of the observed sea level records. Highest correlation and lowest RMS errors was found at Landsort followed by Ölands Norra Udde, for the cases with 25%-50% increased wind stress. It is quite evident that increased wind forcing improves correlation for sea level stations inside the Baltic proper. However, for Forsmark, increased wind stress with 25 and 50 % did not change the correlation at all and for 75 % increase the correlation decreases. When changing the bottom drag coefficient from 1 to 8 $\times 10^{-3}$, highest correlations and lowest RMS errors were found for the standard case for all the stations, except Forsmark and Simrishamn where the extremes occurred for $C_d = 2 \times 10^{-3}$ and $C_d = 4 \times 10^{-3}$, respectively. It is evident that bottom stress on the flows through the Åland Sea is important for the sea level variations at Forsmark. Minimal high frequency only RMS errors are in general shifted towards a lower

Table 1: Correlation (r^2) between hourly observed and modeled sea levels (8040 data points each) for each of the simulations. Highest correlations are emphasized with italic typeface. The cases that are significantly different ($p < 0.05$ for the null hypothesis that they are similar) from the standard case are marked with a star.

Stations	Forsmark	Helsinki	Landsort	Ölands Norra Udde	Simrishamn
$C_d = 3 \times 10^{-3}$	0.907	0.913	0.947	0.926	0.893
$C_d = 1 \times 10^{-3}$	0.908*	0.902*	0.939*	0.920*	0.874
$C_d = 2 \times 10^{-3}$	*0.911*	0.912	0.947	0.926	0.889
$C_d = 4 \times 10^{-3}$	0.901	0.911	0.944	0.922	0.894
$C_d = 6 \times 10^{-3}$	0.890	0.904	0.937*	0.914*	0.892
$C_d = 8 \times 10^{-3}$	0.879*	0.897*	0.929*	0.905*	0.886*
No wave drag	0.907	0.912	0.947	0.926	0.895
Approx. wave drag	0.906	0.915	0.947	0.926	0.895
$\mathbf{F_w}$+25%	0.907	*0.916*	0.951	0.936	0.913
$\mathbf{F_w}$+50%	0.905	0.915	*0.952*	0.943	*0.923*
$\mathbf{F_w}$+75%	0.894	0.906	0.950	*0.944*	0.921
4x4 nm	0.854	0.861	0.902*	0.876*	0.878
1x1nm	0.909	0.915	0.949	0.928	0.895

bottom drag coefficient, $C_d = 2 \times 10^{-3}$. Most extreme difference is at Simrishamn where lowest overall RMS error is found for $C_d = 4 \times 10^{-3}$ and the lowest high frequency RMS error is found for $C_d = 1 \times 10^{-3}$. Increasing grid resolution from 2x2 to 1x1 nm gave only trivial changes in the correlation, but lowering the resolution to 4x4 nm gave a significant reduction. The difference between the total and high frequency RMS errors indicate that lowering the resolution reduce the accuracy primarily at low frequencies and therefore we can conclude that the flows through the Danish Straits are less correctly simulated in the coarse resolution case. The simulation with no wave drag and the approximate wave drag (Eq. 21) gives no change in the correlation compared to the standard case, which indicates that wave drag have only little influence on the coastal sea levels.

4. Results

4.1. Dissipation of energy from barotropic motion

The horizontal distribution of time-averaged dissipation of energy from the barotropic motion by internal wave drag and bottom friction are drawn in Fig. 6. The temporally averaged dissipation by wave drag is large along the 50 m isobath off the eastern and north-western coasts of the Baltic proper (Fig. 6a). The spatial distribution is quite patchy and a number of hot spots can be identified, usually associated with abrupt changes in the bathymetry. For example, the entrance area of the Gulf of Finland seems to be one of these. A closer inspection of the simulated currents (not shown here) reveals a shallow coastal jet flowing northward along the eastern coast of the Baltic proper. When the coastal current enters the Gulf of Finland the barotropic motion seems to dissipate within a short distance. As would be expected bottom stress is high at shallow depths close to the shore. Especially along the eastern coasts of the Baltic proper, the coastal current mentioned above gives rise to large bottom stress. This is also the case in southern Baltic Sea, where coastal currents are strong. Further in narrow straits, like the Åland Sea, and not the

Table 2: RMS error (in cm) between hourly observed and modeled sea levels (8040 data points each) for each of the simulations. The RMS errors computed from 240 h time-slices are given within parenthesis. Lowest RMS errors are indicated by italic typeface. The standard deviation of the observed time series, both in total and using 240 h slices are indicated for comparison.

Stations	Forsmark	Helsinki	Landsort	Ölands Norra Udde	Simrishamn
Standard dev	18.5(9.27)	18.0(10.1)	14.5(6.11)	14.6(7.77)	16.5(12.3)
$C_d = 3 \times 10^{-3}$	7.83(5.86)	7.33(6.60)	4.71(3.29)	5.57(4.33)	7.42(6.25)
$C_d = 1 \times 10^{-3}$	7.90(6.12)	8.28(7.02)	6.05(3.55)	6.58(4.18)	8.43(5.99)
$C_d = 2 \times 10^{-3}$	*7.61*(5.86)	7.45(6.66)	4.95(3.23)	5.72(4.16)	7.64(6.06)
$C_d = 4 \times 10^{-3}$	8.14(5.90)	7.44(6.62)	4.78(3.41)	5.66(4.51)	7.40(6.42)
$C_d = 6 \times 10^{-3}$	8.74(6.01)	7.82(6.69)	5.18(3.65)	6.04(4.79)	7.58(6.70)
$C_d = 8 \times 10^{-3}$	9.24(6.11)	8.23(6.76)	5.63(3.83)	6.46(5.00)	7.84(6.91)
No wave drag	7.82(*5.84*)	7.38(6.66)	4.72(3.30)	5.54(4.31)	7.36(6.19)
Approx. wave drag	7.85(5.90)	7.26(*6.54*)	4.72(3.30)	5.56(4.33)	7.37(6.22)
$\mathbf{F_w}$+25%	7.76(5.92)	7.26(6.66)	*4.61*(*3.26*)	5.21(4.07)	6.79(5.70)
$\mathbf{F_w}$+50%	7.88(6.13)	7.43(6.90)	4.62(3.30)	*4.99*(*3.91*)	*6.55*(*5.55*)
$\mathbf{F_w}$+75%	8.39(6.76)	8.12(7.64)	4.84(3.52)	5.03(4.00)	6.97(6.05)
4x4 nm	10.25(6.24)	9.43(7.10)	6.81(4.14)	7.52(5.20)	8.29(6.92)
1x1nm	7.78(5.88)	*7.24*(*6.54*)	4.62(*3.26*)	5.48(4.32)	7.36(6.24)

least, in the narrow Danish straits and Kattegat (not shown) dissipation by bottom stress is large due to strong currents.

We have computed averages from four areas, indicated by letters A-D in Fig. 6. Areas A and B cover the two deepest basins, Landsort deep (monitoring station BY31) and Eastern Gotland basin (BY15), respectively. Area C covers the Baltic proper without the marginal gulfs and Box D covers Åland Sea. The energy losses due to internal wave drag and bed friction averaged in the different areas are presented in Table 3. To get an overview on difference between shallow and deep areas, we computed the average dissipation due to internal wave drag and bottoms stress over areas in selected depths intervals. The dissipation by bottom stress is much smaller in deeper than in shallower water, as expected from the spatial distributions above. The dissipation due to wave drag seems to be of similar magnitude in deep water as in shallow water areas, which makes the relative contribution of internal wave drag to the loss of barotropic energy larger at deep water areas. The results for the different areas are quite different in details. In the Baltic proper as a whole (area C) the mean dissipation to internal waves is 0.23 mW m^{-2}, which is only a fraction of the dissipation by bottom stress (1.3 mW m^{-2}). However, dissipation by wave drag remain approximately constant for all depth intervals so that in waters deeper than 50 m the two causes of dissipation are of comparable magnitude ($\sim$ 0.2 - 0.4 mW m^{-2}). The largest dissipation by wave drag is found at depth in area D, up to about 2 mW m^{-2}. In areas A and B, where two of the deepest areas are located, dissipation by wave drag is higher or equal to that from bottom stress, even though in area B, the dissipation by wave drag decreases with depth for areas deeper than 100 m.

The temporal variability of dissipation by internal wave drag is quite large, which is exemplified by a time-series for area C in Fig. 7. The average for the area is shown with thin dashed line. During strong events wintertime, the internal wave drag reaches levels of almost 3 mW m^{-2}, or a factor of ten larger than the average. Making a simple statistics shows that the mean

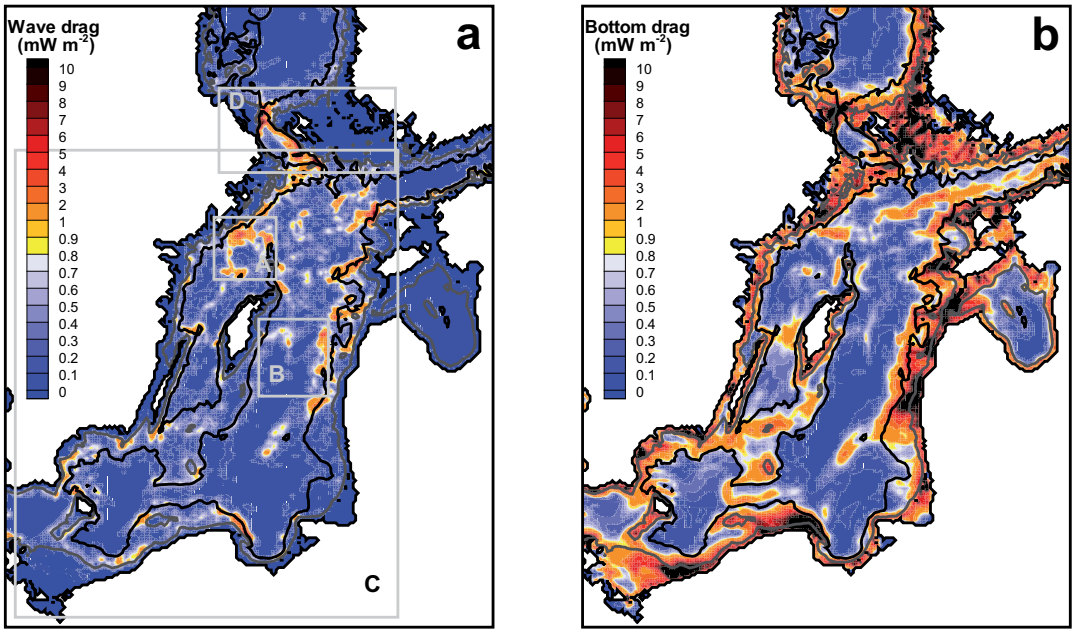

Figure 6: Spatial variation of time-average dissipation by internal wave drag (panel a) and by bottom stress (panel b). Indicated are also depth contours for 20 m (grey) and 50 m (black). area A covers the Landsort deep, B the Gotland deep, C the Baltic proper and D the Åland Sea.

duration of periods when the dissipation is larger than average is 44 hours for area C and in total dissipation is above average during slightly less the 30% of the time. The results for the other areas are similar.

The seasonal signal is even more evident from the monthly mean of the dissipation by internal wave drag for areas A-D (see Fig. 8). Maximal monthly dissipation is almost an order of magnitude larger than the minimal.

4.2. Contribution to mixing

Horizontal averages of dissipation are computed for areas deeper than a specified depth. The dissipation by wave drag and bottom stress as function of depth are drawn in Fig. 9 for areas A, B and D. The dissipation by wave drag is sub-divided into the contributions from 1st, 2nd and the sum of 3rd-10th dynamic modes. Under the bold assumption that, dissipation that occur below a certain depth level contributes to mixing only there, and not above that level, we can regard this (Fig. 9) as the supply of mechanical energy. In that case, a fraction given by the flux Richardson number ($R_f \approx 0.05 - 0.2$) could be used for mixing. We see clearly that the dissipation below 50 m or so is too weak to explain the total supply needed of some 2.1 mW m^{-2} (Liljebladh and Stigebrandt, 2000) mentioned in the introduction. However, at greater depths the required energy supply for mixing seems to be quite smaller. Axell (1998) computed the energy supply needed to sustain work against the buoyancy forces in the deepest parts of Landsort deep (area A) and Eastern Gotland deep (area B) from changes in density during stagnation periods. Assuming $R_f = 0.05$, Axell (1998, figure 10) obtained average energy supply for mixing of about 5 and 0.6 mW m^{-2} to the deep water below 150 m, in areas A and B, respectively. The model results give average dissipation of wave drag of 0.62 and 0.14 mW m^{-2}, respectively, for these areas

Table 3: Spatial and temportal averages of dissipation due to internal wave drag and bottom drag in the standard case. Averages are done for sub-areas defined by different depth intervals; the "All" column refers all depths, i.e., to the whole area.

Internal wave drag (mWm^{-2})						
Area	All	0-50 m	50-100 m	100-150 m	150-200 m	200-250 m
A	0.61	0.44	0.72	0.62	0.41	0.95
B	0.29	0.32	0.59	0.25	0.15	0.10
C	0.23	0.21	0.24	0.26	0.26	0.28
D	0.43	0.22	1.09	2.08	2.07	0.88
Bottom stress (mWm^{-2})						
Area	All	0-50 m	50-100 m	100-150 m	150-200 m	200-250 m
A	1.10	3.15	0.53	0.74	0.38	0.33
B	0.50	1.90	1.25	0.20	0.10	0.11
C	1.55	2.82	0.49	0.36	0.22	0.15
D	4.09	4.74	1.48	1.24	0.76	0.50

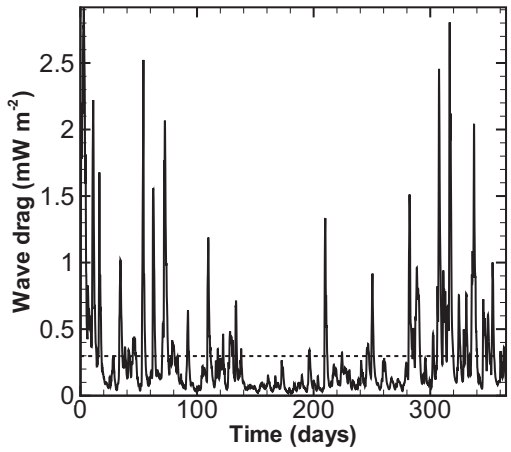

Figure 7: Horizontally averaged dissipation by internal wave drag for box C, the Baltic Proper. The thin dashed line indicates the annual mean dissipation by internal wave drag (0.23 mW m^{-2}).

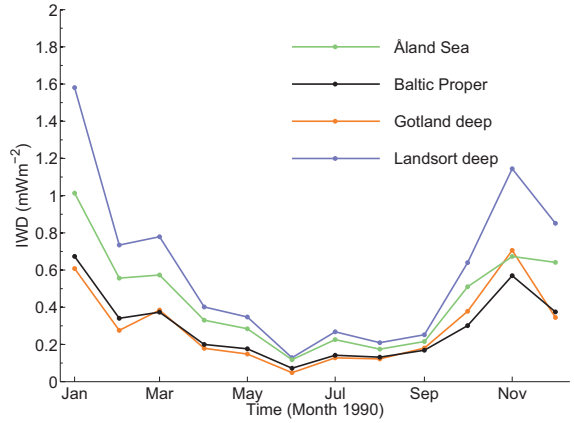

Figure 8: Monthly mean of horizontally averaged dissipation by internal wave drag for Landsort deep (area A), Gotland deep (area B), Baltic proper (area C) and Åland Sea (area D).

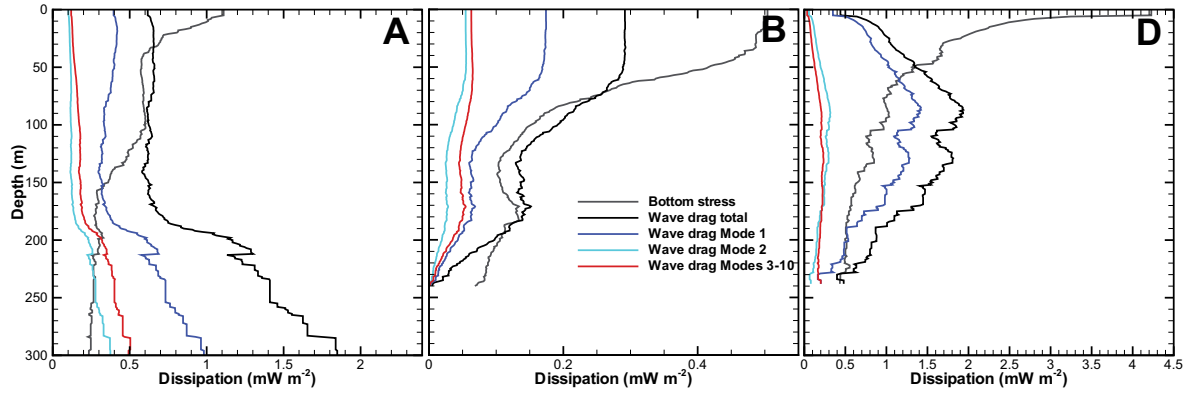

Figure 9: Spatial average of dissipation due to bottom stress and wave drag over areas covering depths deeper than the depth on the y-axis. Total wave drag and the contributions from the 1st, 2nd and the sum of 3rd-10th dynamic modes are drawn. There is one panel each for the areas A, B and D as defined in figure 6.

below 150 m depth (see Fig. 9). Although this is only 12.5% and 25% of the needed supply, it is clearly an indication that processes involving internal wave generation by barotropic currents can be important.

The vertical variation of dissipation due to internal wave drag is quite different in the different areas (Fig. 9). In area A the dissipation increases with depth, while a definite decrease to zero is found in area B. This conforms broadly with Axell (1998) who found that the work against buoyancy forces decreased with depth in both areas, however, he found that the decrease started at above 300 m depth in area A and this might not be resolved in the present model. In area D, there is a definite maximum in dissipation around 100 m depth and the profile is quite different from the other two areas. The contribution seems to be dominated by the 1st dynamic mode; most probably due to strong generation at the two sills delimiting the basin water. The influence from higher order modes become prominent at depth, especially in area B where they contribute with about 40%, but also in area A.

The contribution from bottom stress to mixing in deep waters should be interpreted with great caution, since most probably the bottom near currents here are determined to a large extent on the baroclinic response.

4.3. Sensitivity

There are uncertainties in parameters and forcing of the model that could not be fully resolved by the comparison with sea level observations above. Therefore, we make an assessment of the sensitivity of results on dissipation. The averaged dissipation due to wave drag and bottom drag for the different model experiments are shown in Tables 4 - 7. The experiments with different bottom drag coefficients show that, in general, dissipation both by wave drag and by bottom stress decreases with higher drag coefficient. The decrease in dissipation by bottom stress does not apply to area B, however, where dissipation instead increases for increased drag coefficient. The sensitivity of dissipation by bottom stress on the drag coefficient decreases with depth, while the sensitivity remains high for dissipation by wave drag in the deep. Dissipation by bottom stress is quite sensitive to absence or to parameterization of internal wave drag. The extreme cases are for example in area D, where removing wave drag causes more than a doubling of dissipation by bottom drag at depth and the approximate wave drag reduces it to half. The approximate wave

Table 4: Spatial average in area A of dissipation by internal wave drag and bottom stress over sub-areas deeper than the depth given in the table.

	Internal wave drag (mWm^{-2})					Bottom stress (mWm^{-2})				
	0 m	50 m	100 m	150 m	200 m	0 m	50 m	100 m	150 m	200 m
$C_d = 3 \times 10^{-3}$	0.61	0.65	0.62	0.62	1.17	1.10	0.57	0.59	0.36	0.30
$C_d = 1 \times 10^{-3}$	1.05	1.10	1.02	1.05	2.01	1.19	0.41	0.40	0.26	0.24
$C_d = 2 \times 10^{-3}$	0.76	0.81	0.76	0.77	1.46	1.15	0.52	0.53	0.33	0.29
$C_d = 4 \times 10^{-3}$	0.52	0.56	0.53	0.52	0.98	1.05	0.59	0.62	0.37	0.30
$C_d = 6 \times 10^{-3}$	0.40	0.44	0.42	0.40	0.75	0.98	0.61	0.64	0.38	0.29
$C_d = 8 \times 10^{-3}$	0.33	0.36	0.35	0.33	0.62	0.92	0.61	0.64	0.38	0.29
No drag	0.00	0.00	0.00	0.00	0.00	1.76	1.22	1.15	0.91	1.47
Approx. drag	0.89	1.11	1.28	1.19	1.55	0.93	0.29	0.26	0.13	0.07
$\mathbf{F_w}$+ 25%	0.84	0.90	0.86	0.88	1.67	1.63	0.90	0.94	0.59	0.52
$\mathbf{F_w}$+ 50%	1.09	1.18	1.14	1.18	2.25	2.26	1.32	1.37	0.89	0.80
$\mathbf{F_w}$+ 75%	1.38	1.50	1.46	1.54	2.97	3.06	1.87	1.96	1.31	1.20
4x4 nm	0.65	0.71	0.69	0.77	1.24	0.97	0.50	0.48	0.37	0.17
1x1 nm	0.53	0.55	0.52	0.53	1.05	1.08	0.61	0.64	0.38	0.39

drag cause significantly larger dissipation in deep areas than the full wave drag formulation, showing that it is probably not applicable for estimation of energy supply to deep water mixing. Increased wind stress increases dissipation due to both wave drag and bed friction. At depth they typically doubles when wind stress is increased with 50%.

Dissipation due to wave drag systematically decreases with higher spatial resolution, while changes of dissipation due to bed friction are not systematic. The sensitivity is modest when all depths are included. The changes are larger at depth, most extreme is below 200 m in area D where dissipation due to wave drag decreases with a factor of 4.5 going from 4x4 nm to 1x1 nm resolution. The deeper regions of area A are less sensitive to horizontal resolution with only modest changes in dissipation. At greater depths in area B decreased dissipation by wave drag seems to be compensated by increased dissipation by bottom stress. Largest decrease is seen from 2 to 1 nm for dissipation due to wave drag, which applies to all areas.

5. Discussion

We have shown that transfer of energy from low-frequency wind forced barotropic motions to internal waves potentially is an important driver of diapycnal mixing in the Baltic Sea. However, we get an average dissipation from internal wave drag over stratified parts (depth > 50 m) of the Baltic proper of about 0.25 mW m^{-2} (Table 6) and that is substantially less than the required energy supply of 2.1 mW m^{-2} (Liljebladh and Stigebrandt, 2000). The sensitivity study shows that this can be an underestimate and the model can give up to 0.4 mW m^{-2} without significantly reducing performance in reproducing observed sea levels. However, there are no simple means to increase the dissipation by internal wave drag further, i.e., by increasing wind speeds or changing drag coefficients. The estimates of dissipation by internal wave drag at depth in areas A and B were compared to the needed energy supply estimated by Axell (1998). He estimated that about

Table 5: Same as Table 4 but for area B.

	Internal wave drag (mWm^{-2})					Bottom stress (mWm^{-2})				
	0 m	50 m	100 m	150 m	200 m	0 m	50 m	100 m	150 m	200 m
$C_d = 3 \times 10^{-3}$	0.29	0.28	0.19	0.14	0.10	0.50	0.41	0.15	0.10	0.11
$C_d = 1 \times 10^{-3}$	0.44	0.43	0.30	0.22	0.17	0.32	0.25	0.09	0.07	0.08
$C_d = 2 \times 10^{-3}$	0.34	0.34	0.23	0.16	0.12	0.44	0.35	0.13	0.09	0.10
$C_d = 4 \times 10^{-3}$	0.25	0.25	0.16	0.12	0.08	0.52	0.44	0.17	0.12	0.11
$C_d = 6 \times 10^{-3}$	0.20	0.20	0.13	0.10	0.07	0.55	0.47	0.19	0.13	0.12
$C_d = 8 \times 10^{-3}$	0.17	0.17	0.11	0.08	0.06	0.55	0.48	0.20	0.14	0.12
No drag	0.00	0.00	0.00	0.00	0.00	0.83	0.74	0.37	0.25	0.24
Approx. drag	0.39	0.42	0.34	0.30	0.28	0.40	0.29	0.05	0.03	0.03
$\mathbf{F_w}$+ 25%	0.39	0.39	0.26	0.18	0.13	0.79	0.66	0.24	0.17	0.16
$\mathbf{F_w}$+ 50%	0.51	0.50	0.34	0.24	0.17	1.16	0.97	0.36	0.25	0.24
$\mathbf{F_w}$+ 75%	0.64	0.64	0.43	0.30	0.21	1.65	1.38	0.53	0.36	0.34
4x4 nm	0.30	0.29	0.20	0.17	0.14	0.56	0.39	0.13	0.08	0.09
1x1 nm	0.24	0.24	0.15	0.10	0.07	0.49	0.40	0.17	0.12	0.12

Table 6: Same as Table 4 but for area C.

	Internal wave drag (mWm^{-2})									
	0 m	50 m	100 m	150 m	200 m					
	Internal wave drag (mWm^{-2})					Bottom stress (mWm^{-2})				
	0 m	50 m	100 m	150 m	200 m	0 m	50 m	100 m	150 m	200 m
$C_d = 3 \times 10^{-3}$	0.23	0.25	0.27	0.29	0.44	1.55	0.43	0.32	0.21	0.17
$C_d = 1 \times 10^{-3}$	0.44	0.45	0.45	0.49	0.75	1.88	0.35	0.25	0.16	0.13
$C_d = 2 \times 10^{-3}$	0.29	0.31	0.33	0.36	0.55	1.67	0.41	0.30	0.19	0.16
$C_d = 4 \times 10^{-3}$	0.19	0.21	0.23	0.25	0.37	1.45	0.45	0.34	0.22	0.17
$C_d = 6 \times 10^{-3}$	0.15	0.17	0.18	0.20	0.29	1.32	0.46	0.35	0.24	0.17
$C_d = 8 \times 10^{-3}$	0.12	0.14	0.15	0.17	0.24	1.23	0.46	0.36	0.25	0.18
No drag	0.00	0.00	0.00	0.00	0.00	1.77	0.69	0.59	0.47	0.62
Approx. drag	0.21	0.38	0.59	0.63	0.70	1.60	0.36	0.16	0.08	0.04
$\mathbf{F_w}$+ 25%	0.30	0.34	0.36	0.40	0.63	2.24	0.68	0.52	0.34	0.28
$\mathbf{F_w}$+ 50%	0.39	0.43	0.47	0.52	0.84	3.08	0.97	0.75	0.50	0.41
$\mathbf{F_w}$+ 75%	0.49	0.54	0.60	0.67	1.09	4.14	1.39	1.07	0.73	0.61
4x4 nm	0.28	0.30	0.32	0.40	0.44	1.65	0.45	0.32	0.20	0.11
1x1 nm	0.16	0.18	0.19	0.21	0.36	1.26	0.38	0.32	0.21	0.20

Table 7: Same as Table 4 but for area D.

	Internal wave drag (mWm^{-2})					Bottom stress (mWm^{-2})				
	0 m	50 m	100 m	150 m	200 m	0 m	50 m	100 m	150 m	200 m
$C_d = 3 \times 10^{-3}$	0.43	1.34	1.83	1.56	0.88	4.09	1.30	0.95	0.65	0.50
$C_d = 1 \times 10^{-3}$	0.76	2.25	2.97	2.55	1.34	4.84	1.04	0.72	0.53	0.35
$C_d = 2 \times 10^{-3}$	0.53	1.62	2.18	1.86	1.02	4.41	1.21	0.86	0.60	0.43
$C_d = 4 \times 10^{-3}$	0.37	1.16	1.61	1.38	0.79	3.86	1.36	1.01	0.69	0.55
$C_d = 6 \times 10^{-3}$	0.30	0.95	1.34	1.16	0.67	3.51	1.42	1.10	0.76	0.64
$C_d = 8 \times 10^{-3}$	0.25	0.82	1.17	1.02	0.60	3.27	1.46	1.16	0.82	0.70
No drag	0.00	0.00	0.00	0.00	0.00	4.48	2.32	2.20	1.63	1.11
Approx. drag	0.56	2.59	4.42	4.33	3.80	4.00	0.81	0.31	0.25	0.28
$\mathbf{F_w}$+ 25%	0.55	1.72	2.37	2.04	1.16	5.88	1.91	1.41	0.98	0.77
$\mathbf{F_w}$+ 50%	0.68	2.14	2.96	2.57	1.49	7.94	2.65	1.98	1.39	1.11
$\mathbf{F_w}$+ 75%	0.84	2.63	3.66	3.20	1.88	10.61	3.58	2.72	1.94	1.58
4x4 nm	0.44	1.27	2.59	2.44	2.75	4.30	1.10	0.79	0.55	0.58
1x1 nm	0.38	1.23	1.41	0.98	0.48	3.92	1.45	0.96	0.66	0.55

5 and 0.6 mW m^{-2} needed to be supplied to these areas below 150 m depth compared to the dissipation by internal waves of 0.62 and 0.14 mW m^{-2}. The sensitivity analysis indicates a large uncertainty in the dissipation here. Taking an extreme case: The dissipation in area A is quite sensitive on depth and wind forcing, so if limiting the average to deeper areas than 200 m and assuming that wind stress should be increased with 50%, the dissipation becomes 2.25 mW m^{-2} instead. The high-wind speed case gives a dissipation due to wave drag of about 0.24 mW m^{-2} in area B.

An uncertainty in the comparison between estimations of needed energy supply to explain observed changes in stratification with estimates of the energy supply is that the former are calculated using the Richardson flux number (R_f), or mixing efficiency. Liljebladh and Stigebrandt (2000) used $R_f = 0.06$ and Axell (1998) used $R_f = 0.05$, but commonly used is values up to $R_f = 0.17$ originating from Osborn (1980). Arneborg (2002) suggested an intermediate value $R_f = 0.11$ from theoretical considerations. Anyhow, the factor of three difference in various estimates of R_f may imply an even larger importance energy supply to mixing from wind-forced internal waves.

The parameterization of internal wave drag is derived from quite simplified theory and the consequences of this need to be discussed. In the parameterization of wave drag force we neglect that internal waves are generated on both sides of the step. The energy density of the waves on the shallow side is however much less than on the deep side. Interpreting the idealized analysis by St. Laurent et al. (2003), it seems that neglecting internal waves on the shallow side of the step may potentially underestimate the wave drag with some 20%.

Further are not effects from Earth rotation taken into account, which could be dubious for long-period oscillations. There are however examples of similar parameterizations being used to quantify the internal wave generation from sub-inertial tides (e.g Tanaka et al., 2007). The generation itself should be relatively well described by the non-rotating model if no interference occurs and this would be the case if the waves dissipate at generation or at least within an oscil-

lation period typical of the driving force. Our hypotheses are that the rough complex topography favors rather rapid breaking of the internal waves and that the lack of phase locked frequencies in the wind forcing decreases the probability of interference further. An ultimate test would naturally be a measurement program that investigates the generation processes in the Baltic proper. Arneborg (2000) performed a derivation of internal wave generation at a sill in a channel from slowly oscillating barotropic flows, taking into account generation of baroclinic Kelvin waves. The formula he obtained had the same functional dependence on stratification and barotropic flow as the original step model formulation (Stigebrandt, 1976).

All steps between grid cells are treated as autonomous wave makers in that we do not consider any interaction between waves generated in adjacent cells. Supporting this assumption, it was recently shown experimentally that two very closely spaced sills (about 1 km or 1/7 of the internal Rossby radius) generated internal tides without interaction (Johnsson et al., 2007). This result was obtained by comparing theoretical energy transfer with observed tidal currents, sea level and stratification.

St. Laurent et al. (2003) showed that the calculations of internal tide generation using the step-model can be sensitive to the resolution. This would in our case be transferred to sensitivity to grid resolution in the model. In our simulations, a change in grid size from 4, 2 and 1 nautical mile systematically decreased the average dissipation due to wave drag, but the total changes were not larger than other uncertainties. The comparison of dissipation in the deep basins was also somewhat difficult because they are quite small, so using the 4x4 nm grid barely resolves the deeps. Further, there is no 1x1 nm resolution grid available, so that was constructed by interpolating the 2x2 nm grid and thus did not contain additional roughness that could be present on finer scale. Thus, it was not possible with the present model set up to make definite calculations on the sensitivity on the grid resolution on the internal wave generation parameterization itself, so this must be left to be resolved in a future investigation.

Döös et al. (2004) proposed a parameterization of drag force in shallow water models that takes into account the loss due to flow separation due to resolved topographic obstacles. The functional form of the parameterization resembles wave drag. The discrete form of the drag force in the x-direction according to Döös et al. (2004), say F_D^x, is given by

$$F_D^x = -C_S \, |u| \, \frac{H_b - d}{\Delta s} u \tag{29}$$

This has clear similarities with the approximate wave drag derived in this paper (Eq. 21). The obvious difference between the drag forces is that the slope friction parameterization is scaled with current speed while wave drag is scaled with the internal group speed. Given that Döös et al. (2004) found an optimal fit to observed sea level variations for C_S of between 15 and 26 and that current speed is typically at least an order of magnitude less than the group velocity for long internal waves of the first mode, the two parameterizations give drag forces of similar order of magnitude. We have not repeated the detailed calibration to observed sea levels that Döös et al. (2004) performed, but according to our results using the approximate wave drag does not improve the model's capability to reproduce the observed sea level time-series. The cause for discrepancy is most probably that the primary influence on sea levels comes from drag at shallow regions in straits and close to the coasts, and here the approximate wave drag is zero in contrary to slope-friction.

Acknowledgements. Meteorological data was provided by the BALTEX data center, sea level, stratification and current data was provided by Swedish Meteorological and Hydrologi-

cal Institute, Finnish Marine Institute and Danish Meteorological Institute. This work has been funded by the Swedish Research Council under the G 600-335/2001 and 621-2003-3425 contracts; and by the Swedish Foundation for Strategic Environmental Research via the MARE program. This is contribution no. XX from Tellus, the Centre of Earth Systems Science at the University of Gothenburg.

We thank Ph.D. Lars Arneborg and Prof Anders Stigebrandt for fruitful discussions and valuable comments on earlier versions of this paper.

References

Arakawa, A., Lamb, V. R., 1981. A potential enstrophy and energy conserving scheme for the shallow water equations. Monthly Weather Review 109 (), 18–36.

Arbic, B. K., Garner, S. T., Hallberg, R. W., Simmons, H. L., 2004. The accuracy of surface elevations in forward global barotropic and baroclinic tide models. Deep-Sea Res. II 51 (), 3069–3101.

Arneborg, L., 2000. Oceanographic studies of internal waves and diapycknal mixing. Ph.D. Thesis A59, Earth Sci. Cent., University of Gothenburg, Sweden.

Arneborg, L., 2002. Mixing efficiencies in patchy turbulence. Journal of Physical Oceanography 32 (5), 1496–1506.

Axell, L. B., 1998. On the variability of Baltic Sea deepwater mixing. Journal of Geophysical Research 103 (C10), 21,667–21,682.

Berntsen, J., Xing, J., Davies, A. M., 2008. Numerical studies of internal waves at a sill: Sensitivity to horizontal grid size and subgrid scale closure. Cont. Shelf Res. 28 (), 1376–1393.

Döös, K., Nycander, J., Sigray, P., 2004. Slope-dependent friction in a barotropic model. J. Geophys. Res. 109 (C1).

Dyer, K. R., 1986. Coastal and estuarine sediment dynamics. John Wiley & Sons Ltd., Chichester.

Egbert, G., Ray, R., Bills, B., 2004. Numerical modeling of the global semidiurnal tide in the present day and in the last glacial maximum. J. Geophys. Res. 109 (C3).

Flather, R. A., 1976. A tidal model of the northwest European continental shelf. Mem. Soc. Roy. Sci. Liege Ser. 6 10 (), 141–160.

Gustafsson, B. G., Andersson, H. C., 2001. Modeling the exchange of the Baltic Sea from the meridional atmospheric pressure difference across the North Sea. Journal of Geophysical Research 106 (C9), 19731–19744.

Gustafsson, K. E., 2001. Computations of the energy flux to mixing processes via baroclinic wave drag on barotropic tides. Deep-Sea Research I 48, 2283–2295.

Jakobsen, F., Azam, M. H., Mahboob-ul Kabir, M., 2002. Residual flow in the Meghna Estuary on the coastline of Bangladesh. Estuar. Coast. Shelf Sci. 55 (), 587–597.

Jayne, S. R., St Laurent, L. C., 2001. Parameterizing tidal dissipation over rough topography. Geophysical Research Letters 28 (5), 811–814.

Johnsson, M., Green, J. A. M., Stigebrandt, A., 2007. Baroclinic wave drag from two closely spaced sills in a narrow fjord as inferred from basin water mixing. J. Geophys. Res. 112.

Kuzmina, N., Rudels, B., Stipa, T., Zhurbas, V., 2005. The structure and driving mechanisms of the Baltic intrusions. J. Phys. Oceanogr. 35, 1120–1137.

Liljebladh, B., Stigebrandt, A., 2000. The contribution of the surface layer via internal waves to the energetics of deep-water mixing in the baltic. Paper III in the Ph.D. Thesis A56, Earth Sci. Cent., University of Gothenburg, Sweden.

Martinsen, E. A., Engedahl, H., 1987. Implementation and testing of a lateral boundary scheme as an open boundary-condition in a barotropic ocean model. Coastal Engineering 11 (5-6), 603–627.

Meier, H. E. M., 2005. Modeling the age of Baltic Sea water masses: Quantification and steady state sensitivity experiments. Journal of Geophysical Research 110 (C02006), 1–14.

Meier, H. E. M. ., Feistel, R., Piechura, J., Arneborg, L., Burchard, H., Fiekas, V., Golenko, N., Kuzmina, N., Mohrholz, V., Nohr, C., Paka, V. T., Sellschopp, J., Stips, A., Zhurbas, V., 2006. Ventilation of the Baltic Sea deep water: A brief review of present knowledge from observations and models. Oceanologia 48 (S), 133–164.

Merrifield, M. A., Holloway, P. E., 2002. Model estimates of M_2 internal tide energetics at the Hawaiian Ridge. J. Geophys. Res. 107 ().

Niwa, Y., Hibiya, T., 2001. Numerical study of the spatial distribution of the M_2 internal tide in the Pacific Ocean. J. Geophys. Res. 106 (), 22,441–22,449.

Nycander, J., 2005. Generation of internal waves in the deep ocean by tides. J. Geophys. Res. 110 ().

Osborn, T., 1980. Estimates of the local rate of vertical diffusion from dissipation measurements. Journal of Physical Oceanography 10 (1), 83–89.

Press, W. H., Teukolsky, S. A., Vetterling, W. T., Flannery, B. P., 1997. Numerical Recipes, 2nd Edition. Cambridge Universiy Press, Cambridge.

Samuelsson, M., Stigebrandt, A., 1996. Main characteristics of the long-term sea level variability in the Baltic Sea. Tellus 48A (5), 672–683.
Seifert, T., Tauber, F., Kayser, B., 2001. A high resolution spherical grid topography of the baltic sea revised edition. In: Baltic Sea Science Congress. Stockholm.
Simmons, H. L., Hallberg, R. W., Arbic, B. K., 2004. Internal wave generation in a global baroclinic tide model. Deep-Sea Res. II 51 (), 3043–3068.
Sjöberg, B., Stigebrandt, A., 1992. Computations of the geographical distribution of the energy flux to mixing processes via internal tides and the associated vertical circulation in the ocean. Deep-Sea Research 39 (2A), 269–291.
Smith, S. D., 1980. Wind stress and heat flux over the ocean in gale force winds. J. Phys. Oceanogr. 10 (), 709–726.
Soulsby, R., 1997. Dynamics of marine sands - A manual for practical applications. Thomas Telford, London.
St. Laurent, L., Stringer, S., Garrett, C., Perrault-Joncas, D., 2003. The generation of internal tides at abrupt topography. Deep Sea Res. I 50 (8), 987–1003.
Stacey, M. W., 1984. The interaction of tides with the sill of a tidally energetic inlet. Journal of Physical Oceanography 14 (6), 1105–1117.
Stigebrandt, A., 1976. Vertical diffusion driven by internal waves in a sill fjord. Journal of Physical Oceanography 6, 486–495.
Stigebrandt, A., 1980a. Barotropic and baroclinic response of a semi-enclosed basin to barotropic forcing from the sea. In: Freeland, H. J., Farmer, D. M., Levings, C. D. (Eds.), Fjord Oceanography. Plenum, New York, pp. 151–164.
Stigebrandt, A., 1980b. Some aspects of tidal interactions with fjord constrictions. Estuarine Coastal Marine Science 11, 151–166.
Stigebrandt, A., 1999. Resistance to barotropic tidal flow in straits by baroclinic wave drag. Journal of Physical Oceanography 29, 191–197.
Stigebrandt, A., 2001. Physical Oceanography of the Baltic Sea. In: Wulff, F., Rahm, L., Larsson, P. (Eds.), A systems analysis of the Baltic Sea. Springer Verlag, pp. 19–74.
Stigebrandt, A., 2003. Regulation of vertical stratification, length of stagnation periods and oxygen conditions in the deeper deepwater of the Baltic proper. Meereswiss. Ber. 54, 69–80.
Stigebrandt, A., Aure, J., 1989. Vertical mixing in basin waters of fjords. Journal of Physical Oceanography 19 (7), 917–926.
Stigebrandt, A., Lass, H. U., Liljebladh, B., Alenius, P., Piechura, J., Hietala, R., Beszczýnska, A., 2002. DIAMIX – An experimental study of diapycnal deepwater mixing in the virtually tide-less Baltic Sea. Boreal Environmental Research 7 (4), 363–369.
Svensson, A., 2005. Observations of baroclinic eddies in the Baltic Sea. Tech. Rep. B472, Department of Oceanography, University of Gothenburg.
Tanaka, Y., Hibiya, T., Niwa, Y., 2007. Estimates of tidal dissipation and diapycnal diffusivity in the Kurul Straits using TOPEX/POSEIDON altimeter data. J. Geophys. Res. 112 ().
Tanaka, Y., Hibiya, T., Niwa, Y., Oct 2007. Estimates of tidal energy dissipation and diapycnal diffusivity in the kuril straits using topex/poseidon altimeter data. J. Geophys. Res. 112 (C10), 1–9.
Umgiesser, G., 1997. Modelling the Venice Lagoon. Int. J. Salt Lake Res. 6 (), 175–199.
Verboom, G. K., de Ronde, J. G., van Dijk, R. P., 1992. A fine grid tidal flow and storm surge model of the North Sea. Cont. Shelf Res. 12 (), 213–233.
Weis, P., Thomas, M., Sündermann, J., 2008. Broad frequency tidal dynamics simulated by a high-resolution global ocean tide model forced by ephemerides. J. Geophys. Res. 113 ().
Williamson, J., 1980. Low-storage Runge-Kutta schemes. J. Comp. Phys. 35 (), 48–56.

Paper III

Tellus (2007)
Printed in Singapore. All rights reserved

TELLUS

Ice dynamics in the Bothnian Bay inferred from ADCP measurements

By GÖRAN BJÖRK[1]*, CHRISTIAN NOHR[1], BO G. GUSTAFSSON[1] and AMUND E. B. LINDBERG[2], [1]*Department of Oceanography, Earth Science Center, Göteborg University, Box 460, SE 405 30, Göteborg, Sweden;* [2]*Umeå University, Umeå Marine Science Centre, Sweden*

(Manuscript received 9 February 2007; in final form 28 September 2007)

ABSTRACT

A bottom mounted ADCP has monitored the ice motion and thickness in Bothnian Bay, Baltic Sea during the entire winter season 2004. The ADCP was deployed at 20 m depth at Falkensgrund well outside the land fast ice zone. The data shows that the ice motion is primarily driven by the wind but with a clear influence of internal ice stresses. The ice stresses become more dominant as the ice grow thicker with increasing number of observations with nearly stationary ice for relatively high wind speeds. A clear dependence of the ice/wind speed ratio to wind shifts is detected with higher ratio in the new wind direction. The effect of strain hardening is also seen in several events as decreasing ice speed, sometimes to zero, in spite of constant wind speed and wind direction. A rough force balance computation gives a compressive ice strength of about 9×10^4 N m^{-2}, which is much larger than normally used in numerical ice models. The ice thickness data show numerous ice ridges with ice draft well above 1 m passing the instrument. The ridges make up a large portion, 30–50%, of the total ice volume showing that dynamical processes are important for the total ice production in the Bothnian Bay.

1. Introduction

In this study, we present and analyse observational data of sea ice drift, currents and ice thickness from a full ice season in the central part of the Bothnian Bay (Fig. 1). The observations were made with a bottom mounted Acoustic Doppler Current Profiler (ADCP) during the winter 2003–2004.

The drift of sea ice is mainly controlled by a balance between drag forces by the atmosphere and ocean, and internal stresses acting in-between ice floes and between ice floes and solid boundaries. When the internal stress is weak the coriolis force balances drag forces, and the ice motion is directed to the right of the wind on the northern hemisphere. The relation between internal stress in a medium, its material properties and the state of deformation is described by the rheology. The rheology problem of drift ice is particularly complicated since qualitatively and quantitative different laws apply to different packing densities and thickness of the ice floes (Leppäranta, 1998). One particularly important rheology parameter is the ice strength, which is primary a function of the ice thickness distribution and the compactness of the ice cover (Thorndike et al., 1975). Ice dynamics controls the deformation of the ice cover which in turn generates pressure ridges and open water. The dynamic processes are therefore intimately connected to the ice thickness distribution. For confined ice covers such in the Bay of Bothnia much of the dynamics is controlled by the solid boundaries at the coast line or land fast ice such that pressure ridges tend to build up at the windward side of the basin and open water forms at the leeward side. Better knowledge of ice dynamics and the thickness distribution has been identified as one of the key areas where more research is needed in the Baltic Sea (Omstedt et al., 2004).

The main objective with the present study is to investigate how the ice motion responds to wind forcing from different directions and how the response changes due to variations in thickness and compactness over the ice season. Earlier investigations of ice drift in the Baltic have been based on surface drifters and SAR satellite data during relatively short periods (Leppäranta, 1998; Uotila, 2001). Another aim is to obtain an estimate of the ice thickness distribution with focus on the amount of very thick ice in the form of pressure ridges. Sampling the ice thickness from a fixed position may give observations representing a long horizontal distance when the ice cover is moving. Ice motion in combination with thickness measurements from the ADCP gives a quantitative measure of the ice thickness distribution including the ridges. The abundance and thickness of ridges are important

*Corresponding author.
e-mail: gobj@oce.gu.se
DOI: 10.1111/j.1600-0870.2007.00282.x

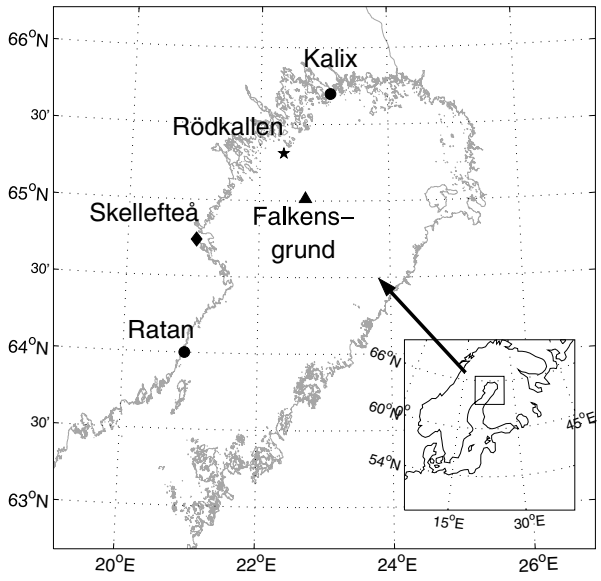

Fig. 1. Map of the Bothnian Bay with positions for the ADCP observations at Falkensgrund (triangle), meteorological observations at Rödkallen (star) and sea level observations at Ratan and Kalix (dots).

quantities for navigational purposes and ridges may also make up a large fraction of the total ice volume. Ridge formation implies a concurrent opening of the ice cover, which can increase total ice production in the basin substantially compared to thermodynamic growth of level ice. Ridges induce form drag that increases the ice water stress significantly and generate turbulence well below the water surface that may increase the overall mixing in the upper water mass. Existing data of sea ice thickness distribution from the Bothnian Bay have been relatively sparse (Jacob and Omstedt, 2005) but resent observations in 2003–2005 using an airborne Electro-Magnetic (EM) sensor has increased the amount of data significantly (EU project IRIS, 2003).

Ice charts where ice types are localized and categorized, including level ice thickness, are published regularly from the Baltic Sea and Bothnian Bay (see e.g. Swedish Meteorological and Hydrological Institute SMHI, www.smhi.se). These charts are based on satellite and mercantile vessel observations and gives therefore limited quantitative information of ice ridges (see Figs. 8–10 for examples).

The Bothnian Bay is the northernmost basin of the Baltic Sea, see map in Fig. 1. The length of the basin is 315 km, the maximal width is 180 km, and the surface area is about 36 500 km^2. The maximum depth is 120 m with a mean depth of 43 m. There is a permanent halocline at about 40 m depth, but the haline stratification is rather weak. The tides are negligibly small in Bothnian Bay due to the narrow straits towards the ocean, but sea level variations due to other processes (mainly wind forcing and air pressure variations) can be quite large with typical amplitudes in the range 0.3–0.5 m (Samuelsson and Stigebrandt, 1996) (see also Fig. 3).

Winters are severe enough to cause sea ice formation in the Bothnian Bay every year. Mean ice thickness varies depending of the severity of the winter, but typically level ice becomes 50–120 cm thick (Leppäranta and Omstedt, 1999). Ice formation generally starts in the shallow coastal areas in the north and thereafter it spreads into the inner parts. Fast ice is usually found landward of the 10 m isobath (see Granskog et al., 2006 for a review of Baltic Sea ice properties). The Bothnian Bay is large enough for the wind forcing to overcome the ice strength and the ice cover deforms therefore during strong wind events and pressure ridges are formed (Leppäranta, 1981; Uotila, 2001). Pressure ridges are typically 5–15 m to a maximum of about 30 m (Leppäranta and Hakala, 1992). The wind is generally rather uniform over the basin since it's size is relatively small compared to the typical scale of atmospheric low pressure systems. Hence, pressure ridges are primarily formed on the windward side of the basin and leads are formed at the upwind side. Thin young ice is formed rapidly in the leads during cold winter conditions.

2. Observations and data processing

An upward looking ADCP was deployed on the sea floor at 21 m depth on the Falkensgrund (N 65°00.80′, E 22°42.48′, see map in Fig. 1). The deployment site was selected in order to be shallow enough to give a distinct echo from the ice but deep enough to avoid the keels of passing ice ridges. The large distance to the shore kept the instrument well outside the fast ice zone.

The instrument, a RDI 600 kHz ADCP, stored ensembles of measurements every 10 min, each consisting of 160 water track pings and 40 bottom track pings. The beam angle is 30° and the beam width for each beam is 3° giving a footprint with a diameter of about 1.2 m for each beam and total footprint area of about 23 m including all beams. A 1 m vertical bin size was used, resulting in an error standard deviation of 1.8 cm s^{-1} for the water velocity. The bottom track measurement was used to detect ice velocity and has an error standard deviation of about 1 cm s^{-1}. The zero velocity offset is typically 0.5 cm s^{-1} for this type of instrument.

Wind and air temperature observations are from the meteorological station Rödkallen, see Fig. 1). The atmospheric data are given every 3 h and were interpolated in time to fit the ADCP data set.

The ice draft can be estimated using the distance between the ADCP and the depth cell with maximum echo intensity. The bin size of the ADCP is 1 m, but it is possible to increase the resolution to about 0.1 m by fitting a modified Gaussian curve to the vertical echo intensity distribution (Shcherbina et al., 2004). The maximum point of the Gaussian curve was then used to determine the distance from the instrument to the lower ice surface. This method was applied on the echo intensity distribution for each of the four beams giving four time-series of distance data. These time-series was then transformed using empirical

orthogonal functions EOF in order to quantify the covariance between the four beams. The time-series of the first orthogonal mode was finally used as a measure of the distance from the instrument to the lower ice surface.

This distance is not only dependent on the ice draft but also on the sea level. The actual ice draft was determined by subtracting the observed sea level. Sea level observations from coastal mareograph stations at Ratan and Kalix where used (see Fig. 1). The average of these two stations was used to represent the sea level at Falkensgrund. The sea level measurement frequency is 1 h and these data were also interpolated to fit the ADCP data set.

It turned out to be quite straightforward to determine whether there is open water or ice above the instrument since open water results in enhanced variance of the error velocity, which is a measure of the difference in vertical velocity between the four beams. Wave motions in open water gives different vertical motion for each beam and therefore large error velocity. In the present data set it was found that open water increases the variance of the error velocity with a factor 3. Similar results was obtained in a study using ADCP from the Gulf of St. Lawrence (Belliveau et al., 1990).

3. Results

The first ice was observed at Falkensgrund on January 16, 2004. Thereafter a persistent ice cover was observed until the ice broke up at May 8, except for a brief period between Jan. 24–28. The three full calendar months (February–April) with ice observations is used in the subsequent analysis.

Time-series of air temperature, wind, ice velocity and water velocity are shown in Fig. 2. The temperature was generally well below zero until mid-April, when it became less variable and systematically above 0°C. The winds were generally moderate with just a few occasions with speed above 10 m s^{-1} and there was a clear correlation between southerly winds and high air temperature and vice versa. Significant ice movements occurred in events with high velocities correlated with strong wind velocities and nearly motionless periods in-between. The maximum ice speed recorded was about 50 cm s^{-1}. Currents 2 m below the ice had generally similar direction as the ice motion, but current speeds were lower indicating that the dominating forcing on the ice cover came from the atmosphere rather than from the sea, as will be discussed further below.

3.1. Ice thickness distribution

The time-series of ice draft computed from echo intensity and adjusted for sea level variations is shown in Fig. 3a and sea level variations at Ratan and Kalix in Fig. 3b. Ice draft of more than 1 m occurred frequently representing pressure ridges passing over the instrument. The maximum draft obtained by this method is about 7 m. It should be noted that the amount of thick ice is artificially exaggerated in this plot since many peaks are merged together by the relatively coarse plot resolution. Figure 3c gives an example with much higher temporal resolution of the echo intensity, ice velocity and the estimated ice draft during a 4-d period. This period started with near zero ice motion (red curve) and nearly constant ice thickness (seen as a very regular and distinct maximum of the echo intensity). The ice started to move on the evening March 26 and numerous ridge-like structures passed the instrument during the late evening and the following day. These appear as a downward displacement of the maximum echo intensity, which is used to determine the ice draft. The ice draft is shown by the white curve.

Although the echo intensity shows a very clear signature of pressure ridges, this method to obtain ice draft is not without problems. The main difficulty is that the echo intensity data are

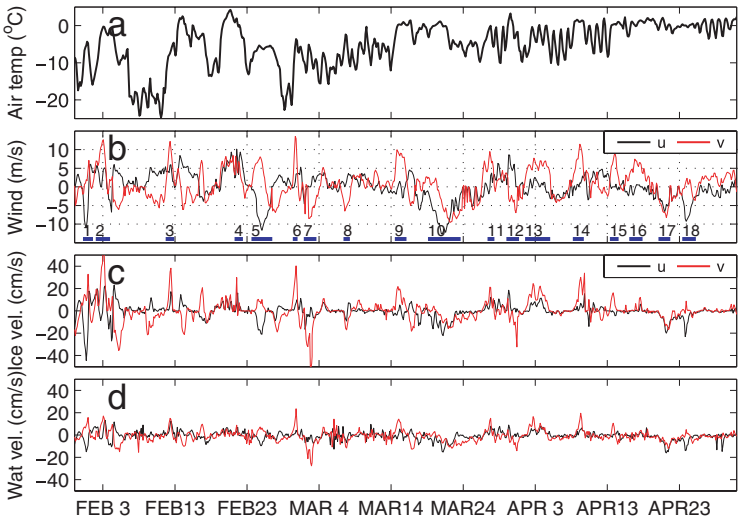

Fig. 2. Overview of the meteorological observations and ADCP measurements during the ice season 2004. (a) Air temperature at Rödkallen. (b) Wind speed components at Rödkallen in geophysical coordinates (u is positive eastward, v is positive northward). The same coordinates are used in the (c) and (d) panels. The thick blue line segments indicates events with wind speed above 5 m s^{-1} that are analysed separately in Figs. 5, 8, 9 and 10. (c) Ice velocity components from Falkensgrund (3 h means) based on bottom track data from the ADCP. (d) Water velocity components (3 h means) at a distance approximately 2 m below the ice based on ADCP data from the water column.

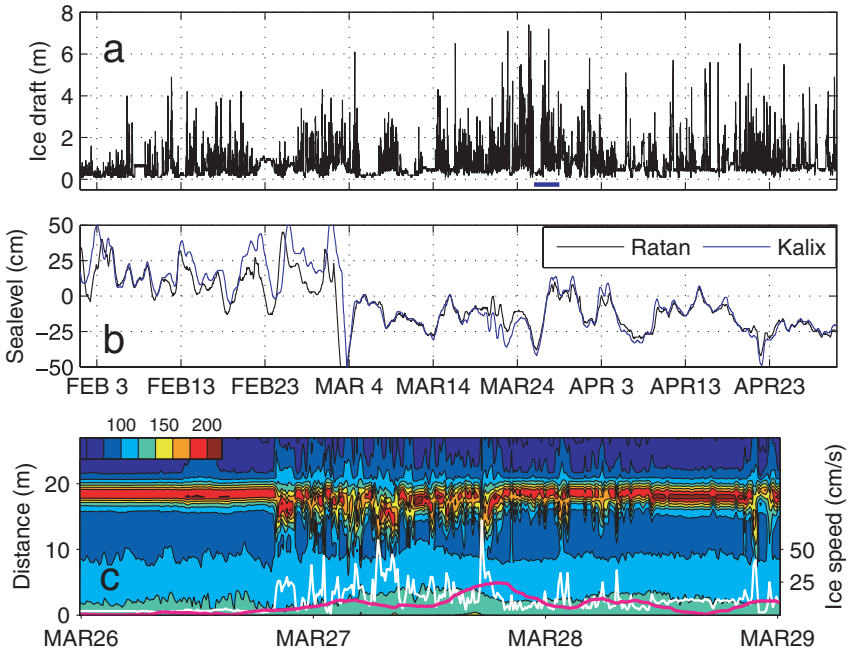

Fig. 3. (a) Ice draft based on ADCP data. The distance from the instrument to the bottom ice surface is determined by fitting a Gaussian curve around the ADCP grid cells containing the maximum echo intensity (see also panel c and method section). The ice draft is then determined by subtracting this distance from the total distance to the sea surface (including sea level variations). The sea level at the observation site is defined as the mean value between the sea level observations at Ratan and Kalix. (b) Sea level observations at Ratan and Kalix. (c) Magnification of a short period (indicated by the thick line segment in panel a) of the ADCP observations. The colour contours show echo intensity as a function of vertical distance from the instrument in decibels (the colour scale is shown in the upper left corner). Also shown is 2× ice draft (white curve) referred to the left *y*-axis, and the ice speed (thick red curve) referred to the right *y*-axis.

averaged over a sampling interval of 10 min. The actual ice draft can vary considerably during the sampling interval and small scale structures during periods with high ice speed are not resolved. An ice speed of 20 cm s^{-1}, for example, corresponds to a measurement cell with a length of 120 m. It can be assumed that many pressure ridges have a smaller horizontal length scale, and such ridges will therefore not be sampled properly. A pressure ridge of smaller scale than the measurement cell will still be seen in the average echo intensity as enhanced values over a number of depth cells (instrument bins) below the level ice surface, where the number of affected cells depends on the ridge thickness. It is however not certain that the position of the maximum echo intensity is affected to the same degree. It is likely that the average maximum echo intensity will be at nearly the same position as for the level ice. Using the maximum echo intensity will therefore sometimes underestimate the ice draft. Another potential problem with the present method is that it might be large differences of the ice draft obtained from the individual beams. This can make it difficult to determine a true draft based on all beams. The first empirical mode based on draft data from the four beams explains however about 87% of the total variance. This shows that individual beam data covaries to a high degree and occasions with large draft differences between beams are rare. The deviation of sea level between the stations is at most about 20 cm as seen in Fig. 3b. The deviation is much less during most of the time and we estimate that the typical error in sea level at Falkensgrund is less than 10 cm.

When observing the ice thickness distribution at a fixed point there is a risk of measuring the same portion of the ice cover passing back and forth above the instrument. That would result in an observed ice thickness distribution that is not representative for a larger area. However, in the Bothnian Bay where the ice seems to move in long trajectories, typically 10–30 km (see Fig. 5), the probability is very low that the same portion of the ice cover will return to the observation point.

The ice thickness distribution is computed using the ice thickness weighted by the length of the measurement cell for each ensemble. The length of the measurement cell is ice speed (3 h moving average) multiplied with the sampling interval (10 min). The ice thickness distribution for each month and for the entire period is shown in Fig. 4. We judge it not relevant to have a finer resolution than 1 m in the thickness increment since the ice thickness obtained by the present method is relatively uncertain. We expect that the error is less than ±0.3 m for level ice but as noted above the error can be larger, and systematically underestimate the ice draft for thick structures with small horizontal scale and passing at high speed.

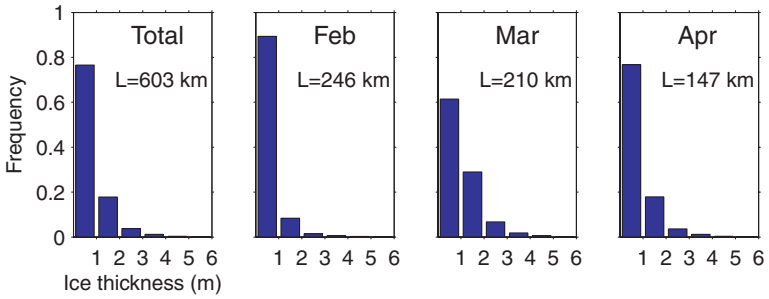

Fig. 4. Total thickness based on ice draft distribution for the entire period (February–April) and distribution for each month. The observations are weighted by the length of each measurement cell defined as the ice speed (3 h moving average) multiplied with the sampling interval (10 min). The distribution is normalized by the total observed track length, L, for each period. L is the sum of the length of the measurement cells.

Table 1. Ice thickness based on ice draft statistics for different months and for the entire period based on ADCP echo intensity data. The mean ice thickness Hm is defined as $Hm = \frac{1}{L}\sum_{i=1}^{n} d_i H_i$, where H_i is the ice thickness for each observation and d_i is the length of each measurement cell, defined as the observed ice speed (3 h mean) multiplied with the sampling interval (10 min). L is the total length of the observation track $L = \sum_{i=1}^{n} d_i$. The volume fraction of ridges VR is defined as $VR = \frac{1}{LHm}\sum_{i=1}^{n} d_i H_i (H_i > 1m)$

	February	March	April	Total
Hm (Mean ice thickness) (m)	0.43	0.99	0.77	0.73
VR (Ridge volume fraction)	0.32	0.61	0.45	0.49

Most of the ice was thinner than 1 m, as expected in this area where the level ice rarely becomes thicker than 1 m. The thinnest fraction occupied about 90% in February, 60% in March and 78% in April. Ice thicker than 1 m represents pressure ridges and there were thus 10% of ridges in February, 40% in March and 22% in April (see also Table 1). The ridges constituted a large proportion of the total ice volume as seen in the table. The results suggest that between 30 and 60% of the ice volume in the central Bothnian Bay consists of ridges at least during this particular ice season. This data set represents a total observed track with a length of 600 km which is about two to three times the size of the basin and should thus give a fairly representative ice statistics for the central part of the bay.

3.2. *Ice dynamics*

The Bothnian Bay is large enough so the accumulated wind force across the basin can overcome the ice strength during most circumstances and the ice will move even if the basin is completely ice covered. However, during extremely cold winters with very thick level ice (>0.5 m), the ice cover may become nearly stationary (Haapala and Leppäranta, 1996). The 2004 season was rather mild so the ice cover was mobile during the entire winter.

The ice was nearly stationary for wind speeds less than about 5 m s^{-1} (Fig. 2) but there was still some motion during most of the time. The ice cover could be defined as stationary for only about 3% of the observations having a speed less than 0.5 cm s^{-1} which is the threshold of the instrument. The ice speed was small, <10 cm s^{-1}, for about 70% of the observations. The high speed part of the record, with speed >10 cm s^{-1}, was characterized by relatively well defined events with maximum speeds between 20 and 50 cm s^{-1}. These high speed events represent a major part (about 70%) of the total drifting distance of the ice (defined as the ice speed times the sampling period and summed over all observations). It is therefore relevant to analyse the direct dynamic response of the ice to wind forcing event by event. We found 18 events during the winter season with wind stronger than 5 m s^{-1}. These are indicated in Fig. 2b. Figure 5 shows progressive vector diagrams of ice and wind for these events. The wind vector has been scaled with a factor of 0.03, which is a typical ice/wind speed ratio. This ratio may actually vary between 0.02 and 0.035 depending on the ice roughness where the low value represents a deformed ice cover with frequent pressure ridges and the high value a smooth ice surface (Leppäranta, 2005). It should be noted that effect of the coriolis force on the free drift speed and turning angle is negligible for the present relatively thin ice cover having a Rossby number (coriolis force/water drag force) typically less than 0.1.

Extensive ice motion occurred in all events throughout ice season. Typical translations were 10–30 km during the events corresponding to 5–20% of the basin scale (about 150 km). Since the basin was almost completely ice covered during the entire winter each event must have caused substantial ice deformation and ridge building.

Event 1 was the only one with free drifting ice, i.e., without any significant internal ice stresses or influence of water motions. The ice and wind trajectories have nearly the same length and the ice moved at an angle to the right of the wind vector. The trajectories are also of similar length in event 2, but the ice moved to the left of the wind vector. During this event, the ice motion was significantly affected by a strong barotropic oscillation in the ocean with an amplitude of about 20 cm s^{-1}. The oscillation is barely seen in Fig. 2 but is a dominant feature in the entire water column data. Internal ice stresses dominated later on during the season causing ice trajectories to be shorter than free drift scaled wind trajectories. There was one event at the end of the ice season (in April, event 16) when the ice moved only

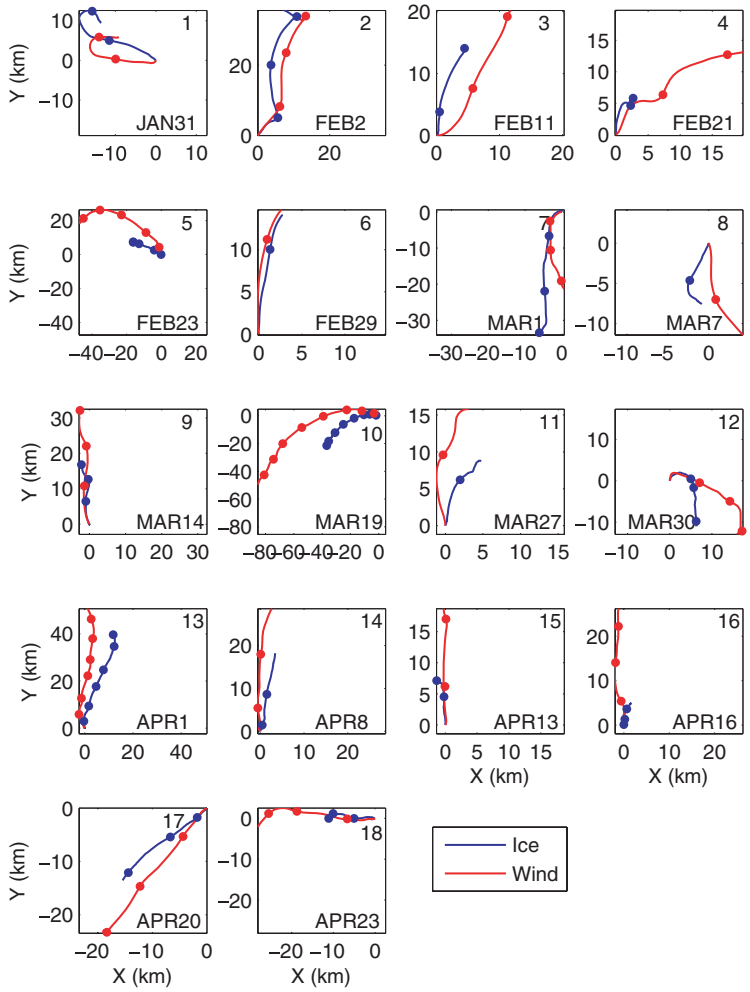

Fig. 5. Wind and ice trajectories for events with wind speed larger than 5 m s^{-1} (see Fig. 2 for time period of each event). The wind components has been multiplied by a factor 0.03 so that equal length of the trajectories would roughly represent free drift. Event number (top) and start date (bottom) for each event are also shown. The elapsed time along each trajectory is roughly indicated by a dot every 12 h.

about 5 km compared to about 25 km for free drift. This event was the last of four events with southerly winds that packed the ice towards the northern part of the bay and thereby enhanced the strength against deformation. There is a general tendency that the ice is more mobile in events characterized by a large directional shift of the wind compared to the previous event. This is especially clear when comparing event 16 and 17. When the northeasterly wind started in April 20, it occurred after a long period of southerly wind and the ice moved easily in the new (reversed) wind direction. Ice charts (not shown) confirmed that the period of southerly winds formed a large open area in the southeastern part of the bay, which made it easy for the ice to move in that direction.

An overview of how the ice speed responds to wind forcing can be obtained from a two-dimensional frequency plot of wind and ice speed. Such plots are shown in Fig. 6 for each month and are based on 3-h mean ice and wind speeds. For an ice cover in free drift all data would be concentrated along a line with a slope related to the ice/wind speed ratio (a line with 3% slope is indicated in the figures). This is not the case for the observations from Bothnian Bay where the data is very much spread over the wind/ice speed plane. There is a weak tendency to a concentration of data around the free drift line in February but most of the observations fall below the free drift line indicating a large influence of internal stresses. There are also some observations with faster ice motion than 3% of the wind speed, probably due to influence of ocean currents acting in the wind direction. The ice speed was generally reduced in March with few observations higher than 25 cm s^{-1} and a larger dominance of data points below the free drift line. The was also significantly more observations with ice speed less than 5 cm s^{-1}. The winds were generally weaker in April with just two occasions above 10 m s^{-1}, but there is still a clear tendency that the ice cover was much less mobile than earlier in the season with many more observations with ice speed below 5 cm s^{-1}. There were, for example, 110 occasions (corresponding to about 14 d) in the wind speed range 2–5 m s^{-1} having ice speed less than 5 cm s^{-1}. The ice cover was thus nearly stationary for low wind speeds. It should also be noticed that even though the ice cover was nearly stationary for most of the time, there were still events when it

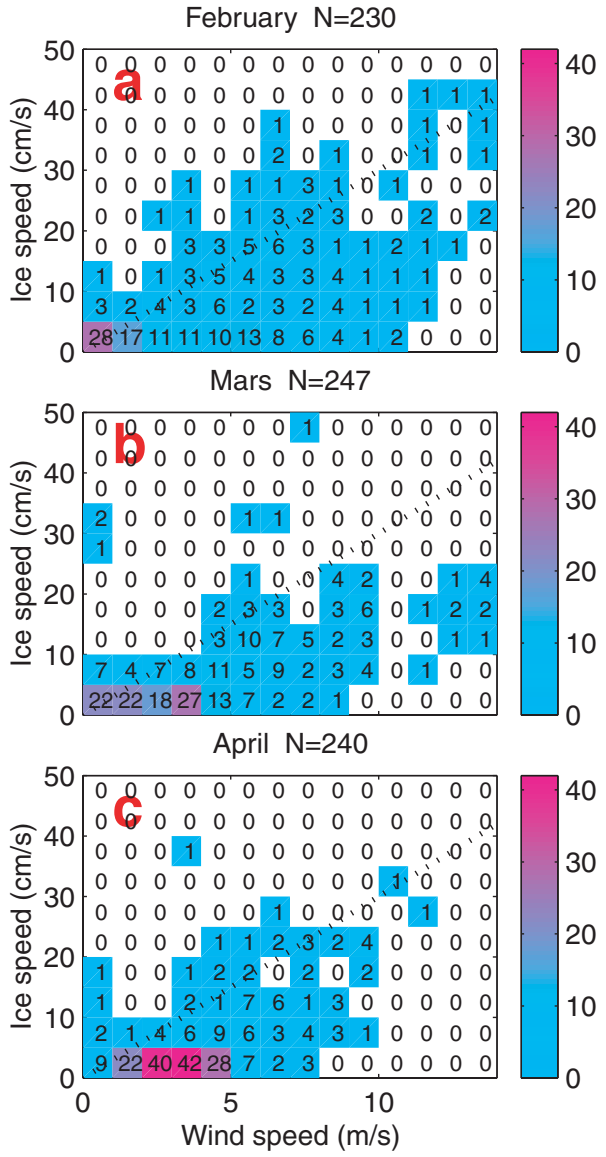

Fig. 6. Two-dimensional frequency plot of wind and ice speed for each month based on 3 h mean ice speeds. (a) February, (b) March and (c) April. The wind and ice speed is divided into 1 m s^{-1} and 5 cm s^{-1} bins, respectively. The dotted line indicates roughly the free drift relation when the ice velocity is 3% of the wind speed. The number of occurrences in each bin is given both by numbers and a colour scale. The total number of occurrences (3 h means) N for each month are also given.

moved in near free drift. This is likely due to areas of thin new ice or open water that usually are formed close to the coast. The ice can easily move towards such areas if the wind direction is favourable.

The percentage of observations with nearly stationary ice cover (ice velocity <5 cm s^{-1}) for different wind speed intervals is summarized in Table 2 for each month. This gives a measure

Table 2. The percentage of observations with near zero ice motion (0–5 cm s^{-1}) for different wind speed intervals

Month	2–3 m s^{-1}	3–4 m s^{-1}	4–5 m s^{-1}	5–6 m s^{-1}	6–7 m s^{-1}
February	64	50	42	50	30
March	72	77	45	26	9
April	90	80	68	30	14

of how the stiffness of the ice cover (resistance to move with the wind) developed over the season. The percentage of observations with nearly stationary ice cover increased over the season for all three wind speed intervals up to 5 m s^{-1}. The ice was, for example, nearly stationary in 50% of the observations in February in the wind speed interval 3–4 m s^{-1} but in April this occurred for 80% of the cases. However, the ice still moved rather easily for wind speeds above 5 m s^{-1} even in April. The ice speed is then larger than 5 cm s^{-1} in 70% of the observations.

A more objective way to examine the relation between wind forcing and ice motion is to assume a linear dependence between the wind and ice velocity by fitting a linear regression model to the data. The ice/wind relationship is given by: (1).

$$U_{\mathrm{ice}}(t) = R(t)U_{\mathrm{wind}}(t) + Z(t), \tag{1}$$

where all involved quantities are complex numbers. $R(t)$ is the temporally varying complex regression coefficient involving a wind/ice speed ratio and a turning angle. $Z(t)$ contains the portion of the ice motions not explained by the wind forcing. $R(t)$ is computed by minimizing the least-square error between the model and observations over a time window δ_t, that is,

$$R(t) = \frac{\langle U_{\mathrm{ice}} U^*_{\mathrm{wind}} \rangle - \langle U_{\mathrm{ice}} \rangle \langle U^*_{\mathrm{wind}} \rangle}{\langle U_{\mathrm{wind}} U^*_{\mathrm{wind}} \rangle - \langle U_{\mathrm{wind}} \rangle \langle U^*_{\mathrm{wind}} \rangle}, \tag{2}$$

where means are computed as

$$\langle U \rangle = \frac{1}{\delta_t} \int_{t-\delta_t/2}^{t+\delta_t/2} U(\tau)\, \mathrm{d}\tau \tag{3}$$

and the stars denotes complex conjugates. The length of the time window is a trade-off between the possibility to detect changes in the wind/ice relation and to include enough covariability to get a significant regression. A window shorter than 5 d gives a very unstable regression coefficient with large fluctuations indicating that wind forced variability occur on longer timescales. We use a 10-d window that both gives a stable regression and a possibility to see changes in the relationship over the period. The wind/ice speed ratio plot and the associated angle for different months is shown in Fig. 7a. The speed ratio was around 3% in the beginning of February, decreased to just above 1% in the middle of the month and went back up to 3% at the end of February and early March. The ratio was relatively low, between 1–2%, during the rest of the period. The rapid decrease of the speed ratio in the first part of the period shows that ice stresses became dominant rather quickly, presumably as a result of the increasing new ice

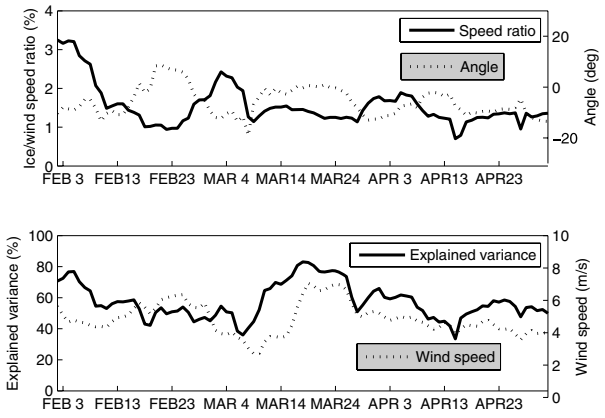

Fig. 7. (a) Ice/wind speed ratio and turning angle based on a linear regression model (eq. 1) using a 10 d time window. The time window is incremented by 1 d. (b) Explained variance and average wind speed over each 10 d window.

thickness. The enhanced speed ratio during some periods, as in late February, can be explained by shifts in the general wind direction. The event in late February was the first occasion of northerly winds after a period of mostly southerly and easterly winds (see Fig. 5) and it was then easy for the ice to move towards thinner ice in the south. There is no tendency that the ice becomes more mobile just before it disappears in early May which is somewhat unexpected because large amounts of open water are normally associated with the break-up which should increase the mobility. The break-up period was however dominated by southerly winds that hold the remaining ice cover in the northern part of the bay.

The turning angle was generally negative meaning that the ice moved to the right of the wind direction. It was about -10° at the beginning of the period, which is less than typically -30° that would be expected in free drift (Thorndike and Colony, 1982) indicating some influence of ice stresses already for the initially thin ice cover. There was also a relatively long period in the middle of the record with near zero angle, again showing the influence of the internal stress. The explained variance, that is how much of the variance of the ice motion that is explained by the linear model for each time window, was high, about 80%, in the beginning of the record and in March. Between these periods the explained variance was relatively low (40–60%) showing a less direct relation between ice and wind velocity. The explained variance is somewhat dependent on the wind speed with higher values for higher wind speeds which is natural since one should expect a clearer wind dependence for strong winds when the wind force can overcome the internal stress.

The observations can be examined in terms of force balance in order to acquire quantitative information on the partitioning between air stress, water stress and internal ice stress. We examine three characteristic events in more detail: One event in near free drift (event 1), one relatively short event with significant ice stress (event 5) and a long event dominated by ice stress (event 10).

The force balance neglecting the acceleration, coriolis and sea surface tilt terms is given by

$$\tau_{\mathbf{i}} + \tau_{\mathbf{a}} + \tau_{\mathbf{w}} = 0, \tag{4}$$

where $\tau_{\mathbf{a}}$ is the air stress, $\tau_{\mathbf{w}}$ water stress and $\tau_{\mathbf{i}}$ internal ice stress. $\tau_{\mathbf{a}}$ and $\tau_{\mathbf{w}}$ can be computed from data while $\tau_{\mathbf{i}}$ is given as the difference vector. The air and water stress are computed according to:

$$\tau_{\mathbf{a}} = \rho_a C_a |\mathbf{U_w}| \mathbf{U_w} \tag{5}$$

$$\tau_{\mathbf{w}} = \rho_w C_w |\mathbf{U_2} - \mathbf{U_i}| (\mathbf{U_2} - \mathbf{U_i}), \tag{6}$$

where $\mathbf{U_w}$ is the wind velocity, $\mathbf{U_i}$ ice velocity, and $\mathbf{U_2}$ water velocity 2 m below the ice. Stresses and velocities are all vector quantities. ρ_a and ρ_w are the air and water density, respectively ($\rho_a = 1.3$ kg m^{-3}, $\rho_w = 1000$ kg m^{-3}). The air drag coefficient Ca $= 1.5 \times 10^{-3}$ is based on 10 m wind speed observations from Joffre (1982). The ice/water drag coefficient C_w is estimated from the ADCP water velocity data 2 m below the ice, U_2. A value $C_w = 3.0 \times 10^{-3}$ was found to give a realistic force balance during free drift. We use a drag coefficient based on ocean velocities relatively near the ice in order to obtain a direct connection between the ice–water velocity difference and the surface stress. The 2-m distance below the ice is chosen in order to be as close as possible to the ice but still having ADCP data from the water column that is free from disturbances by the strong echo from the bottom surface of the ice (ADCP data from the depth cell closest to a strong reflector tends always to be corrupted). Another possibility is to use current velocity well below the turbulent upper boundary layer, which is usually referred to as the free geostrophic velocity. In that case one needs also to incorporate a turning angle between the geostrophic current and the surface stress. Effects of stratification needs then probably also to be taken into account.

Event 1 occurred early in the season when the ice was thin (5–20 cm according to the ice chart) and the ice cover should therefore primarily be in free drift and the force balance should be dominated by air stress and ice–water stress. Fig. 8 shows the ice speed and force balance during event 1. The chosen value of C_w gives an ice/water stress that matches the air stress relatively well over most of the period. The length of the difference vector $\boldsymbol{\tau}_{\mathbf{i}}$ (which can interpreted as internal ice stress) is also much smaller than the two other stresses. It should be noted that the ice/wind speed factor is well above 0.03 during a larger part of the event (Fig. 7a), which is higher than other observations during free drift conditions. Leppäranta and Omstedt (1990) report a factor 0.02 during a 7 d experiment in April. It is likely that the present event, early in the season, is characterized by relatively smooth ice surface with relatively few ridges giving a low water stress that in turn brings up the ice wind factor compared to the April observations with more ridges.

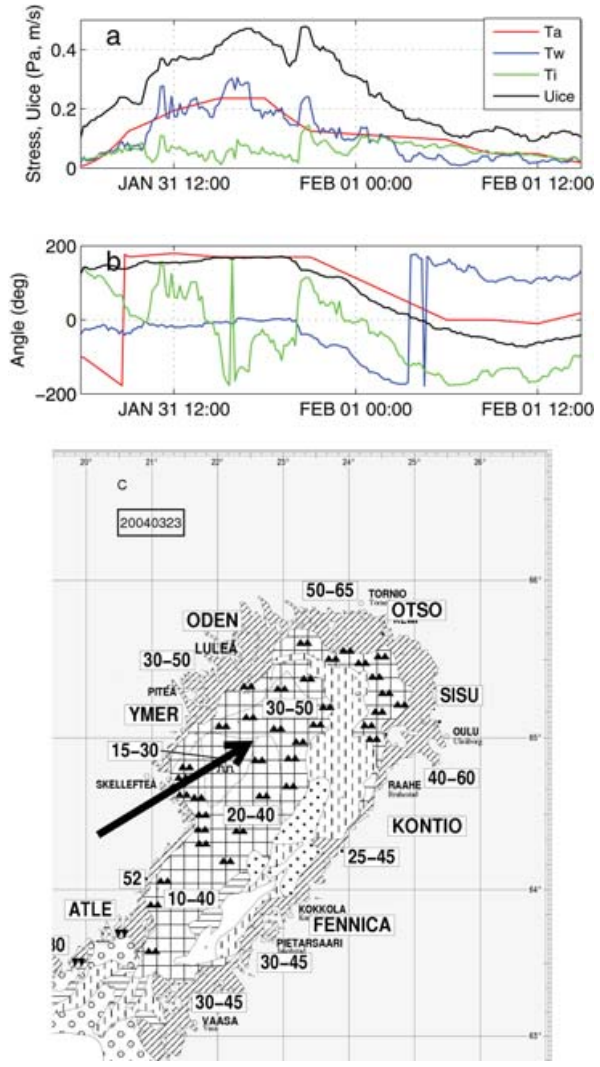

Fig. 8. Stress vectors and ice velocity vector during the period 01/31–02/01 (event 1 in Fig. 2). The (a) panel shows magnitudes and the (b) panel the angle in the geophysical coordinate system (90° represents a vector pointing in the northward direction). Ta is the air stress, Tw is the water stress, Ti is the internal stress and Uice is the ice velocity. All time-series are low-pass filtered by a 1 h moving median filter. Panel (c) shows ice chart from February 2, reproduced with permission by the Swedish Meteorological and Hydrological Institute (SMHI). The numbers within squares are ice thickness in cm and the arrow shows the position for the ADCP measurements. Symbols for ice-types are defined as: Checked pattern denotes consolidated, compact ice (9–10/10); horizontal hatching close ice (7–10/10); vertical bars open ice (4–6/10); circles very open ice (1–3/10); stars new ice; dots open water; inclined hatching fast ice; and triangles denote pressure ridges.

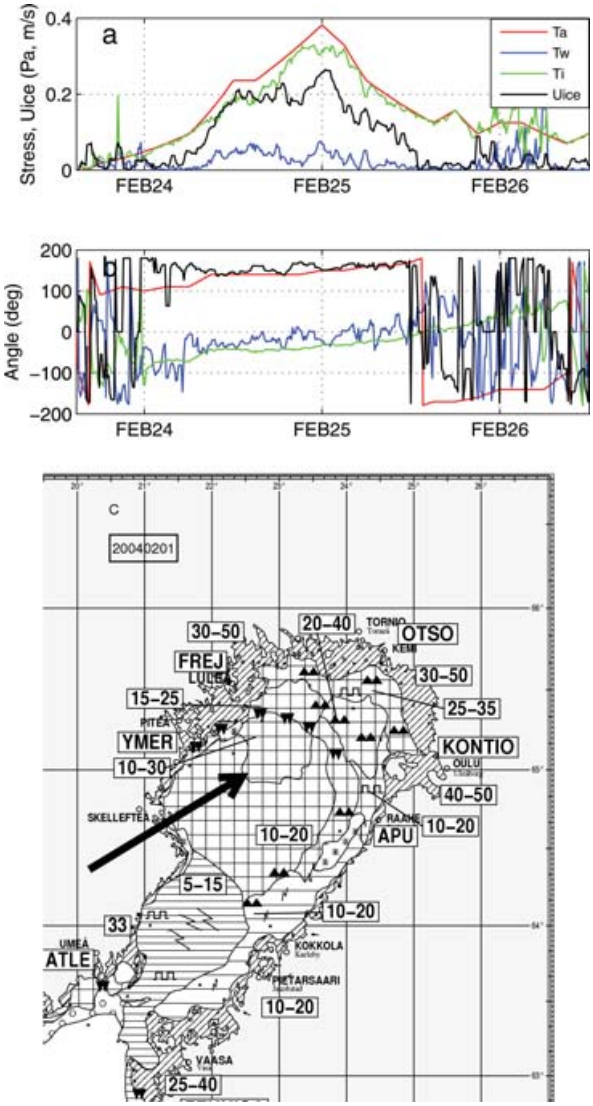

Fig. 9. Same as Fig. 8, but for the period 02/24–02/26 (event 5 in Fig. 2.)

The next event (no 5) is characterized by significant ice stresses (Fig. 9). The ice thickness according to the ice charts was 15–40 cm over a large part of the basin. The wind direction was from southeast in the beginning of the event and turned gradually towards east and northeast. The ice started to move significantly when the air stress exceeded 0.1 Pa and the speed increased until it levelled off at about 0.2 m s^{-1} in spite of continued increased air stress. $|\boldsymbol{\tau}_\mathbf{w}|$ was much smaller than $|\boldsymbol{\tau}_\mathbf{a}|$ during the event showing the dominance of internal ice stress. This is an example of strain hardening such that the internal ice force increases as the ice becomes compacted. There was a second peak in ice velocity, possibly due to the change in wind direction exposing a somewhat weaker part of the ice cover to the air stress. The ice stopped moving at around 0.15 Pa air stress while it started to move at a much lower stress level (∼0.08 Pa).

Event no 10 (Fig. 10) is an example of a longer wind event when the wind direction slowly shifted from easterly to northeasterly. The effect of successive strain hardening can be seen during this event such that the ice became stronger the more it was compacted. The ice started to move easily for air stress at about 0.1 Pa but the internal ice stress built up rapidly and

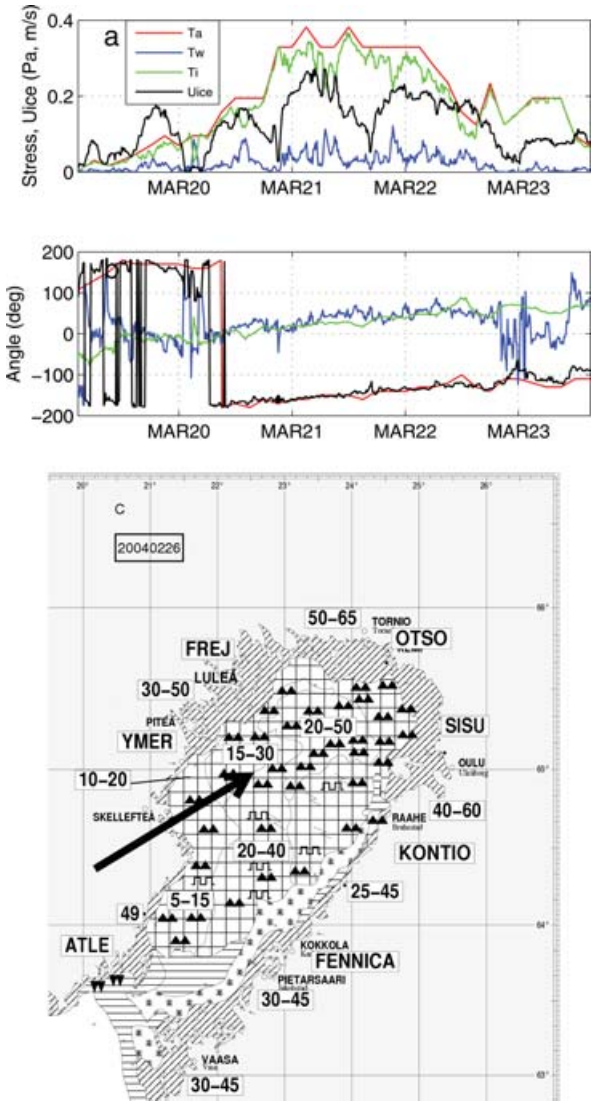

Fig. 10. Same as Fig. 8, but for the period 03/20–03/23 (event 10 in Fig. 2.)

stopped the motion. When the air stress later on increased to about 0.2 Pa it overcame the ice strength and the ice started to move, reached a maximum, and stopped again due to increased internal stress. The same pattern repeated on the third day when the air stress increased to >0.3 Pa with an associated peak in ice velocity. A second peak in the ice velocity occurred during this relatively long period of high and relatively constant air stress. This was probably due to slightly changing wind direction towards more northerly so that a weaker part of the ice cover became involved in taking up the wind load. It is possible that the peninsula southeast of Skellefteå (Fig. 1) no longer posed an obstacle when wind shifted and the ice could pass more freely in the southward direction.

It is possible to obtain a rough estimate of the compressive ice strength from the internal ice stress and the wind fetch over the basin. The maximum ice stress during event 10 with near zero velocity was about 0.3 Pa which multiplied with a fetch of about 150 km gives a force of $4.5 \times 10^4\,\mathrm{N\,m^{-1}}$. In order to obtain an ice strength this should be divided with an ice thickness, which is rather uncertain, but using 50 cm which was the maximum level ice thickness in the area according to the ice chart gives an ice strength of $9 \times 10^4\,\mathrm{N\,m^{-2}}$. This is actually much larger than the $2.5 \times 10^4\,\mathrm{N\,m^{-2}}$ that has been used as a working standard in ice models of the Baltic (Leppäranta et al., 1998). This difference by a factor of three is somewhat surprising since 50 cm should be about the thickest level ice present in the basin during this season. If thinner ice had to take up the wind load the difference would have been even larger. Another possibility is that the ice cover was heavily ridged in the area for maximal ice stress so that the effective load up-taking thickness was larger than 50 cm. It should be mentioned that higher values of the yield strength, up to 100 kPa, have been obtained by comparing surface elevation data for open water and compact ice (Zhang and Leppäranta, 1995).

4. Discussion

The single fixed instrument in the central part of the basin provides some basic information of the dynamic response of the ice cover to wind forcing, but it gives certainly not the full picture. It is well known that the motion field varies in space it is an open question over how large area this single point measurement gives a representative measure of the ice motion. Drifter data shows, for example, that the ice motion becomes more aligned along the coastline in the shear zone close to the coast (Uotila, 2001). It would be interesting to have observations at several locations in order to quantify spatial variations of the ice motion. Spatial information can already be obtained from drifting buoy data (Uotila, 2001) and pattern following systems based on satellite pictures (Leppäranta et al., 1998). An advantage with fixed instruments below the ice is that currents and ice thickness can be measured simultaneously with ice velocity. Fixed point observations also provide high time-resolution data compared to satellite products and a better control of the observation location compared to drifting buoys which will be transported over long distances.

The ice draft derived from the ADCP is probably underestimated especially for small scale structures and high ice speeds primarily due to the 10 min long averaging period of the ADCP data. It is hard to estimate how large this error is without comparing simultaneous ADCP data with, for example, data from an upward looking sonar with much higher sampling frequency. Other investigations based on drilling Leppäranta and Hakala (1992) and EM data from the extensive IRIS field champagne on eastern Bothnian Bay 2004 show that ridges thicker than 5 m are relatively frequent. One aspect in favour of reducing the error with the present method is that structures giving an enhanced echo intensity well below the level ice surface and no associated change of the position for the maximum echo intensity are rare in the present record. The short period shown in

Fig. 3c is in fact representative for the entire observational record. This means that ridges are always detected but the maximum thickness for an individual ridge might still be underestimated. It is therefore likely that the amount of ridges ice >1 m in the obtained thickness distribution is realistic.

The present study has some implications on ice models for the Baltic and likely also for other semi-sized basins with perennial ice cover such as the Great lakes, the White Sea and the Hudson Bay. With semi-sized is meant here that the basin is large enough to have moving ice but small enough so that the atmospheric forcing is nearly uniform. A characteristic feature for the Bothnian Bay is the formation of open water and new ice at the leeward coast. The size of this area is a critical quantity to reproduce by ice models. It is important to describe the opening area correctly since it will be the place for large production of new ice and it will also represent a build-in weakness of the ice cover for winds in the opposite direction. If the size of new ice area is reasonable correct one can also expect the rheology of the ice model, including the parameters such as the ice strength, to work properly. Areas of new ice and open water along the coast are relatively easily identified in satellite pictures and from detailed ice charts and should therefore be practical to use for model verification purposes.

5. Conclusions

ADCP observations at Falkensgrund during the ice season 2004 showed that:

Pressure ridges, defined as ice thicker than 1 m, occupied 10% of the ice cover in February, 40% in March and 22% in April, and the estimated ridged ice contribution to the total volume was 30–60%.

The ice speed was small ($<10\,\mathrm{cm\,s^{-1}}$) for most of the time (70%) and stationary ($<0.5\,\mathrm{cm\,s^{-1}}$) for only 3% of the time. High speeds ($20–50\,\mathrm{cm\,s^{-1}}$) occurred in relatively well defined events. These events make up a major part (70%) of the total drift distance.

The wind/ice speed ratio was about 3% for the initial thin ice cover in early February, and the ratio was significantly lower (1–2%) during the rest of the season.

There is a general tendency that the ice is more mobile in events characterized by a large shift in wind direction.

A rough estimate, based on wind fetch and motion data, gives a compressive ice strength of $9 \times 10^4\,\mathrm{N\,m^{-2}}$, which is more than three times larger than the $2.5 \times 10^4\,\mathrm{N\,m^{-2}}$ regularly used in dynamic ice models.

6. Acknowledgments

We thank Dr. Bength Liljebladh for technical support regarding instrument configuration and data processing. This is contribution no 7 from, the centre for Earth System Science at Göteborg University (Tellus). The Swedish Meteorological and Hydrological Institute (SMHI) kindly supplied atmospheric and sea level data. Financial support was provided by Umeå Marine Science Centre (UMF) and the Swedish Research Council (VR).

References

Belliveau, D. J., Bugden, G. L., Eid, B. M. and Calnan, C. J. 1990. Sea ice velocity-measurements by upward-looking doppler current profilers. *J. Atmos. Oceanic Technol.* **7**(4), 596–602.

Granskog, M., Kartokallio, H., Kuosa, H, Thomas, D. N. and Vainio, J. 2006. Sea ice in the Baltic Sea—a review. *Estuarine, Coast. Shelf Sci.* **70**, 145–160.

Haapala, J. and Leppäranta, M. 1996. Simulating the Baltic Sea ice season with a coupled ice-ocean model. *Tellus, Ser. A* **48A**, 622–643.

IRIS, 2003. Ice Ridging Information for Decision Making in Shipping Operations. EU project homepage: http://www.tkk.fi/Units/Ship/Research/Iris/Public/

Joffre, S. M., 1982. Momentum and heat transfers in the surface layer over a frozen sea. *Boundary-Layer Met.* **24**(2), 211–229.

Jacob, D. and Omstedt, A. (eds.) 2005. BALTEX PHASE 1: 1993-2002, State of the Art Report. *BALTEX Publication* **No. 31**, 181 pages.

Leppäranta, M. 1981. On the structure and mechanics of pack ice in the Bothnian Bay. *Finnish Mar. Res.* **248**, 3–86.

Leppäranta, M. and Omstedt, A. 1990. Dynamic coupling of sea ice and water for an ice field with free boundaries. *Tellus, Ser. A* **42A**, 482–495.

Leppäranta, M. and Hakala, R. 1992. The structure and strength of first-year ice ridges in the Baltic Sea. *Cold Regions Sci. Technol.* **20**, 295–311.

Leppäranta, M. 1998. The dynamics of sea ice. Lecture notes from a summer school in Savonlinna, Finland 6–17 june 1994. In: *Physics of Ice-Covered Seas*, (ed. Matti Leppäranta). Helsinki University Press, Helsinki, 305–342.

Leppäranta, M., Sun, Y. and Haapala, J. 1998. Comparison of sea ice velocity fields from ERS-1 SAR and dynamic model. *J. Glaciol.* **44**, 248–262.

Leppäranta, M. and Omstedt, A. 1999. A review of ice time series of the Baltic Sea. *Publications Instituti Geographici Universitatis Tartuensis*, **84**, 7–10.

Leppäranta, M. 2005. *The Drift of Sea Ice*. Springer, Helsinki, 266 p.

Omstedt, A., Elken, J., Lehmann, A. and Piechura, J. 2004. Knowledge of the Baltic Sea physics gained during the BALTEX and related programmes. *Prog. Oceanogr.* **63**(1–2), 1–28.

Samuelsson, M. and Stigebrandt, A. 1996. Main characteristics of the long-term sea level variability in the Baltic Sea. *Tellus* **48A**, 672–683.

Shcherbina, A. Y., Rudnick, D. L. and Talley, L. 2005. Ice-draft profiling from bottom-mounted ADCP data. *J. Atmos. Oceanic Technol.* **22**(8), 1249–1266.

Thorndike, A. S. and Colony, R. 1982. Sea ice motion in response to geostrophic wind. *J. Geophys. Res.* **87**(C8), 5845–5852.

Thorndike, A. S., Rothrock, D. A., Maykut, G. A. and Colony, R. 1975. The thickness distribution of sea ice. *J. Geophys. Res.* **80**(33), 4501–4519.

Uotila, J. 2001. Observed and modelled sea-ice drift response to wind forcing in the northern Baltic Sea. *Tellus* **53A**, 112–128.

Zhang, Z. H. and Leppäranta, M. 1995. Modeling the influence of ice on sea level variations in the Baltic Sea. *Geophysica* **31**(2), 31–45.

Paper IV

,
,

A Dynamic Sea Ice Model Based on the Formation Direction of Leads

Christian Nohr[**,a], Göran Björk[a], Bo G. Gustafsson[b]

[a]*Department of Oceanography, Earth Science Center, University of Gothenburg, Box 460, SE-405 30 Göteborg, Sweden*
[b]*Baltic Nest Institute - Stockholm Resilience Center, Stockholm University, SE-106 91 Stockholm, Sweden*

Abstract

A dynamic ice model is presented using a novel approach where the memory of weak directions in the ice cover is stored. The model computes ice motion, ice deformation and the associated dynamic ice production without the need of a full two dimensional computation. The ice dynamics is based on a viscous-plastic approach in a marginal ice zone with both compressive and shear stresses. The method is very computational efficient but is likely restricted to basin scales of semi size with relatively coherent wind forcing over the basin. The model is applied to the Bothnian Bay of the Baltic Sea and coupled with an ocean model. The results show good agreement when compared against measurements of ice velocity from an upward looking ADCP deployed in the center of the Bothnian Bay and observations from ice charts. As a model application, the dynamic ice production that occurs in addition to the pure thermodynamic growth in a deforming ice cover has been computed over the period 1991-2004. The results show that the dynamic ice production typically increases the ice volume with 80% over the simulation period.

Key words: Sea ice, Ice thickness distribution, Ice production, Level ice, Deformed ice

1. Introduction

The most common way to mathematically describe the dynamic properties of sea ice is to use models where the dynamical equations are solved on a two dimensional grid. Although this kind of models can be very successful in describing various ice properties such as ice motion, ice deformation, ice thickness and ice concentration [e.g. Hunke and Dukowicz, 1997, Bitz et al., 2001] they might not be the most suitable tool for all applications. The main reason for this is that two dimensional models are quite computational demanding and generate massive data output including detailed information about horizontal variability which might not harmonize

*Corresponding author.
**Corresponding author.
Email addresses: chno@oce.gu.se (Christian Nohr), gobj@oce.gu.se (Göran Björk), bo.gustafsson@stockholmresilience.su.se (Bo G. Gustafsson)

with other parts of a model system. One example of application where other type of ice models may be needed is physical and biogeochemical model simulations of enclosed or semi-enclosed basins where the water column can be well described by a one-dimensional column model and where a realistic ice sub-model is needed but not necessarily provide with full two dimensional fields. In such applications there is often a need of exploring multi dimensional parameter spaces and compare with data in order to find an optimum parameter combination. Such explorations are very time-consuming with a full two dimensional ice model approach and call for more idealized ice models. Another example is model simulations of enclosed or semi-enclosed basins where the water column can be well described by a one-dimensional column model. The models need a realistic ice sub-model but the simulations are not required to provide full two dimensional ice fields.

In the Baltic Sea modeling community, various horizontally integrated coupled column models have been used for modeling the major oceanic features such as temperature and salinity structure with very satisfying results [e.g. Omstedt and Axell, 2003, Gustafsson, 2003]. One draw-back with several of these models is the lack of a physically correct description of ice dynamics in the ice sub-models. The thermodynamical ice growth is generally well handled, but the description of the ice dynamics is rather primitive. One example is the model by Omstedt and Axell [2003] where the basin surface is partly covered by ice while the rest is open water. The ice and open water are separated by a moving "ice front". If the wind is offshore the front moves in free drift. When the wind is onshore, the ice speed is reduced by internal forces dependent only on the ice strength [Hibler, 1979]. No ridging occurs in the model and the thickness is only thermodynamically controlled. In the model by Gustafsson [2003], the ice cover is separated into a number of categories with unique area coverage fractions, ice thickness, snow thickness and ice temperatures, following Björk [1992]. The ice velocity is dependent on the basin average ice thickness so that the ice moves in free drift below a maximum thickness. For thicker ice the wind speed/ice speed ratio is decreased linearly up to a certain thickness, above which the ice cover becomes immobile. This model has thus not any wind direction dependence on the ice motion. Deformation and ridging is implemented in the model such that the ridging is proportional to the ice speed.

Here we present an alternative way to include a more realistic first order description of the ice motion and ice deformation, in what we call middle-sized basins, without explicitly resolving the two dimensional fields. We define a middle-sized basin to be a basin that is large enough for the wind force to overcome ice strength and generate moving pack ice, but small enough in comparison with weather systems so that the wind forcing is approximately constant over the entire basin surface, i.e. the wind varies in time but not in space. The wind stress will then mainly pack the ice against the windward coast and create an area of open water at the leeward coast. The open water area will freeze over rapidly during the winter, but as long as the new ice is relatively thin, it will remain as a weak part of the ice cover. The leading idea of the model is to utilize that the ice generally moves in a slab like fashion, with relatively small shearing motions, in the central parts of a semi-sized basin like the Baltic Sea [Leppäranta et al., 1998]. In the model, we keep track on the approximate location of where open water and new ice is formed by storing the formation direction. The formation direction can then be utilized to determine the resistance of the ice to move according to subsequent wind forcing from other directions.

The model is applied to the Baltic Sea and coupled to a one dimensional ocean model, but we think that the concept can be used in other areas and other types of applications as well. The computational efficiency open for really long term simulations as well as sensitivity studies over dense multidimensional parameter spaces. The model is described in detail in section 2.

Section 3 gives a comparison between model computed ice velocity and observed velocity at a fixed point. Section 4 gives an example of model application with focus on the dynamical ice production in the Bothnian Bay. The ice model is coupled to an ocean model and the ice cover is simulated over 14 years. The dynamical ice production arises when deformation processes open up leads in which the ice production is much higher than for the surrounding ice. Rapid ice growth in the open water areas can often represent a significant part of the total ice growth. Ice thickness data over a full ice season in the Bothnian Bay show that up to 50 percent of the ice volume may consist of ridged ice [Björk et al., 2008], indicating a significant dynamical ice production, see also a review by Granskog et al. [2006]. The model results are discussed in section 5.

2. Model description

The dynamical properties of the model are described in detail here while the thermodynamic part of the sea ice model and the water circulation model are only described briefly since thorough descriptions are given in Björk [1992] and Gustafsson [2003]. The ice cover is resolved by a number of ice categories where each category occupies a certain fraction of the total basin area and the thickness evolution due to thermodynamic ice growth/melt is computed independently for each category. The model makes use of a viscous-plastic rheology approach in order to determinate the ice stress. Two types of compressive ice strength parameterizations are tested. The first type is the widely used linear relation where the strength increases linearly with the ice thickness [Hibler, 1979] and the second uses a strength that is proportional to the square of the ice thickness as can be derived from energy conservation during ridge building [Rothrock, 1975].

2.1. Definition of ice categories and ice thickness distribution

The ice cover is separated into a number, n, of ice categories $C_i, i = 1, n$. Each category is characterized by five state variables

$$C_i = (a_i, H_i, h_i, T_i, B_i) \tag{1}$$

Where i is the category index, a_i is the fraction of the total area occupied by category i, H_i is the ice thickness, h_i the snow thickness and T_i the ice temperature. Note that the thickness of each category changes continuously according to the thermodynamic forcing. The categories have therefore not a fixed thickness and it is either not associated with any specific thickness interval. The new feature introduced here is a property called formation direction B_i, defined as the direction at which a new category is formed. The exact definition of this variable is given later. The categories are sorted by thickness such that $i = 1$ contains the thinnest ice or open water (if $H_1 = 0$ m). The sum of the fractional areas of the n categories always equal unity

$$\sum_{i=1}^{n} a_i = 1 \tag{2}$$

The area weighted average thickness of the ice cover $\langle \overline{H} \rangle$ is defined as

$$\langle \overline{H} \rangle = \sum_{i=1}^{n} a_i H_i \tag{3}$$

which is the same as the ice volume per unit area. The cumulative ice thickness distribution $G(H_i)$ is defined as

$$G(H_i) = \sum_{j=1}^{i} a_j \tag{4}$$

The categories may consist of level (not deformed) ice or ridged (deformed) ice which is book-kept for diagnostic purpose.

2.2. The model concept

In the following we consider a fully ice covered basin where the ice is set in motion by wind stress. The principal sketch (Fig. 1) shows three stages of a simplified ice cover, including deformation of a weak category (subscript *j*) and thermodynamical ice growth. Initially the ice cover is stationary (Fig. 1a) and includes one thick category and one thin and weak category. The thin category has been given a formation direction B_j towards the left in the figure. When a wind stress is applied (Fig. 1b) from a direction opposite to B_j, the ice cover starts to move. The ice piles up and forms a pressure ridge in a deformation zone at the windward shore of the basin. The deformed thick ice forms a new category (subscript *r*) and is given an associated formation direction. The open water concurrently generated at the leeward side is also introduced as a new category with its associated formation direction (subscript *ow*). The area fraction of open water is dependent on the ice speed, basin dimensions and the length of time step. During the whole deformation process the total ice volume is conserved. After the deformation event, new ice forms in the open water and the rest of the ice cover grows thicker according to the thermodynamic forcing (Fig. 1c).

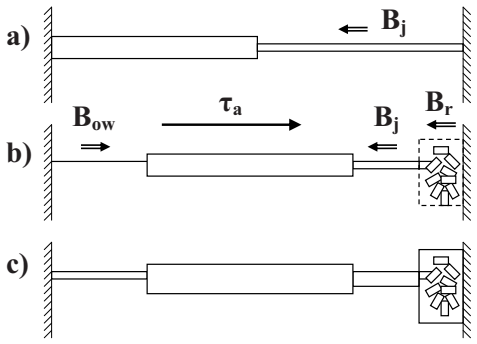

Figure 1: A simplified one-dimensional sketch showing a simplified cycle of one model time step. (a) Initially the bounded ice cover consists of one thick and one thin part. The weak ice category has in this case a formation direction B_j towards left. (b) When a wind stress τ_a is applied in opposite direction to B_j it will move the ice cover towards right. A part of the weak category will be deformed at the right boundary and form a ridge with a formation direction B_r, opposite to the direction of the wind stress. As the ice cover moved away from the left boundary, open water emerges which will be given the formation direction B_{ow} equal to the direction of the wind stress. The amount of open water formed is dependent on the ice speed and the length of time step. (c) The cycle ends with a thermodynamic computation where all categories grows (as in the figure) or melt according to the thermodynamic forcing.

The formation direction is defined mathematically by a unit vector, $\vec{B}$, parallel to the wind vector, ($\vec{B} = \vec{\tau}_a/|\vec{\tau}_a|$), where $\vec{\tau}_a$ is the wind stress vector. The open water category is given such a formation direction while the formation direction of the ridge category is opposite to the wind direction $-\vec{B}_j$. A vector definition of B is used in the mathematical description of the model although only a scalar quantity (angle) is needed to be stored in the model as indicated in (1). It should be noted that the newly formed area with formation direction $\vec{B}_{ow}$ (as in Fig. 1) will represent a weak part of the ice cover when wind shifts to the opposite (negative) direction. New categories are created almost every time the ice is set in motion by the wind and eventually the originally homogenous ice cover consists of a collection of categories including open water, level ice and pressure ridges. During the winter season, shifts in the wind field will, if the wind is strong enough, generate a mosaic of different ice categories within the pack ice. Fig. 2 shows schematically the definition of formation directions of new ice and ridged ice in two dimensions.

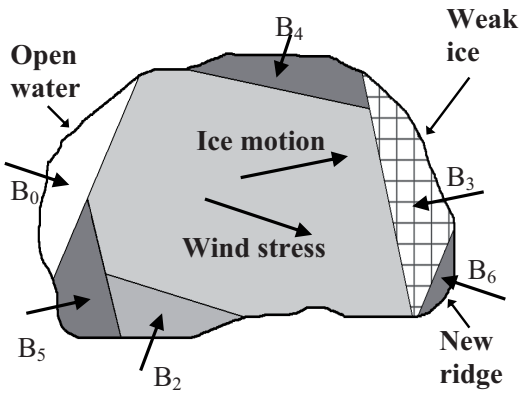

Figure 2: A conceptual sketch showing a mosaic of 6 different ice categories. Here a typical situation for a deformation process on a weak category (upper right) with formation direction B_3 is shown. The white area (to the left) represents newly formed open water with the formation direction parallel of the wind direction (B_0) and the new pressure ridge is also given the formation direction (B_6) parallel of the wind direction (lower right). Note that the actual shapes and positions of the different categories are not stored in the model. Note also that the ice motion in the model is defined to be directed towards and parallel to the weak category formation direction, while the new formation direction is parallel to the wind stress.

The dynamical formulation of the model is similar to what has been used in studies of the Marginal Ice Zone [Leppäranta et al., 1989]. The force balance is defined in a local (in time) coordinate system fixed to the formation direction of the actively deforming category. A definition sketch is shown in Fig. 3. The wind stress components in this local coordinate system are defined by

$$\begin{aligned} \tau_{ay} &= \vec{\tau}_a \cdot (-\vec{B}_j) \\ \tau_{ax} &= \vec{\tau}_a \cdot (\vec{k} \times (-\vec{B}_j)) \end{aligned} \tag{5}$$

where $\vec{B}_j$ is the formation direction of the deforming category, $\vec{\tau}_a$ is the wind stress vector, and $\vec{k}$ is a unit vector in the vertical direction. The wind stress vector is thus decomposed into one component perpendicular, τ_{ax}, and one component parallel, τ_{ay}, to $\vec{B}_j$. It is useful to introduce two imaginary coastlines parallel to τ_{ax} and τ_{ay} in order to describe the force balance. The ice

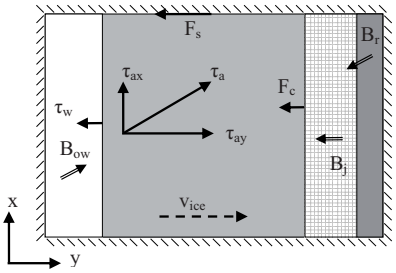

Figure 3: Definition sketch showing the force balance in the model during ice deformation and with wind stress $\vec{\tau}_a$ direction deviating from the formation direction $\vec{B}_j$ of the deforming category. The coordinate system is defined by the formation direction $\vec{B}_j$ with the y axis parallel to $\vec{B}_j$. Imaginary coastlines are also indicated in order to visualize how the internal forces are defined. The ice cover moves in the y-direction (v_{ice}) and deforms the weak ice (grid pattern) with formation direction $\vec{B}_j$ against an imaginary coastline parallel to the x-axis. This give rise to a force, F_c, due to the yield strength of the ice and opposing the wind stress. The wind stress has also a component against the coastline parallel to the y-axis which generates shear stresses and an additional force F_s opposing the wind stress. The ice cover is also affected by a water stress $\vec{\tau}_w$ acting against the ice motion. Note that the the forces F_c and F_s are force per unit length while the wind and water stresses are force per unit area. $F_c = \tilde{\sigma_j}$ and $F_s = \gamma\tau_{ax}$ in the formal notation in Eq. 8. The new ridged category (dark grey) is given a formation direction $\vec{B}_r$ opposite to the wind stress direction and the new open water category (white) is given a formation direction $\vec{B}_{ow}$ parallel to the wind stress.

motion is always parallel but opposite to the formation direction of the deforming category j. The yield strength of this category will then induce a force F_c against the ice motion due to compressive stress against the windward coastline. If the wind direction is not exactly parallel to $\vec{B}_j$ it will also generate a force F_s against the ice motion due to shear stress at the coastline parallel to τ_{ay}. There is also a water stress $\vec{\tau}_w$ directed against the ice motion. Model studies of ice drift in the Baltic Sea have shown that the inertia of Baltic Sea is insignificant and that quasi-steady-state solutions work well [e.g. Leppäranta, 1981, and references therein]. Assuming steady state, zero water velocity and neglecting the sea surface tilt the equations governing the local force balance become

$$\begin{aligned} 0 &= \frac{d\sigma_{xx}}{dx} + \tau_{ax} + \rho_w C_w \sin\theta_w v_{ice}|v_{ice}| \\ 0 &= \frac{d\sigma_{yx}}{dx} + \frac{d\sigma_{yy}}{dy} + \tau_{ay} - \rho_w C_w \cos\theta_w v_{ice}|v_{ice}| \end{aligned} \tag{6}$$

where σ_{xx} is the compressive stress in the x-direction, σ_{yy} the compressive stress in the y-direction, σ_{xy} the shear stress, τ_{ax} the x-component of the wind stress, τ_{ay} the y-component of the wind stress. The last two terms in each equation are the ice/water stresses where ρ_w is the water density, C_w ice/water drag coefficient, θ_w turning angle (see Table 1) and v_{ice} is the ice velocity. Hence the only stress derivative neglected here is the derivative of the shear ice stress in y-direction, $\frac{\partial\sigma_{yx}}{\partial y} \equiv 0$. By using a compressive-to-shear stress ratio γ specifying the shape of the elliptic yield curve in a viscous plastic rheology [Leppäranta et al., 1989] we can in steady state relate compressive ice stress to shear ice stress according to

$$|\frac{\sigma_{xy}}{\sigma_{xx}}| = \gamma \tag{7}$$

where care must been taken with the signs which will be dependent on the sign of τ_{ax}. The velocity parallel to the formation direction (y-direction in the local coordinates) is solved by

Table 1: The physical parameters used in the model.

Parameter	Value	Unit	Description
$L_{north-south}$	275	km	Basin length (north-south)
$L_{east-west}$	150	km	Basin width (east-west)
H_{min}	0.025	m	Minimum ice thickness participating in the merging process
ϕ_{max}	$\frac{\pi}{12}$	rad	Maximum distance between two categories that is merged
ρ_{ice}	920	kg/m^3	Sea ice reference density
ρ_w	1000	kg/m^3	Sea water reference density
C_w	$3.5{\cdot}10^{-3}$	-	Ice-water friction coefficient
θ_w	$\frac{\pi}{6}$	rad	Angle of turning

introducing the compressive-to-shear stress ratio and eliminates the derivatives in the x-direction. The resulting single equation for the balance in the y-direction is integrated between $y = 0$ to $y = L$ with the limits $\sigma(y = 0) = 0$ and $\sigma(y = L) = -\tilde{\sigma}_j$ where $\tilde{\sigma}_j$ is the compressive yield strength of category j. L is the length scale depending on the wind direction due to the shape and the size of the basin, see Fig. 4 and Table 1. Finally the ice velocity is obtained

$$v_{ice} = \sqrt{\frac{(\tau_{ay} - \gamma|\tau_{ax}|)L - \tilde{\sigma}_j}{\rho_w C_w(\cos\theta_w \pm \gamma \sin\theta_w)L}} \tag{8}$$

where the sign in the denominator is positive for $\tau_{ax} > 0$ and negative for $\tau_{ax} < 0$. Note that the wind stress is by definition always on-shore so that the sign of the τ_{ax} is not relevant for the shear effects. It can be seen from this equation that wind stress parallel to the y-axis will generate an ice velocity proportional to the difference between the total force in the y-direction and the yield strength. For non-parallel wind the velocity will be reduced not only from a reduced component in the y-direction but also due to shear stress induced by the component in the x-direction. In the notation of Fig. 3 then $F_c = \tilde{\sigma}_j$ and $F_s = \gamma\tau_{ax}$. The turning angle of the ice water stress will increase the speed somewhat when τ_{ax} is negative since the water stress then has a component opposite to τ_{ax} and reduces the total shear stress. For positive τ_{ax} the water stress will be in the same direction and increase the shear stress.

2.3. Deformation procedure

Two criterions must be fulfilled in order to start ice motion and deform a specific category. First, the wind stress vector must have a component in the opposite direction of the formation direction.

$$\vec{\tau}_a \cdot (-\vec{B}_j) > 0 \tag{9}$$

Second the integrated wind force component in the formation direction must overcome the retarding forces due to internal friction of category j (according to (8)) such that the ice can be set in motion

$$(\tau_{ay} - \gamma|\tau_{ax}|)L > \tilde{\sigma}_j \tag{10}$$

The thinnest ice category that fulfills both criteria (9) and (10) will control the ice motion according to (8). In the case when no ice category satisfies both conditions, no deformation (or motion) of the ice occurs during that time step. If both (9) and (10) are true the deforming category, j, will give away area fractions to a new category $(n + 1)$ of ridged ice and a new category of open water, $i = 0$. Thus, the time evolution of the area fraction a_i for each category is governed by

$$\frac{da_i}{dt} = \begin{cases} r & i = 0 \\ 0 & i = 1, j-1 \\ -\frac{M}{M-1}r & i = j \\ 0 & i = j+1, n \\ \left(\frac{M}{M-1} - 1\right)r & i = n+1 \end{cases} \tag{11}$$

The rate of deformation, r, is defined as the fraction of ice-free area generated by ice deformation per unit of time and can be estimated from

$$r = \frac{v_{ice}}{L} \tag{12}$$

The ridged category is defined to be M times thicker than the ice forming the ridge. A constant thickness multiplier is the simplest possible way to describe the ridging process. If the thickness of the weak category is e.g. 0.1 m and $M = 3$, the thickness of the ridge will be 0.3 m, which may be interpreted as the mean thickness of the ridge. The main functioning of (11) during a time step with deformation can be summarized as follows; (a) New open water area fraction for $(i = 0)$ with associated formation direction B_0 as defined earlier; (b) Decreasing area of the category $(i = j)$ which is deformed into ridges; (c) Increasing area fraction of a new category with ridged ice $(i = n + 1)$ also with an associated formation direction B_{n+1}. As seen here two new categories are formed by the deformation procedure, $i = 0$ and $i = n + 1$. The ridging may result in two cases; (*i*) If $\frac{M-1}{M}r\Delta t$ is smaller or equal to a_j, the appropriate fraction of weak ice is ridged during the time step, Δt; (*ii*) If $\frac{M-1}{M}r\Delta t$ is larger than a_j the entire area of weak category of ice is ridged but some part will then remain of the total time step. The entire procedure with finding a new category and deformation is then repeated until the entire time in the time step is used up. The factor $\frac{M}{M-1}$ comes from the fact that thick ridges (large M) will occupy smaller area fraction than thinner ridges. The index 0 for the new category is only used temporarily. The index of all categories is incremented one step when the procedure is finished.

2.4. Merging procedure

Since new categories are generated almost each time step, merging of categories are needed to keep the number of categories on a manageable level, but the important directional information of weaknesses in the ice cover must still be preserved. The present procedure for selecting two categories i and j that will be merged into the one category k is a modified version of the procedure described in Björk [1992]. Instead of merging thinnest ice first, the new procedure starts with the categories of thickest ice. The two categories with the smallest thickness difference are merged, but categories thinner than H_{min} are excluded from merging, in order to preserve formation direction for thin ice. An additional condition is that only categories with relative similar formation direction can be merged. The angle difference has to be smaller than the angel ϕ_{max}

(see Table 1). When merging two categories i and j, the new ice thickness H_k, snow thickness h_k and formation direction $\vec{B}_k$ are calculated as area weighted means of the state variables of the merged categories. Exceptions are the area fraction a_k, which is simply added together and the temperature T_k, which is computed under the condition that the total heat should be conserved [Björk, 1992]. It follows from the definition of the categories that only one category of open water exists. Two categories of open water (i and j) may arise when deformation takes place. In this simplified model, these two categories are instantly merged into a category k and the new category inherits the formation direction of the categories i or j having the largest area fraction.

2.5. Ice strength parametrization

The pure compressive ice strength is taken to be proportional to the ice thickness according to $\tilde{\sigma} \propto cH_{ice}^{b}$. Two commonly used values for b are tested in the model, $b = 1$ the linear approach (LA) and $b = 2$ the non-linear approach (NLA). In conventional 2D-models, c usually also includes a strong dependence of the ice compactness since each grid cell may be occupied by open water and ice of one or several thicknesses [e.g. Bitz et al., 2001]. In the present model H_{ice} is simply the thickness of one particular ice category and the compactness dependency is therefore omitted. The LA has been used in several ice dynamic models [e.g. Flato and Hibler, 1995, Haapala and Leppäranta, 1997, Haapala, 2000, Pritchard, 2001]. The LA parametrization for the compressive strength reads

$$\tilde{\sigma}_j = P^* H_j \tag{13}$$

Here P^* is an empirical compressive coefficient. The NLA is given by the following expression

$$\tilde{\sigma}_j = \rho_{ice}\mu_0 H_j^2 \tag{14}$$

Here ρ_{ice} is the density of ice and μ_0 is an empirical compressive coefficient. This parametrization was suggested by Overland and Pease [1988] based on energy arguments such that the ridging stress is associated with an increase in potential energy from submerging blocks [Rothrock, 1975].

2.6. Thermodynamic and oceanic models

A one-layer thermodynamic ice model computes the time dependent evolution of H_i, h_i and T_i independently for each category according to the atmospheric forcing and heat flux from the ocean. The model includes the effect of salt enclosed in brine pockets and formation of snow ice. The internal ice temperature is determined by a prognostic equation for ice thicker than $25cm$. For thinner ice, T is simply computed as average of the ice upper surface temperature and the bottom temperature. The snow thickness is determined from the balance between accumulated snowfall and melting. Snow is also lost due to snow ice formation. For a detailed description of the thermodynamic model, see Björk [1992] and Gustafsson [2003]. The ice model should be coupled to an ocean model in order to make realistic long term simulations. The ocean model provides with a lower boundary condition for the ice sub-model where the heat flux from the ocean into the ice is a critical quantity for controlling the freezing and melting rate. In the present investigation the ice model is applied to the Bothnian Bay (Fig. 4) and a specific ocean model is used for this area. This model uses a one dimensional column model approach for the entire Baltic Sea and Kattegat area. The area is divided into 13 sub-basins including the Bothnian Bay [Gustafsson, 2003]. The Bothnian Bay sub-basin of the model is forced by wind stress (every

3 hours), air temperature, cloudiness, humidity, precipitation and atmospheric pressure from the meteorological station Rödkallen (Fig. 4). The observations are used to calculate the wind stress together with radiative, sensible and latent heat fluxes. The model is run with a time-step of 3 hours.

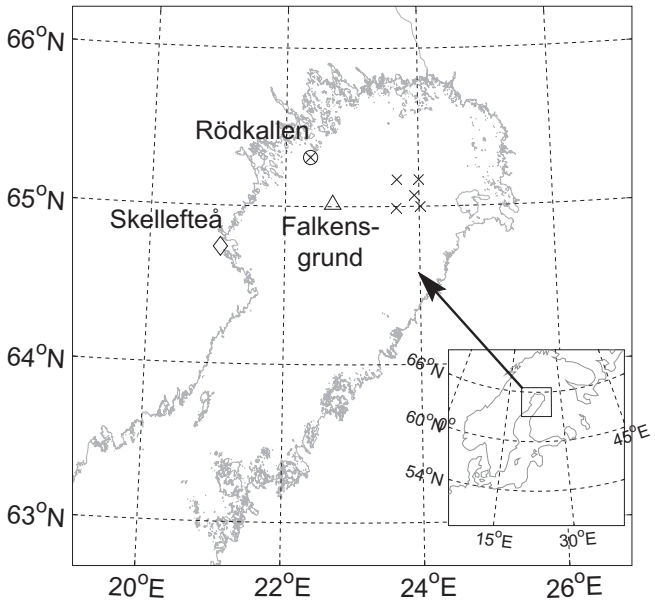

Figure 4: Map of the Bothnian Bay in the northern part of the Baltic Sea, marked with positions for the meteorological observational station Rödkallen (marked with ⊗) [65° 18.6' N, 22° 22.2 E], the larger city Skellefteå (marked with ◇), the ADCP deployment site at Falkensgrund (marked with △) [65° 01' N, 22° 43' E] and ice drifters (marked with ×).

3. Results

3.1. Search for a best case of parameter values

A large number of runs have been performed in order to test the model sensitivity to the main dynamical parameters (P^*, μ_0, γ, M) and to find an optimal set of parameter values. Both linear and non-linear ice strength parameterizations were investigated, (equations 13 and 14). Literature values of some of these parameters vary widely. For P^* the values range from (1 - 100) kN/m^2 (typically P^* = 25 kN/m^2 for the Baltic Sea) and for γ, the range is $0 \ll \gamma < 1$ (typically γ = 0.50) [Leppäranta, 2005]. A range for the NLA coefficient μ_0 is difficult to find in the literature, but the empirical value of 1.6 N/kg found by Overland and Pease [1988] may represent a typical value for oceanic ice conditions. Note that this comparison is not straight forward since P is based on one single category of ice in this model, while conventional 2-D models are based on A and $\overline{H_{ice}}$ within the grid cell. The ridge multiplier may vary from simple rafting (M=2) to values

Table 2: The range of simulation parameters used in the sensitivity test.

Parameter	Range	Unit	Description
P^*	1-60	kN/m^2	Ice strength parameter for LA
μ_0	1-100	N/kg	Ice strength parameter for NLA
γ^{-1}	2-6	-	Compressive-to-shear ice stress ratio
M	3-6	-	Ridge ice thickness multiplier

as high as 15 in the Arctic Ocean [Björk, 1997]. However, here we only test a limited range of the parameters and the range used in the sensitivity test is presented in Table 2.

The modeled ice velocity is compared with a high-resolution time series of ice velocities from the winter of 2003/2004 measured by an upward looking ADCP deployed at Falkensgrund in the center of the Bothnian Bay (see Fig. 4) [Björk et al., 2008]. A persistent ice cover at Falkensgrund was observed between January 28 and May 8, but only the tree full calendar months of the ice observations (February to April) are used in this analysis. The ADCP data set has a time-resolution of 10 minutes. A 3-hour moving median filter has been applied for the comparison with model results. The explained variance E is used to quantify how well the observed ice motion is reproduced by the model.

$$E = 1 - \frac{\sum(\vec{U}_{mod} - \vec{U}_{obs})^2}{\sum(\vec{U}_{obs} - \overline{\vec{U}_{obs}})^2} \tag{15}$$

Here $\vec{U}_{mod}$ and $\vec{U}_{obs}$ are the modeled and observed ice velocity vectors, respectively.

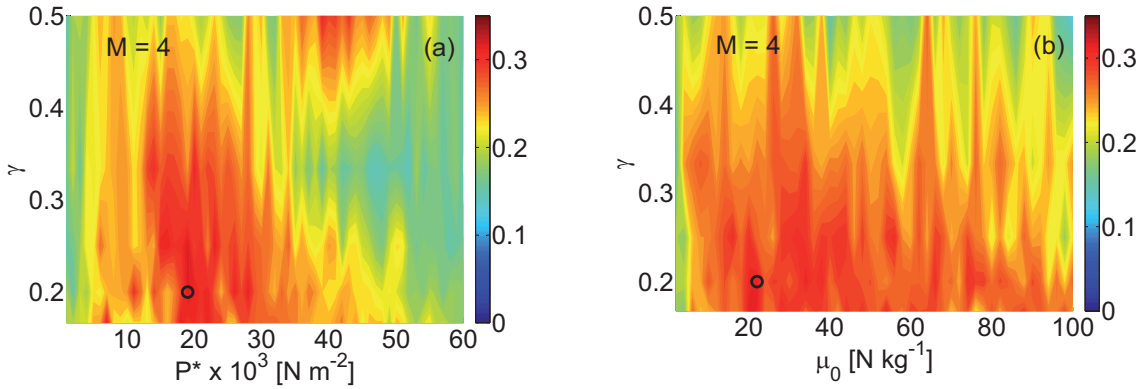

Figure 5: Contour diagram for explained variance, E, between ice velocity observed at the Falkensgrund, measured by the upward looking ADCP, and model ice velocity. Panel (a) shows E as a function of γ and P^* for the LA and panel (b) shows E as function of γ and μ_0 for the NLA. Results are for M = 4 for both panels and the black circle in each panel marks the optimal parameter settings. For the LA the maximum ($E \approx 0.33$) is obtained for $P^* = 19$ kN/m^2 and $\gamma = 0.2$. The maximum value for the NLA ($E \approx 0.33$) occurs for $\mu_0 = 22$ N/kg and $\gamma = 0.2$.

The explained variances as function of γ and P^* for the LA and γ and μ_0 for the NLA are

shown in Fig. 5 for the optimal value of $M = 4$ for both approaches. For the LA a well defined maximum of $E \approx 0.33$ is obtained for $P^* = 19$ kN/m^2 and $\gamma = 0.2$. The maximum value for the NLA ($E \approx 0.33$) occurs for $\mu_0 = 22$ N/kg and $\gamma = 0.2$ but not as distinct as for the LA. For the parameter M, ranging from 3 to 6, explained variance varied between 0.31 to the maximum value of 0.33, using the optimal parameter values. For comparison the ice strength is drawn in Fig. 6 against the thickness for LA and NLA with the optimal parameter settings. The LA and the NLA will give the same strength for $H_m = 0.94$ m, and consequently the NLA has weaker ice for $H_m < 0.94$ m.

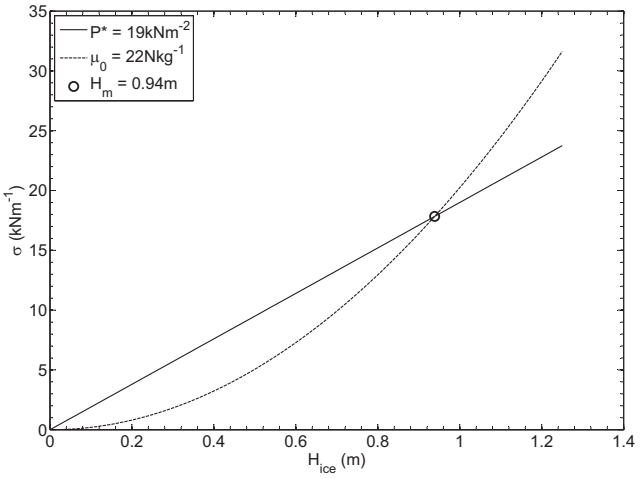

Figure 6: Ice strength for the LA and NLA optimal parameter settings in Fig. 5 as a function of ice thickness, $P^* = 19$kN/m^2 and $\mu_0 = 22$ N/kg. The curves intercept at $H_{ice} = 0.94$ m.

Another interesting point is that in contrast to the LA where one clear optimum is found, several candidates for an optimal solution emerge for the NLA and mainly for larger ice strength $\mu_0 > 22$ N/kg. A general feature is that the model is relatively insensitive to the value of γ, especially for the LA. This indicates that shear stresses are not as important as compressive stress. The explained variance might seem rather low but this can be expected since there are several difficulties comparing model with observations for such a long and high frequency sampled time series like the ADCP data set. In the model, the ice tends to move with a more or less constant speed during 3-hour intervals controlled by the forcing data. The observed ice velocity is sampled with much higher frequency and is more dynamic even though the data are filtered somewhat. The short time series shown in Fig. 7 is an example that clearly illustrates the difficulties in obtaining a higher explained variance. Other errors, such as observed ice movements when the model gives zero ice velocities (due to high ice strength), divergences in the ice cover due to variable forcing over the basin (which is not incorporated in the model) or forcing by ocean currents may also explain the relatively low value of E.

3.2. Comparison with observed ice velocity at a single point

The time series of the velocity components using the optimal parameter setting for the LA and the NLA are shown together with the observed ice velocities from the ADCP and free drift ice velocity in Fig. 8. Here we see a relatively good agreement between observed and simulated

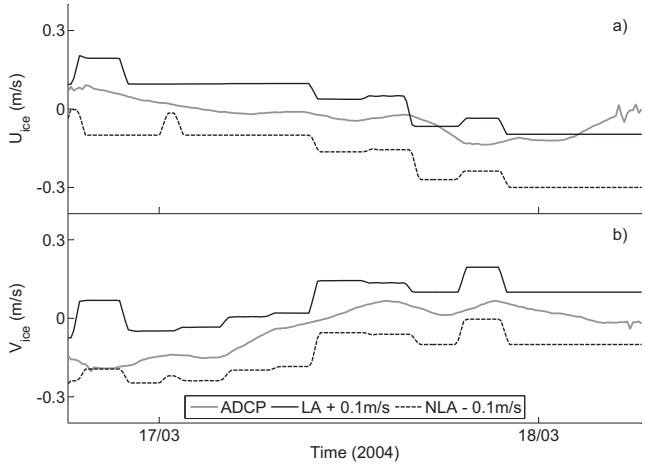

Figure 7: Detailed time series showing an example of the differences between the model and observed ice velocities used in calculating explained variance. a) U-components (positive eastward) and b) V-components (positive northward) Note the more step-like behavior of the model velocities due to the lower observational frequency of the wind forcing (3 h) compared to ADCP observations (10 min). Note that LA velocities are shifted +0.1m/s and NLA velocities are shifted -0.1m/s.

velocities in that most of the major motion events are captured by the model in a realistic way. Although the curves look similar, there are significant differences between the model simulated ice velocity and free drift. In particular during a longer period in February when the model computed U-velocity is much smaller than the free-drift velocity. There are, of course, discrepancies since the model treats the ice dynamics in a very simplified way and that the comparison is only for one single observation site. The results are relatively similar for the linear and non-linear strength parametrization. The model gives generally too small amplitude for transients of the ice motions. It is however not obvious that this is due to imperfection in the model ice dynamics since wind forcing is not particulary strong during these events. Thus, the problem might be either that the wind data are not representative or that forcing by ocean currents is significant. An example of this is one event in mid April that is characterized by a wind burst of about 10 m/s from south. This wind speed should not really be able to generate an ice velocity of 40 cm/s as observed by the ADCP, unless the ice cover is in free drift. From observations on ice charts produced by SMHI (The Swedish Meteorological and Hydrological Institute, not shown) there are no indications of open water or new thin ice in the north supporting a free drift situation. From the water column ADCP data (not shown), there is indeed a strong barotropic current. Since the model does not include any mechanical forcing from the ocean, it cannot give realistic velocities during such events. Another striking feature is that from the mid of April, the modeled ice velocity is near zero for long periods of time while the observation show events with significant speed. The ice cover seems to be too stiff during this period, indicating that there are some omitted processes in the model during the breakup phase of the ice cover. A closer inspection of the results shows that the temperature is generally above 0 °C and there is no insulating snow cover on top of the ice which makes it possible for the solar radiation to penetrate into the ice cover. Thus it might well be the case that the ice is melting internally which should break up the bounds between the crystals and make the ice weaker and more deformable. This effect is not

included in the present model.

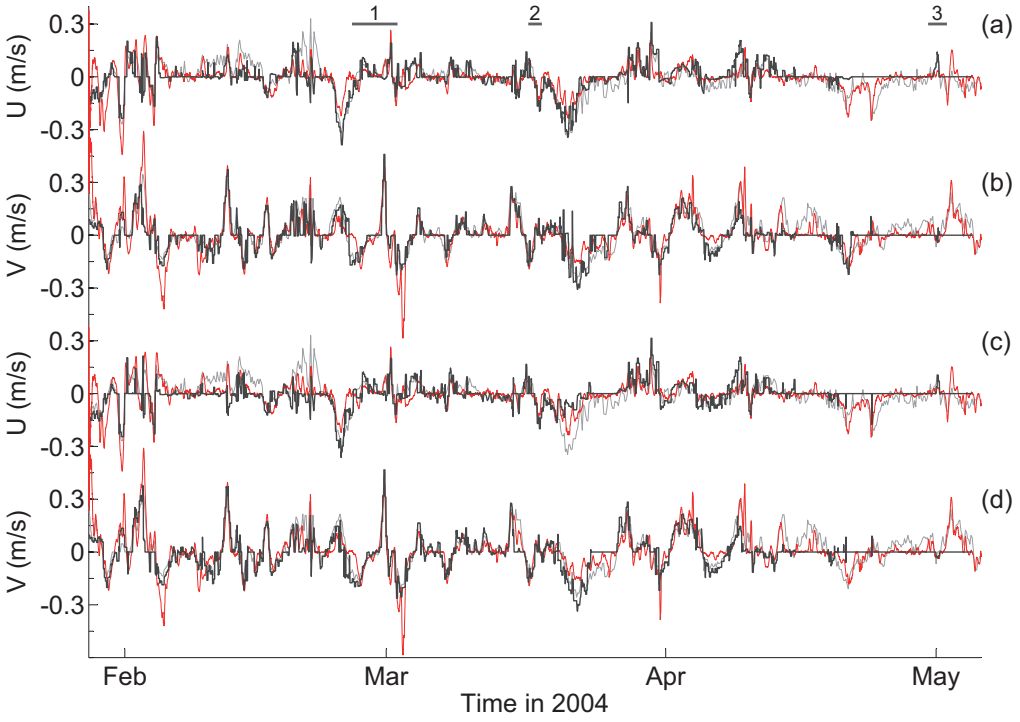

Figure 8: Comparison between modeled ice velocity, observed ice velocity from ADCP measurements at Falkensgrund and free drift ice velocity. u-components positive northward and v components positive eastward. The red curve is the observations with an 3-hour moving median filter applied, the black curve is the model ice velocity and the gray curve is the free drift velocity. Panels a) and b) are for linear ice strength, LA, and panels c) and d) are for non-linear ice strength, NLA. The numbered bars on top (1 - 3) indicate periods for which ice trajectory comparisons are presented.

3.2.1. Comparison with ice trajectories

Three illustrative periods (marked with bold lines labeled 1 - 3 in Fig. 8) have been analyzed in more detail. Period 1 has shifting winds and full ice cover in the basin and is thus very demanding with respect to simulate correct ice dynamics. Period 2 is a situation with nearly free drift of the ice cover. Period 3 illustrates the difficulties of simulating ice motion late in the ice season. These periods are compared to ice motions from the upward looking ADCP and daily ice charts from the Bothnian Bay (not shown). Prior to comparing the ice motions, it is worth noting that the modeled ice motion is highly influenced by the historical information stored in the formation directions which makes the whole comparison very subtle.

The simulated and observed ice motions and wind vectors for the first period are shown in Fig. 9. The air temperature stayed well below freezing most of the period, reaching $-20\,^{\circ}$C. In general the model follows observations quite well, it captures the major events both in direction and distance made. The explained variance is substantially higher than the average for the entire winter; 0.60 and 0.58 for the LA and NLA, respectively. The error is larger for the NLA and the cause can be found in the information stored in the formation directions. Fig. 10 shows

the location and area fraction of the categories prior to and after the event. This figure also illustrates the kind of information contained in the model. Separate panels are drawn for open water, level ice and ridged ice. The location of open water shifts position from southwest to west and the NLA gives significantly smaller opening area fraction (Fig. 10a and d). Generally for both approaches, level ice in southeast is deformed into pressure ridges, while new level ice categories appear in northwest. Deformation is more pronounced for NLA which tends to be more dynamic (Fig. 10b and e). Ridged ice categories in north and south are primarily merged into new deformed categories in order to keep the number of categories limited (Fig. 10c and f). For LA the number of level ice categories dropped from 40 to 19 during the event, while the number of ridge ice categories stayed constant. For NLA the number of categories stayed unchanged both for level and ridge ice categories.

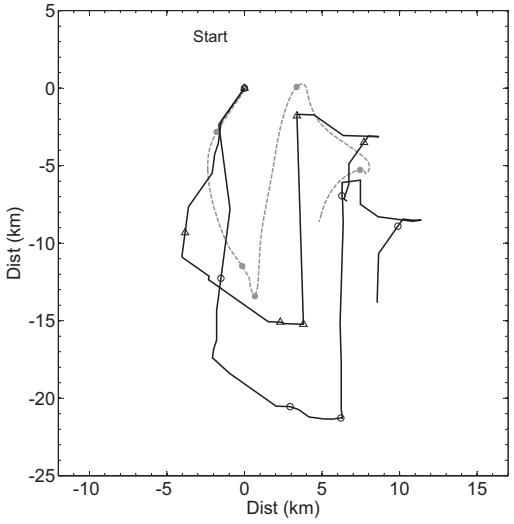

Figure 9: Trajectories showing an example of ice motions early in the ice season (2004-02-26 to 2004-03-02). This event has shifting winds and full ice cover in the basin and is thus very demanding with respect to simulate correct ice dynamics. Dashed line is the observed ice movement, line with △-marking is the LA and line with ∘-marking is the NLA, all with daily markings.

The second event is shorter but according to ice charts prior to this event, an area of quite open pack ice is found in the southeast of the basin while the rest consist of closed pack ice. During the event, a wind of about 5 m/s moves the ice offshore about 8 km in the southward direction (Fig. 11). There is a relatively good agreement between the observation made by the ADCP and the simulated ice motion. Southward motion continues until the wind direction reverses for a short period moving the ice cover slightly northward. At the end of the event the wind turns easterly and the speed increases to 6 m/s, which causes the ice cover to move towards the Swedish east coast. The theoretical free drift trajectory as well as model results and observations indicate that the major force balance is between wind and water stress with just a minor contribution from internal ice stress.

During the last event, the ice charts roughly indicate a relatively immobile pack ice, with an estimated level ice thickness of 30 - 60 cm scattered with numerous ridges, situated in the northwestern part of the basin. In the southeast, the ice cover is completely open. The ice

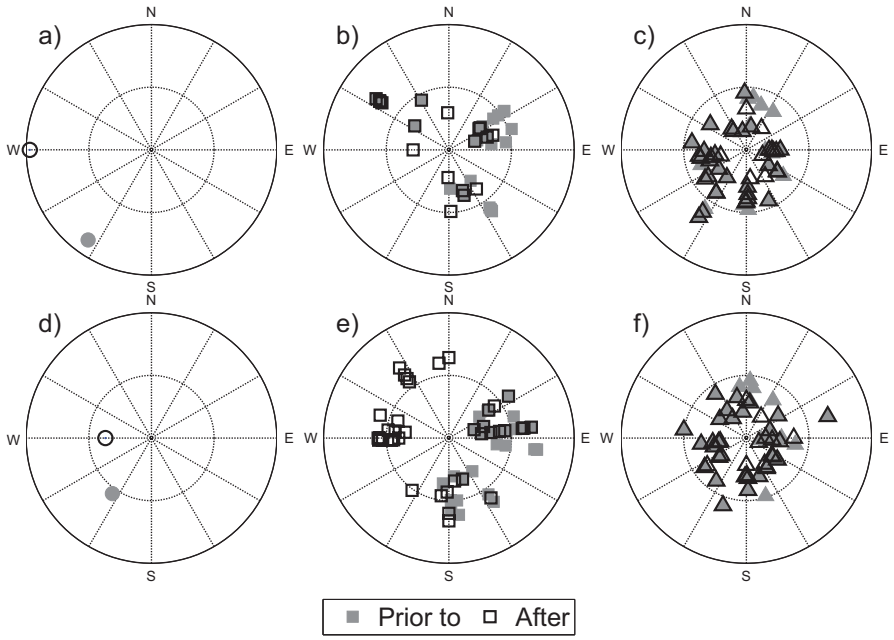

Figure 10: Formation directions and area occupation for the categories open water (panels a and d), level ice (panels b and e) and ridged ice (panels c and f) for LA and NLA, upper and lower row, respectively. The markers are plotted in a compass coordinate system indicating the direction of formation (B_i) and the distance from origin represent the area fraction (a_i) occupied by each category. Filled markers indicate locations of categories prior to the event (2004-02-26), while open markers indicate locations of categories after the event (2004-03-02). Ice motions in between these two dates are shown in Fig. 9.

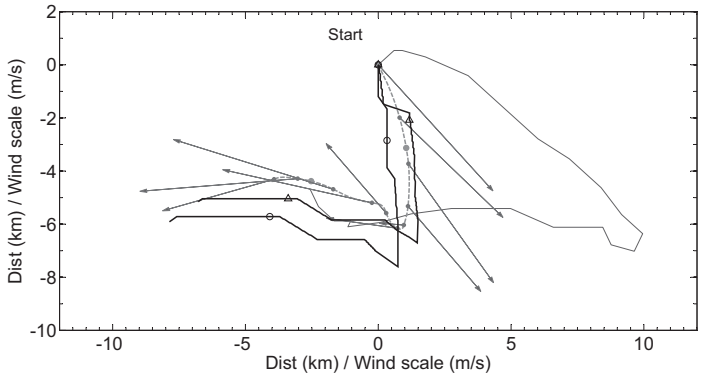

Figure 11: Trajectories showing an example of ice motions in the middle of the ice season (2004-03-16 to 2004-03-18) and with good agreement with observation. This event is a situation with nearly free drift of the ice cover and the ice motion is compared to a trajectory showing the theoretical free drift of the ice cover (thin solid line). Dashed line is the observed ice movement, arrows represents the wind vector, line with △-marking is the model with LA and line with ○-marking is the model with NLA, all with daily markings. Wind vectors are given every 3 hours, scaled with a factor of 10^3 m/s.

trajectories and theoretical free drift for this period are shown in Fig. 12. The period starts with an ADCP record of a short northward ice motion due to a wind speed of 5 m/s and this motion is not captured by the model. A modest wind speed of 5 m/s can only apply strong enough force to deform ice thinner than 40 cm for LA and 60 cm for NLA. The thinnest ice in this direction is apparently thicker than this and the ice does not move. Thereafter the model gives an eastward ice motion which is confirmed by the ADCP. Here the model has kept track of the location of the category of open water and the model ice motion is close to the theoretical free drift, reaching a maximum of 15 cm/s. Thus the model ice drifts reached 14 cm/s for LA and 11 cm/s for NLA. When the wind becomes southerly again it moves the ice a long distance toward north (about 20 km), as recorded by the ADCP. The model does not follow this motion because the ice is too thick to be deformed for this low wind speed.

4. Dynamical versus thermodynamical ice growth

As a model application we have investigated how dynamic processes influence the ice volume of the Bothnian Bay. Deformation of the ice cover produces open water areas in which the ice production can be much larger than for the surrounding ice. This results in dynamic ice growth in addition to the pure thermodynamic growth. The modeled maximum spatial average ice thickness for each year is shown in Fig. 13 for the period 1991-2004. For reference, the anomaly of the Dec-Apr means of air temperature, wind speed and direction are shown in the upper panel. The dynamic ice production typically increases the ice volume with 80% compared to the pure thermodynamic growth. Thus dynamic processes give a large and important contribution to the total ice volume in the Bothnian Bay. Such large contribution from dynamical processes is

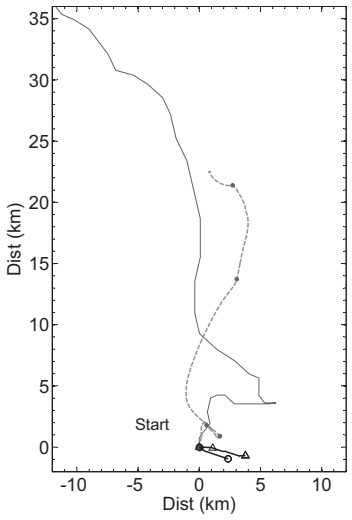

Figure 12: Trajectories showing an example of ice motions late in the ice season (2004-04-30 to 2004-05-02) with large deviation between the model and observed motion. This event illustrates the difficulties of simulating ice motion when the remaining ice is too thick to deform. A free drift trajectory of the theoretical free drift of the ice cover is plotted (thin solid line) to exemplify the behavior of the model. Dashed line is the observed ice movement, line with △-marking is the LA and line with ○-marking is the NLA, all with daily markings.

confirmed by ADCP observations of the ice thickness showing that pressure ridges make up a significant part of the ice volume [Björk et al., 2008]. The amount of ridges as measured by the ADCP in March 2004 was about 60%. These observations includes just ridges thicker than 1 m (due to the relatively low resolution of the instrument) and the actual total amount of ridged ice should therefore be somewhat higher. In comparison, the total amount of ridged ice is about 80% in the model.

The linear and non-linear ice strength approaches give relatively similar ice thickness during most years but there are exceptions like 1999 when the difference is more than 20 cm. The LA gives generally somewhat thinner ice, 0.89 m compared to 0.94 m for the NLA, most probably due to the larger ice strength for thinner ice (see Fig. 6). Daily cumulative ice thickness distributions (ITD) have been computed for 1995 and 1999 for both the LA and NLA, and these are drawn in Fig. 14 and illustrate the differences in ice mobility. Binned daily ice thickness distributions are computed from the model's dynamic thickness distribution. In 1999, ice thinner than 20 cm occupies a much larger area for the NLA than for the LA. Compare, for example, February 1999 (day 32-59) when about 70% of the area was thinner than 20 cm for the NLA compared to about 45% for the LA. It is also evident that the more dynamic NLA cause larger open water fractions during ridging events and also generates more ridged thick ice > 72 cm. The larger fraction of thinner ice in the NLA, gives also a more rapid increase of ice free area during the final melting in spring. Complete meltdown of the entire ice cover occurs however at the same date for the two approaches since it is controlled by the thickness of the thickest ice which is similar for both. A year with similar maximum ice thickness for the two approaches is 1995 when also the ITD had similar development over the season (Fig. 14a and c). The ice cover consist mostly of thin ice $H_{ice} < 56$ cm for both approaches. However, the NLA gives somewhat

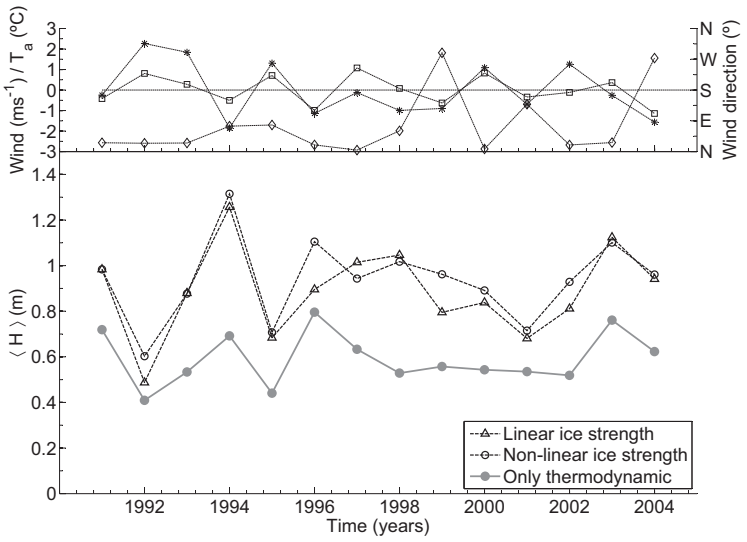

Figure 13: Upper panel shows anomalies of the five month means of air temperature (∗), wind speed (□) and wind direction (◊) for each year over the period 1991-2004. Anomalies are defined as deviations from the mean over the entire period. The lower panel shows the maximum ice thickness each year $\langle \overline{H} \rangle$ over the period. Curve marked △ is for the LA and curve marked with ○ is for the NLA. The dotted line shows the model computed ice thickness with no ice dynamic.

larger area of really thick ice, i.e. > 100 cm.

A likely general cause for differences of the maximum ice thickness that occurs some years between the two approaches may be identified from Figs. 13 and 14. There is a tendency that the NLA gives more ice production for years with low wind speed and low temperature (both have negative anomalies). Weak winds favors larger ice production in the NLA since the weaker thin ice causes more open water generation resulting in higher ice production, but the temperature needs also to be lower than normal in order to maintain a high heat loss to the atmosphere for weaker wind.

5. Discussion

It should be kept in mind that the present type of ice model is meant to provide with a realistic as possible first order description of dynamic ice processes without the need of using a two dimensional grid. This makes the model relatively crude by necessity but it should still give a much better description of the ice cover than a model based on only the thermodynamics. A perfect match with data cannot be expected since the model parameters represent a basin average as for example, the ice velocity. The entire motion field in the basin is represented by one value in the model which then has been compared with data from a single position. However, in order to be useful the model should still provide realistic ice motion by reproducing the main motion events with a realistic velocity scale and direction. We think this is the case judging from the direct comparison in Fig. 9. We would also like to stress that some of the discrepancies between model and data likely result from omitted mechanical forcing from high frequency ocean motions which would give errors in any type of ice model.

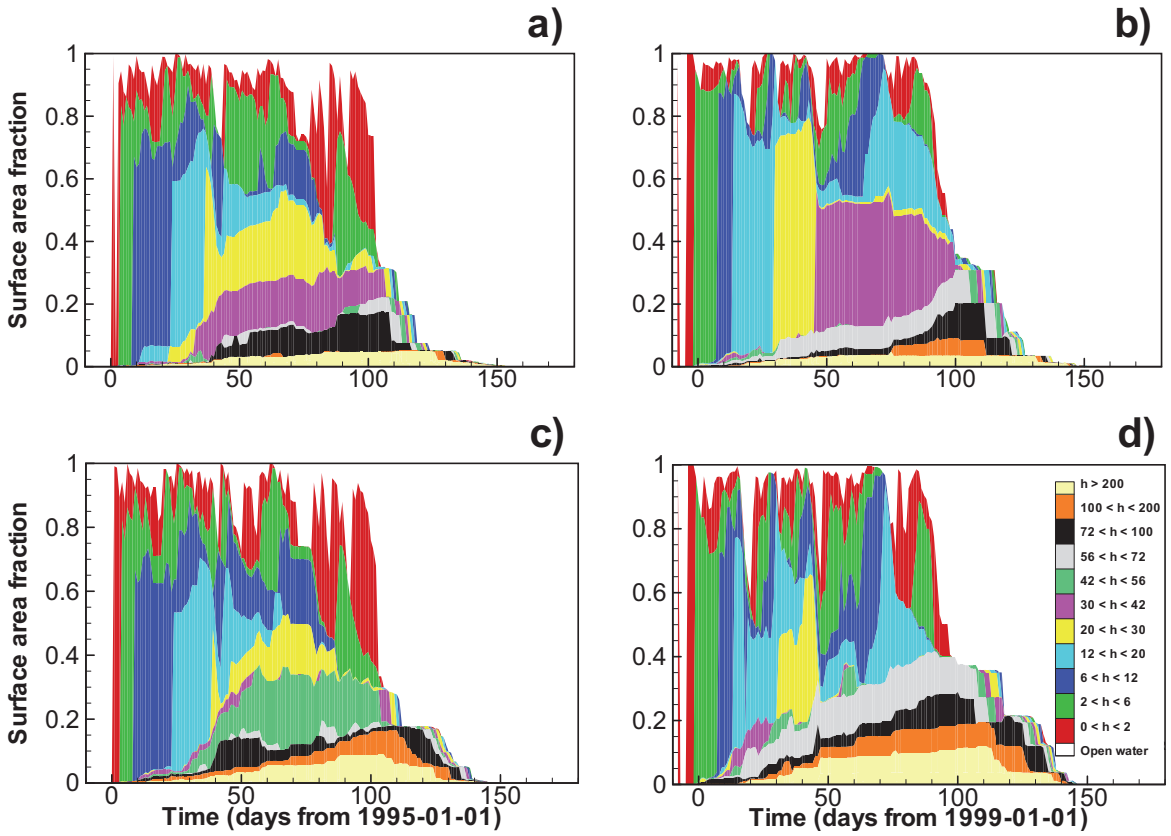

Figure 14: Ice thickness distribution, i.e. area fraction as function of daily cumulative ice thickness and time, for the LA (panel a and b) and NLA (panel c and d). Panel a and c are for the year 1995 when the LA and NLA give similar maximum ice thickness (see Fig. 13) and panel b and d are for the year 1999 when the LA and NLA give different maximum thickness. The unit for the thickness h is cm.

The main purpose of developing this type of dynamic ice model was to improve the existing horizontal integrated coupled column models used in the Baltic Sea. These models are developed to simulate physical biogeochemical processes in the ocean without describing the detailed horizontal field. The dynamical formulation of the present model which is based on the findings made in several studies of the MIZ [e.g. Leppäranta et al., 1989] should provide a higher level of reality than in presently used integrated models.

The basic concept of the model by storing information of weak directions of the ice cover seems to be working in general but it should be kept in mind there are restrictions of the basin size. The basin should be small enough in order to have a coherent ice motion over the major part of the basin. There exist some data from ice drifters that can be used to exemplify coherence between different points in the basin. In March 1997, drifters were deployed relatively near the fast ice zone at the Finish coast in a sector of 64.9° - 65.2° N and 23.6° - 24.1° E [Zhang, 2000] (see map of the Bothnian Bay in Fig. 4). In general, all of the drifters moved in a clockwise circular fashion. However there where differences, e.g. the drifters closest to the shear zone were probably hampered by pressure ridges trapped by the fast ice zone, while the drifters further out were probably situated in a more loosely packed drift ice. The basin scales for which the model is applicable needs thus to be investigated further. One major scaling variable is the basin size which should be significantly smaller than the scale of weather systems like low pressures.

This is well fulfilled for the Bothnian Bay having a scale of 300 km which is much smaller than the typical synoptic scale of low pressure system. Other basins with pack ice that also fulfil this conditions are eg. White Sea, Hudson Bay and the North American Great Lakes. Larger lakes in the northern Europe like Vänern, Ladoga, Onega and Peipsi may be applicable. Recently, Lake Peipsi in Finland was used as an example of modeling larger lakes with a mesoscale sea ice model [Leppäranta and Wang, 2008].

Our original intention was to find the best of the two different ice strength parameterizations. This has not really been possible due to a combination of the model complexity, omitted processes and imperfection in forcing and verification data. The ice velocity at a given time is not only dependent on the ice strength parametrization but also on the complete state of the ice cover, including the thickness distribution and formation directions, which impose a dependence on the development of the ice cover over the whole season. We see that some omitted processes like stresses from ocean currents sometimes give large deviations between observed and modeled ice velocity, and increase the difficulties to evaluate the ice strength parameterizations. Further discrepancies between observations and model results are added from non-coherent motions, clearly showed by the drifter data. Non-coherent motions are not resolved by the model neither by the ADCP data. Finally, wind forcing data are just from one location and with relatively low time resolution which also makes it hard to evaluate between different ice strength behaviors.

It is interesting to note that the optimal ice strength (P^*) obtained for the linear approach (LA) is of the same magnitude as commonly used in Baltic Sea ice models [Leppäranta, 2005]. The optimal ridge multiplier (M) is also in good agreement with the one used in other sea ice ridging schemes for the Baltic Sea [e.g. Gustafsson, 2003], and as expected much smaller than the one used in Arctic Ocean [e.g. Björk, 1997, Schramm et al., 1997, Lindsay, 2003]. The aspect ratio of the yield curve (γ) is in the same range as Leppäranta et al. [1989] found in their analysis for the MIZ, whilst the commonly used value is about 0.5. For the non-linear approach (NLA), the optimal μ_0 was found to be more than 10 times larger than what Overland and Pease [1988] used in their study. They derived the value of μ_0 from a comparison between the LA and the NLA where they adopted an empirical value of $\tilde{\sigma}_e = \sqrt{2} \cdot 10^3$ N/m with a mean ice thickness of $\overline{H}_{ice}$ = 1.0 m to match an empirical value of $P^* = 1 \cdot 10^3$ kN/m^2 [Rothrock, 1975]. If we instead use

the P^* from this study, but with the same ice thickness, we end up with $\mu_0 = 20.6$ N/kg, which is quite close to the optimal value of Overland and Pease [1988]. Bearing in mind the wide span in literature values on P^* and that the ice strength in the brackish Baltic Sea is greater than the one in oceanic waters [Leppäranta, 2005], the value of μ_0 in this study is not unrealistic for the non-linear ice strength parametrization. According to Fig. 5 the LA appears to give realistic results for P^* between an upper and lower limit (5 kN/m^2 $< P^* <$ 40 kN/m^2) for $E > 0.25$. For the NLA, however, only a lower limit is distinguished ($\mu_0 > 5$ N/kg).

A low sensitivity to γ in the model is quite evident (see Fig. 5), because the wind direction is normally relatively close to the formation direction of the weak ice. This makes the $\gamma\tau_{ax}$ term in Eq. 8 small. The sensitivity to γ is especially low for the NLA. One of the reasons for this is that the wind forces easily move and deform the ice cover when the thin ice fraction is relatively large. Fig. 14 shows that the area fraction of thin ice is generally larger for the NLA. Deviations of the wind direction from the formation direction which generates shear stresses do not then affect the ice velocity so much since the ice cover is more often close to a free drift balance. When the ice cover tends to be thin, the size of the yield curve may therefore not be as important to the deformation process as for a thicker ice cover.

In transients, the model does not respond as fast as observations indicate. This could be due to an oversimplified ITD composition in the model only treating three types of categories: open water, level ice and pressure ridges. Incorporating more ice types, like rafted ice, or multiple categories of open waters should probably shift the ITD towards larger fractions with thinner ice. The ice cover would be generally weaker and more responsive to wind shifts. Simulations with reduced ice strength support this by giving a more rapid response of the ice cover. However, by reducing P^* and μ_0 the ice motions are exaggerated and do not conform to observed velocities. The problems with the transients could also imply that $\tilde{\sigma}$ might be a function of not only H_{ice} but also other variables, such as time and space [Lipscomb et al., 2007]. Examining the short period showing the ice trajectory (Fig. 9) reveals an increased simulated velocity in the southward direction, compared to the observed ice motions. This again could be due to the history in the ITD or too large fetch in the north-south geometrical direction of the basin. However, this feature is not seen when the ice moves northward again, instead it corresponds well with the observations. Conclusively some differences are seen between the LA and the NLA and these are most likely due to interaction between the ice dynamics and the ITD.

The model ice cover appears too stiff in the later part of the winter with smaller ice motion compared to observations, from mid April and onwards. The commonly used compressive strength parameterizations, also used in this study, do not depend on seasonal variations in the ice properties. It is known that the flexural strength in sea ice is dependent on brine pockets [Timco and Johnston, 2002]. Thus when the air temperature increases and the sea ice melts, brine pockets tend to increase in size and the sea ice becomes very porous [Anderson and Weeks, 1958]. It is also likely that penetrating solar radiation further loosens up the crystal structure when the snow cover has melted away in spring. To the authors knowledge no attempts have been made to include these effects in dynamic sea ice models. Another shortcoming is that the model only treats one category of open water at the time. Late in the season when thin ice starts to melt there should have been several areas of open water in between the thicker ridges and when the ice cover is set in motion, these areas are easily closed. If multiple open water categories are implemented the model should likely be able to better capture these motions.

Acknowledgements. Meteorological observation data were provided by the Swedish Meteorological and Hydrological Institute. This work has been funded by the University of Gothenburg,

the Swedish Research Council under the contracts G 600-335/2001 and 621-2003-3425 and the MARE project funded by the Foundation for Strategic Environmental Research. This is contribution no. XX from Tellus, the Centre of Earth Systems Science at the University of Gothenburg.

References

D. Anderson and W. Weeks. A theoretical analysis if sea-ice strength. *Transactions, American Geophysical Union*, 39 (4):632–640, 1958.

C. M. Bitz, M. M. Holland, A. J. Weaver, and M. Eby. Simulating the ice-thickness distribution in a coupled climate model. *Journal of Geophysical Research*, 106(C2):2441-2463, 2001. doi: 10.1029/1999JC000113.

G. Björk. On the response of the equilibrium thickness distribution of sea ice export, mechanical deformation, and thermal forcing with application to the Artic Ocean. *Journal of Geophysical Research*, 97(C7):11287–11298, 1992. doi: 10.1029/92JC00814.

G. Björk. The relation between ice deformation, oceanic heat flux, and the ice thickness distribution in the Artic Ocean. *Journal of Geophysical Research*, 102(C8):18681–18698, 1997. doi: 10.1029/97JC00789.

G. Björk, C. Nohr, B. G. Gustafsson, and A. E. B. Lindberg. Ice dynamics in the Bothnian Bay as inferred from ADCP measurements. *Tellus A*, 60(1):178–188, 2008. doi: 10.1111/j.1600-0870.2007.00282.x.

G. M. Flato and W. D. Hibler, III. Ridging and strength in modelling the thickness distribution of Arctic sea ice. *Journal of Geophysical Research*, 100(C9):18611–18626, 1995. doi: 10.1029/95JC02091.

M. Granskog, H. Kaartokallio, H. Kuosa, D. N. Thomas, and J. Vainio. Sea ice in the Baltic Sea - a Review. *Estuarine Coastal And Shelf Science*, 70(1-2):145–160, 2006. doi: 10.1016/j.ecss.2006.06.001.

B. G. Gustafsson. A time-dependent coupled-basin model of the Baltic Sea. Technical Report C47, Department of Oceanography, 2003.

J. Haapala. *Modelling of the seasonal ice cover of the Baltic Sea*. Ph.d. thesis, University of Helsinki, 2000.

J. Haapala and M. Leppäranta. The Baltic Sea ice season in changing climate. *Boreal Environment Research*, 2(1): 93–108, 1997.

W. D. Hibler, III. A dynamic thermodynamic sea ice model. *Journal of Physical Oceanography*, 9(4):815–846, 1979. doi: 10.1175/1520-0485(1979)009<0815:ADTSIM>2.0.CO;2.

E. C. Hunke and J. K. Dukowicz. An elastic-viscous-plastic model for sea ice dynamic. *Journal of Physical Oceanography*, 27(9):1849–1867, 1997. doi: 10.1175/1520-0485(1997)027<1849:AEVPMF>2.0.CO;2.

M. Leppäranta. An ice drift model for the Baltic Sea. *Tellus*, 33(6):583–596, 1981.

M. Leppäranta. *The drift of sea ice*. Springer in ass. with Praxis Publishing, Chichester, UK, 2005.

M. Leppäranta and K. Wang. The ice cover on small and large lakes: scaling analysis and mathematical modelling. *Hydrobiologia*, 599(1):183–189, 2008. doi: 10.1007/s10750-007-9201-3.

M. Leppäranta, M. Lensu, and Q.-M. Lu. Shear flow of sea ice in the marginal ice zone with collision rheology. *Geophysica*, 25(1-2):57–74, 1989.

M. Leppäranta, Y. Sun, and J. Haapala. Comparison of sea-ice velocity fields from ERS-1 SAR and a dynamical model. *Journal of Glaciology*, 44(147):248–262, 1998.

R. W. Lindsay. Changes in the modeled ice thickness distribution near the surface heat budget of the Arctic Ocean (SHEBA) drifting ice camp. *Journal of Geophysical Research*, 108(C6):3194, 2003. doi: 10.1029/2001JC000805.

W. H. Lipscomb, E. C. Hunke, W. Maslowski, and J. Jakacki. Ridging, strength, and stability in high-resolution sea ice models. *Journal of Geophysical Research*, 112(C03S91), 2007. doi: 10.1029/2005JC003355.

A. Omstedt and L. B. Axell. Modeling the variations of salinity and temperature in the large gulfs of the Baltic Sea. *Continental Shelf Research*, 23(3-4):225–394, 2003. doi: 10.1016/S0278-4343(02)00207-8.

J. E. Overland and C. H. Pease. Modeling ice dynamics of coastal seas. *Journal of Geophysical Research*, 93(C12): 15619–15637, 1988. doi: 10.1029/JC093iC12p15619.

R. S. Pritchard. Long-term sea ice dynamics simulations using an elastic-plastic constitutive law. *Journal of Geophysical Research*, 106(C12):31333–31343, 2001. doi: 10.1029/2000JC000638.

D. A. Rothrock. The energetics of the plastic deformation of pack ice by ridging. *Journal of Geophysical Research*, 80 (33):4514–4519, 1975. doi: 10.1029/JC080i033p04514.

J. L. Schramm, M. M. Holland, J. A. Curry, and E. E. Ebert. Modeling the thermodynamics of a sea ice thickness distribution 1. Sensitivity to ice thickness resolution. *Journal of Geophysical Research*, 102(C10):23079–23092, 1997. doi: 10.1029/97JC01297.

G. Timco and M. Johnston. Ice strength during the melt season. Volume 2 of *Proceedings of the 16th IAHR International Symposium on Ice*, pages 187–193, Dunedin, New Zealand, 2002.

J. Ukita and R. E. Moritz. Yield curves and flow rules of pack ice. *Journal of Geophysical Research*, 100(C3):4545–4557, 1995. doi: 10.1029/94JC02202.

Z. H. Zhang. Comparisons between observed and simulated ice motion in the northern Baltic Sea. *Geophysica*, 36(1-2): 111–126, 2000.